Assessing Site Response Complexity Using Single Station HVSR: Mexico City Case Study

A master's thesis submitted by
Marshall A. Pontrelli

In partial fulfillment of the requirements for the degree of Master of Science
In Civil and Environmental Engineering

Tufts University
August 2019

Adviser: Dr. Laurie Baise

Committee Members: Dr. Dick Plumb, Dr. Juan Pestana and Dr. Jon Lamontagne

Purpose: Use the horizontal to vertical spectral ratio (HVSR) to characterize site response in high impedance basin environments. Test the applicability of the Thompson et al. (2012) statistics to the HVSR. Demonstrate that the shape of the HVSR can be used to characterize site response and potentially identify site response complexity, the shape being characterized by: the total number of peaks, and the frequency, amplitude, half power bandwidth and interevent variability of the fundamental peak.

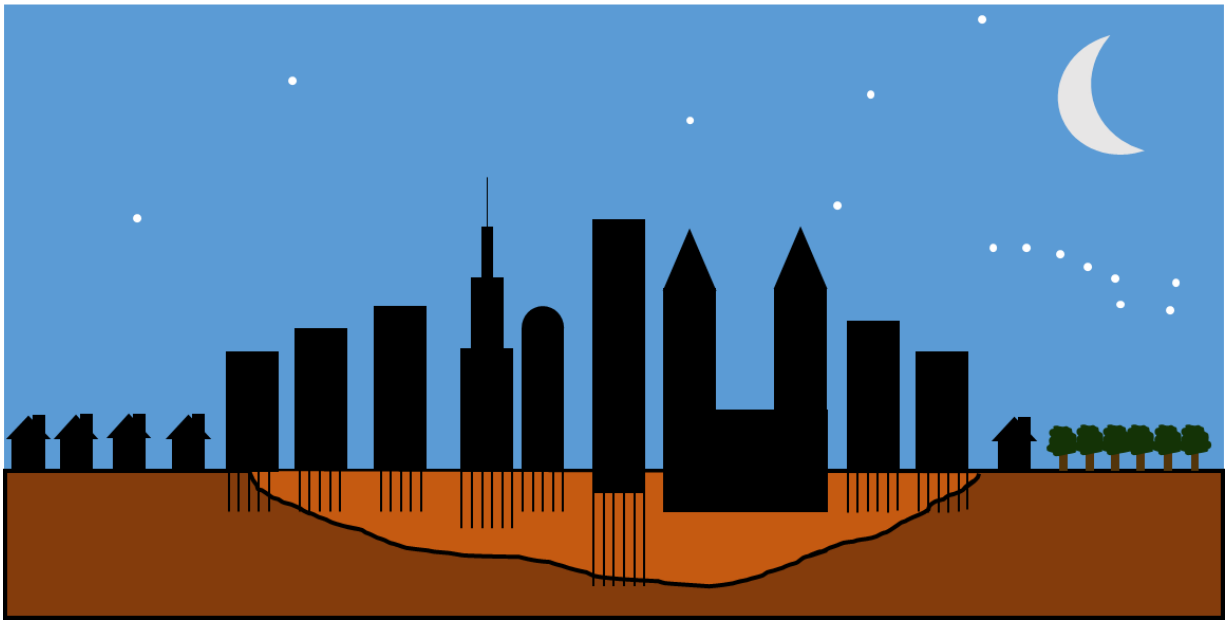

“As an earthquake wave travels from strata to strata, if we study its reflection and changing velocity in transit, we may often be led to the discovery of certain rocky structures buried deep beneath our view, about which without the help of such waves it would be hopeless ever to attain any knowledge… Earthquakes are gigantic experiments which tell the elastic moduli of rocks as they exist in nature, and when properly interpreted may lead to the proper comprehension of many ill-understood phenomena.”

-John Milne
1898

ABSTRACT

Sedimentary basins with high impedance contrasts can lead to significant shaking due to local site response during earthquakes and, as a result, pose a significant risk to infrastructure and local populations. The site response transfer function is most often modeled as the response of a soil column to a forcing function assuming vertically propagating shear waves through horizontal, laterally homogenous soil systems. In real soil systems, however, these assumptions tend to collapse due to wave scattering through heterogenous materials, significant attenuation, non-vertical incidence, and other complexities in the subsurface. In work by Thompson et al. (2012), the authors develop a taxonomy using surface-downhole spectral ratios from weak ground motions for classifying a site's resonant behavior referenced to the SH1D condition. We attempt to apply this taxonomy to single station recordings in Mexico City, a case study where basin effects are well documented, by using the horizontal to vertical spectral ratio (HVSR) (Nakamura, 1989) as a first estimate of the site empirical transfer function (Lermo and Chávez-Garcia, 1994b), and using a theoretical transfer function derived from inversion. The HVSR clearly identifies a fundamental resonance peak and even higher resonance modes at some stations in the basin; however, the shape of the HVSR changes from the transition zone (at the edge of the basin) into the lake bed sediments (within the basin). The inverted theoretical transfer function also exhibits limitations mapping onto the HVSR. We extend the taxonomy by proposing a set of statistics describing the shape of the HVSR to assess site response complexity: the number of significant peaks, and the frequency, amplitude, half power bandwidth and interevent variability of the fundamental peak. We observe that these statistics vary spatially across the extent of the Mexico City basin in quantifiable patterns, reflecting variations in subsurface properties and providing indications of complex site response.

TABLE OF CONTENTS

LIST OF FIGURES

LIST OF TABLES

*Indicates a table that is in the appendix because of its size, these tables are still numbered sequentially as they show up in the text

LIST OF EQUATIONS

1.0 INTRODUCTION

1.1 Background

1.1.1 Site response definition

Local geology amplifies seismic energy due to the shape and properties of the geologic structure, a phenomenon known as “site response”. The common structure that causes this effect is a sedimentary basin with soft, low density, low velocity overburden overlying hard, high density, high shear wave velocity basement (Thomson, 1950; Haskell, 1960; Borcherdt, 1970; Kramer, 1996; Baise et al. 2016, Yilar et al. 2017). The impedance contrast between the overburden and basement (Eq. 1) affects the amplitude of shaking, a, and the depth, d, and shear wave velocity, β, of the overburden affects the fundamental frequency of shaking, f_n (Eq. 2). Some examples of cities built on this structure are San Francisco, Mexico City, Seattle and Boston among many others. Site response poses an issue for infrastructure and, by association, citizens of cities built on these basins due to the tendency of buildings to resonate with the ground. This can have devastating effects as was seen in the 1985 Michoacán earthquake in Mexico City and the 1989 Loma Prieta earthquake in San Francisco. Quantifying basin resonance is essential to develop resilient infrastructure in earthquake-prone areas.

Normal incidence shear waves propagating vertically through the subsurface amplify at

$$\left| {}^{v_i}/_{2v_j} \right| = {}^{\rho_i \beta_i}/_{\rho_j \beta_j} \tag{1}$$

at frequencies

$$f_n = {}^{\beta_i}/_{4d_i} \tag{2}$$

where

υ_i = displacement amplitude of a layer
υ_j = displacement amplitude of a different layer
ρ_i = density of the nth layer
β_i = shear wave velocity of the nth layer
d_i = depth of the layer
f_n = fundamental frequency

(Haskell, 1960; Kramer, 1996). An impedance contrast (Eq. 1) greater than 1 between overburden and basement, yields free surface amplification and an impedance contrast below 1 yields free surface de-amplification. An increase in depth to the basement or a decrease in the shear wave velocity, yields a decrease in fundamental frequency (Eq. 2; Fig. 2*a*). These relationships are vital to estimate site amplification and fundamental frequency and consequently are essential to site response analyses. We can leverage these relationships using near-surface geophysical techniques to model and incorporate the near surface into seismic hazard analyses.

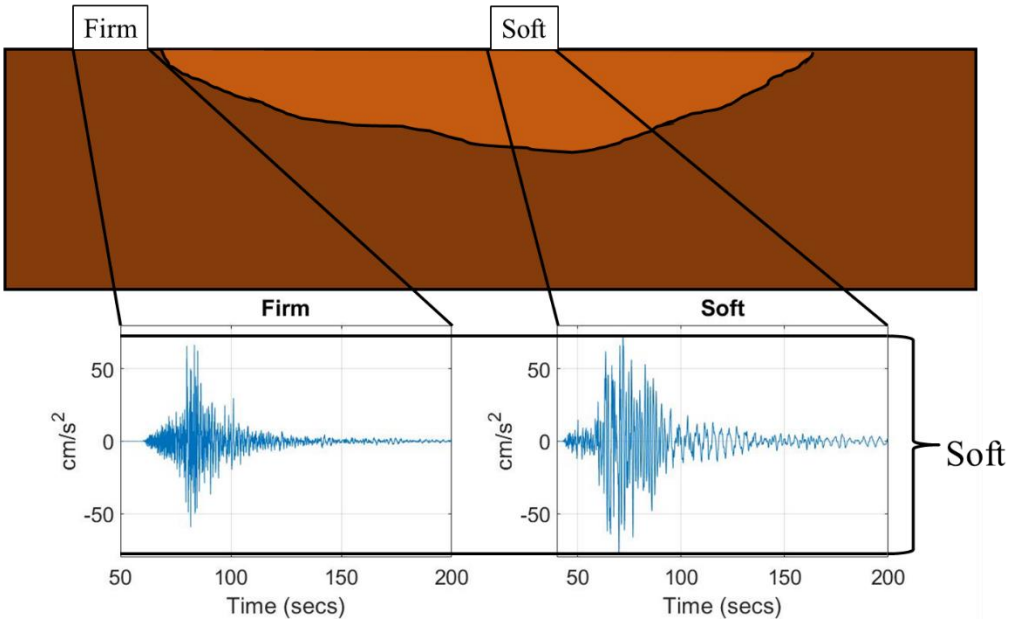

Figure 1. Cartoon of a sedimentary basin with recordings from the 2017 Puebla earthquake in Mexico City or a firm site and soft site. The amplitude of the waves on the soft site is greater than the hard site, as is the size of the energy envelope, and the period at the soft site is longer than the period of the hard site.

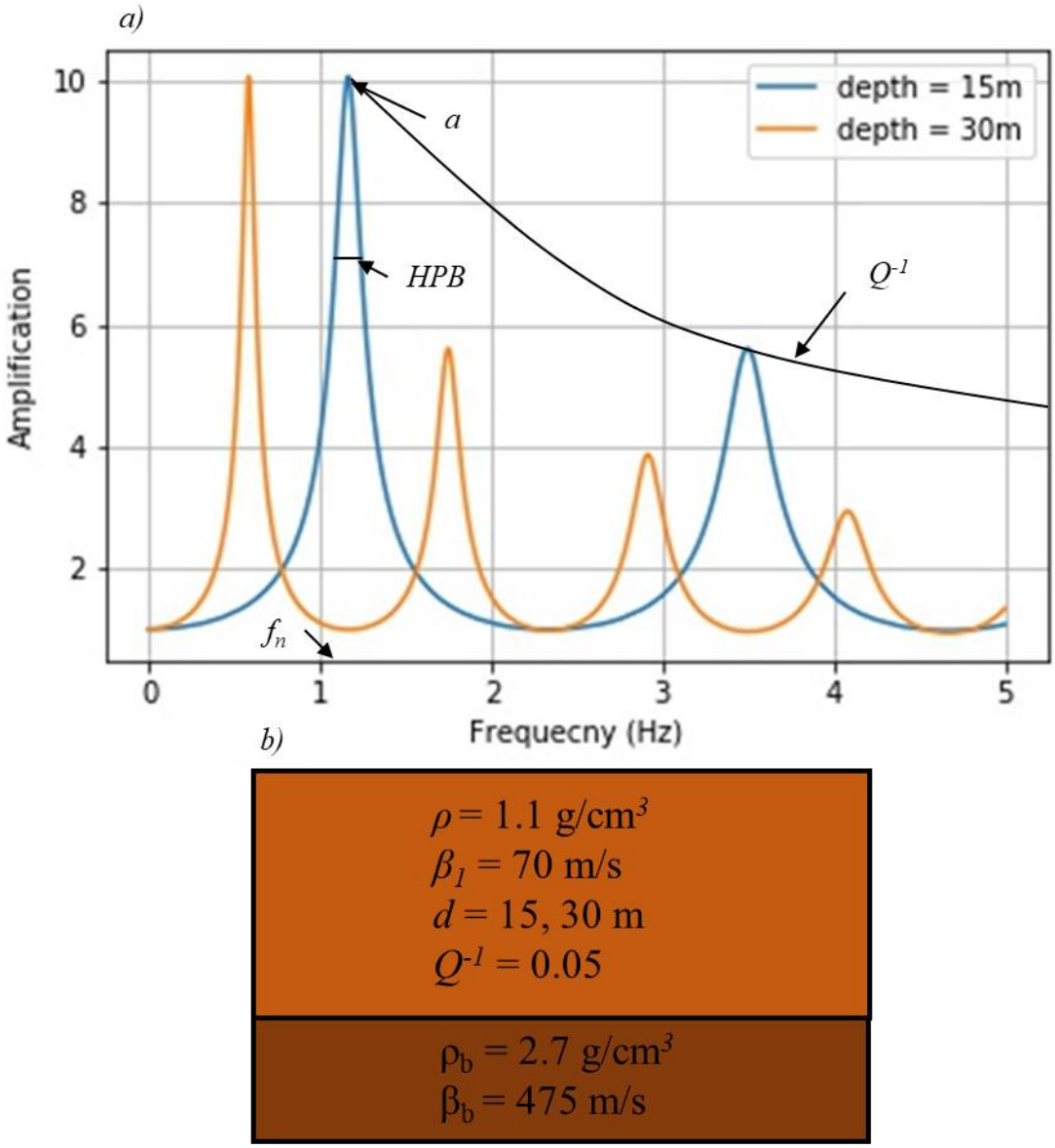

Figure 2. *a)* Example TTFs at 2 depth values (15 m and 30 m), showing f_n, *HPB*, and Q^{-1}. *b)* Input model values for the typical Mexico City Basin site (Stephenson and Lomnitz, 2004).

1.1.2 Theoretical transfer function

We model the theoretical transfer function, hereafter TTF, with 1) vertically propagating shear waves through 2) laterally homogenous soil layers that have 3) frequency independent damping and 4) strain independent shear modulus, assumptions collectively referred to as “SH1D”.

The source input *i(t)*, earth's crust $h_e(t)$, site geology $h_g(t)$, and instrument response $h_r(t)$ are linear time invariant systems, and the recorded ground motion *s(t)* is a linear combination of these systems (Fig. 3):

$$s(t) = i(t) * h_e(t) * h_g(t) * h_r(t) \tag{3}$$

Where "*" is the convolution operator (Appendix Eq. 1.1; Borchert, 1970; Sheriff and Geldart, 1995). The Fourier response spectra of the ground motion is equal to the product of the Fourier transform (Appendix Eq. 1.2) of each of the respective systems:

$$S(f) = I(f)\, H_e(f)\, H_g(f)\, H_r(f) \tag{4}$$

An earthquake at a large hypocentral distance from the location of interest has vertically incident incoming waves due to Snell's law (Appendix Eq. 3.3) and the tendency of density to increase with depth in the Earth (Sheriff and Geldart, 1995). Two records in the basin, *a* and *b*, have equal source, path and instrument response, thus the shear wave transfer function, *a(f)*, from location *b* to location *a* is the ratio of the magnitude response spectra of the horizontal component of *a* and *b*.

$$a(f) = \frac{S_{ha}(f)}{S_{hb}(f)} \tag{5}$$

where $S_{ha}(f)$ is the horizontal component of the record at location *a* and $S_{hb}(f)$ is the horizontal component of the record at location b. This ratio is the TTF (Kramer 1996; Appendix 1, Eq. 1.3).

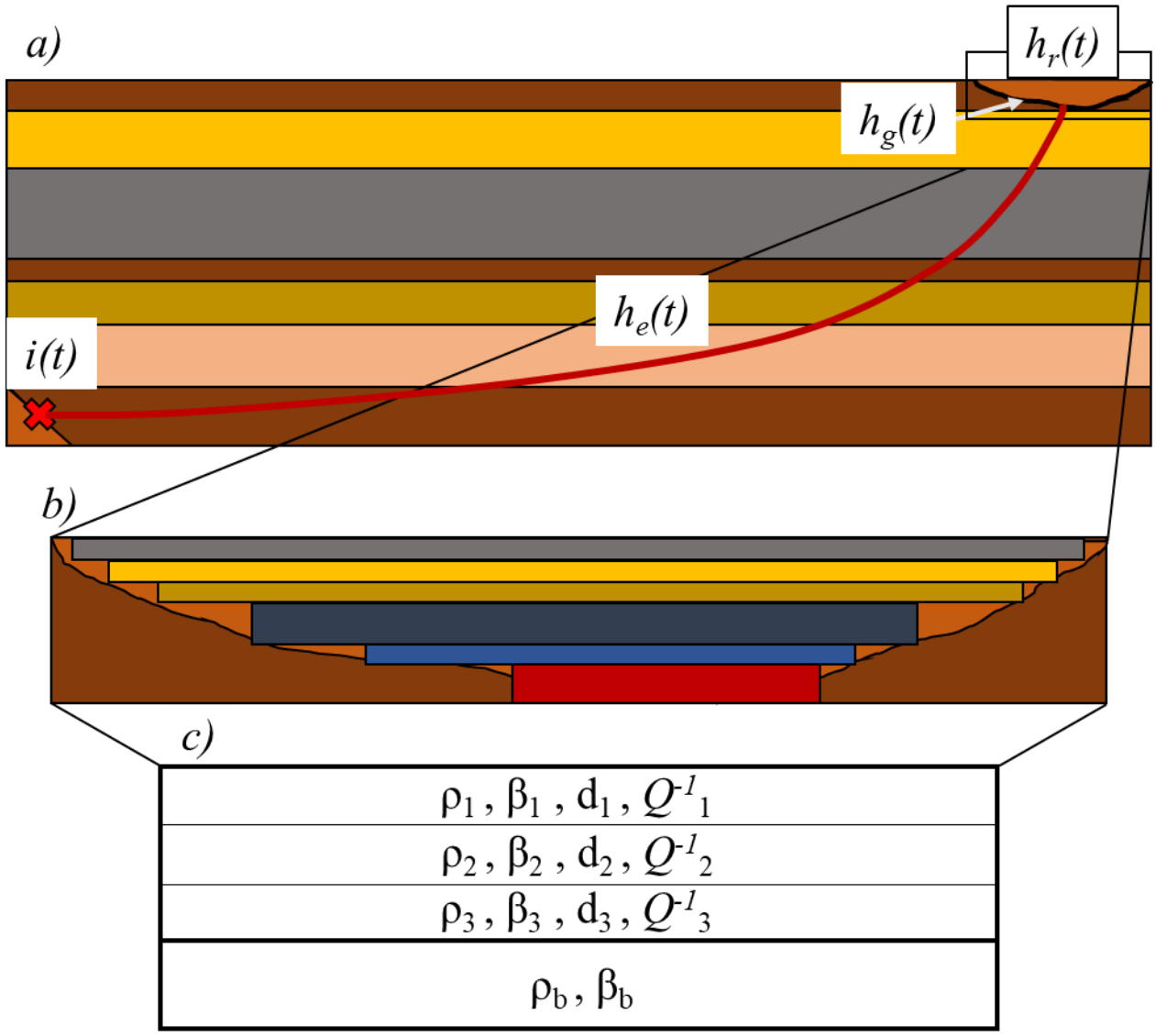

Figure 3. *a)* Site response model from a global seismological perspective with earthquake hypocenter, $i(t)$, represented by a red x, earth's crust, $h_e(t)$, represented by horizontal layers of varying color, site geology, $h_g(t)$, represented by a brown basin, and instrument response, $h_r(t)$, represented by a black square. *b)* The site geology, $h_g(t)$. *c)* The variables with which we model the site geology.

Seismic waves propagating through a medium are subject to dissipation of energy known as attenuation. We denote generalized seismic attenuation $Q^{-1}{}_{p,s}$. It consists of both *P* and *S* wave attenuation each of which is divided into two processes: attenuation by wave scattering ($^{Sc}Q^{-1}$), and intrinsic attenuation ($^{i}Q^{-1}$). Attenuation by wave scattering occurs when heterogeneities in the

properties of the material through which the energy travels scatters the waves. This does not remove energy from the seismic wavefield, and we refer to it as "geologic complexity". Intrinsic attenuation is the dissipation of energy from friction of particles, viscosity, permanent deformations and thermal relaxation (Sato and Fehler, 1998). We analyze *S* wave attenuation in this study, hereafter Q_s^{-1}. Attenuation of a system is related to the damping ratio, ζ, of the system (Appendix 2, Eq. 2.7) in percent:

$$\zeta = 100 * 0.5 * {Q_{p,s}}^{-1} \tag{6}$$

The TTF of shear waves is a function of the vibrational properties of the media through which the waves propagate: d, β, ρ, and Q_s^{-1} of the overburden, and Q_s^{-1} and ρ of the basement (Fig. 2*c*). We use spectral properties of real records to estimate these relationships.

1.1.3 Empirical transfer function

We forward model TTFs by inputting vibrational material properties of SH1D layers d, β, ρ, and Q_s^{-1} and generating the response of one layer to another by dividing their synthetic frequency contents (Fig. 2). Our approach is using *s(t)* of real records to make inferences about the vibrational material properties. For this, we use the empirical transfer function, hereafter ETF, a spectral ratio of the magnitude response of one signal to another. In practice, we use two spectral ratios to compute the site ETF: the borehole transfer function, and the simple spectral ratio, hereafter SSR, and one spectral ratio to approximate it: the horizontal to vertical spectral ratio, hereafter HVSR.

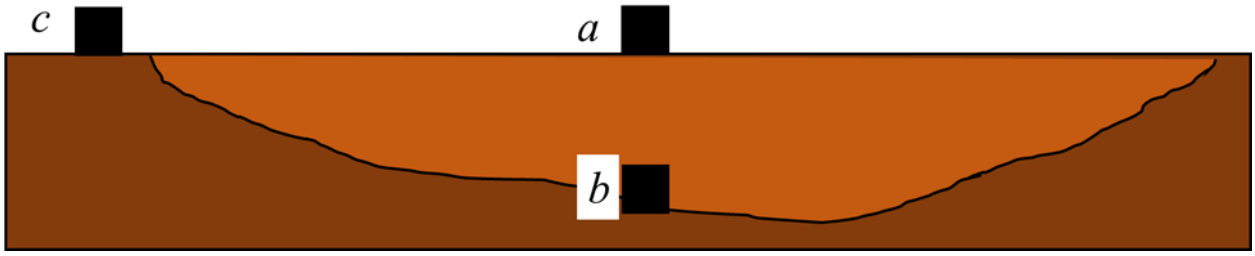

Figure 4. Sedimentary basin with three locations: *a*, at the site of interest, *b*, at the base of the overburden and *c*, at a reference site.

1.1.3.1 Surface-borehole ETF

The surface-borehole spectral ratio is the most direct way to calculate the ETF. It requires a recording at the base of the soil column, location *b*, and a recording at the top of the soil column, location *a* (Fig. 4). We compute the magnitude response of the recordings and take their spectral ratio (Eq. 5), thus generating the transfer function between location *b* and location *a*. This method has been used in numerous site response studies (Baise et al. 2003a.; Baise et al. 2003b.; Thompson et al. 2012; Kaklamanos, 2015; Kaklamanos, 2018a). It is, however, expensive to perform in the field due to the cost of borehole installation.

1.1.3.2 Simple spectral ratio ETF

The SSR is a less direct way to calculate the ETF. It uses a recording at a surface reference site, location *c*, and a recording at the free surface site of interest, location *a* (Fig. 4). Like the surface-borehole ETF, we compute the magnitude response of each recording and take their spectral ratio (Eq. 5). The SSR method assumes that the source and path effects are equivalent from a significantly distance hypocenter and that the basement rock motion at location *c* is equal to the basement rock motion at location *b*. Site response analysts take care to assure that the reference site is a valid approximation of ground motion at location *b* (Steidl et al. 1996). It has been used effectively in many studies (Borcherdt, 1970; Campillo et al. 1989, Shearer and Orcutt,

1987; Lermo and Chávez-Garcia 1994a; Pratt and Brocher, 2006, Pratt, 2018a;) and can be performed at a lower cost than the surface-borehole ETF.

1.1.3.3 HVSR

The horizontal to vertical spectral ratio (HVSR) is an indirect way of approximating the surface-to-borehole ETF from a single surface recording at location *a* (Fig. 4) by canceling out the Rayleigh wave and *P*-wave influences on the surface record in order to enhance the image of the shear wave resonance (Nakamura, 1989). The surface ground motion is contaminated by surface waves, particularly Rayleigh waves, so the magnitude response at a site is not a clear representation of shear wave content in the record. The HVSR minimizes the effect of the Rayleigh wave on the surface recording to isolate the shear wave resonance, thus approximating both the fundamental frequency and amplification of multiple reflecting SH waves. The amplification of vertically propagating shear waves is

$$a(f) = H_a/H_b \tag{7}$$

where H_a is the horizontal magnitude response at location *a* on the ground surface, and H_b is the horizontal magnitude response at location *b* at depth (Fig. 4). This ratio is analogous to the surface-borehole transfer function (Eq. 5). The surface site, H_a, is influenced by Rayleigh waves, the amount of which relative to the bedrock site is

$$Influence\ of\ Rayleigh\ wave = V_a/V_b \tag{8}$$

where V_a is the vertical magnitude response at location *a*, and V_b is the vertical magnitude response at location *b*. This assumes that the Rayleigh wave particle ellipse dimensions are uniform and scaled throughout the material (Fig. 5, maroon lines). Dividing the shear wave amplification by the influence of the Rayleigh wave, therefore, removes the influence of the Rayleigh wave.

$$a(f)/\ Influence\ of\ Rayleigh\ wave = \frac{H_a}{H_b} \times \frac{V_b}{V_a} \quad (9)$$

There is little amplification of multiple reflecting *P*-waves propagating from location *b* to location *a* at the shear wave resonant frequency (f_n) because the *P*-wave has a higher velocity than the *S*-wave, thus the *P*-wave f_n will be higher than the *S*-wave f_n (Appendix Eq. 3.1; 3.2). Similarly, Rayleigh waves influence the record at higher frequencies than the *S*-wave f_n. The ratio of the vertical motions at the *S*-wave f_n is therefore approximately 1, while at higher frequencies, the correction normalizes out the Rayleigh wave and *P*-wave influences. The Rayleigh and *P*-wave resonance peaks beyond the *S*-wave f_n are therefore diminished without significantly affecting the amplitude or shape of the fundamental peak. The *S*-wave f_n and amplification at location *a* can therefore be approximated by the HVSR at the fundamental frequency (f_0) as

$$HVSR(f_0) = \frac{H_a}{V_a} \quad (10)$$

because $V_b/H_b = 1$. Equation 10 defines the horizontal to vertical spectral ratio. (Appendix 6).

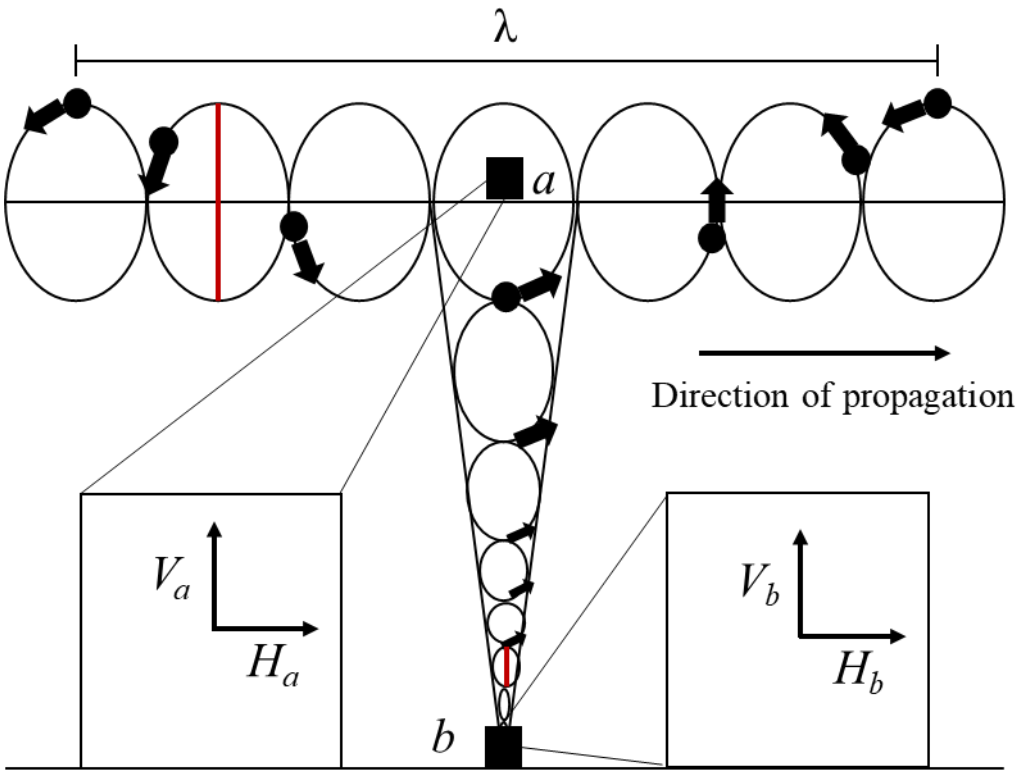

Figure 5. Retrograde Rayleigh waves traveling left to right across the page. The circles represent particles and the arrows represent their motion. The ellipses show the continuous particle motion. The squares represent locations *a* at the surface and *b* at depth. The maroon lines show the length of the long axis of the Rayleigh wave ellipse at location *a* and at location *b*. The Rayleigh wave cartoon is based on Fig. 2.15 in Sheriff and Geldart 1995, second edition.

1.2 Motivation

In Thompson et al. (2009), the authors compared two computations of the SH1D theoretical transfer function to the site empirical borehole transfer function and concluded that there is a significant difference between the ETF and two TTF computations that is substantially larger than the difference between two TTFs. They attributed this discrepancy to either (1) a mismeasurement of soil properties, aleatoric uncertainty, and/or (2) a breakdown in the SH1D model, epistemic uncertainty, and concluded that the latter is most likely the primary cause for the discrepancy.

They compared the ETF to the TTF using 13 KiK-net stations in Japan, each with coupled surface and borehole seismometers with depths ranging from 100 to 200 meters. Each site has two shear-wave velocity profiles: one measured both directly from downhole testing, and the other computed indirectly from spectral analysis of surface waves (SASW) testing. They computed each site's surface-borehole ETF by taking the spectral ratio between the 2D complex Fast Fourier Transform (FFT) (Steidl, 1996) of the horizontal recordings at the base and the 2D complex time FFT of the recordings at the surface of 10 small-strain earthquakes with maximum acceleration less than 0.2g (In this study, we use 0.1g per Beresnev and Wen, 1996). They computed the median of the spectral ratios, the standard deviation in natural logarithmic space, and the large-sample confidence interval at each frequency of the surface-borehole ETFs.

They computed the site TTF considering two formulations of the SH1D theoretical transfer function: (1) accounting for the downgoing-wave effect, and (2) accounting only for the upgoing waves (TTF_u). They solved both formulations using the Nrattle Fortran routine (section 3.2). After comparing the TTFs to the ETFs at each of the 13 Kik-net sites as shown in Figure 6, they found that often the site ETF significantly differs from the site TTF, and that in many cases, this discrepancy is due to a breakdown in the assumptions used for the theoretical formulation of the SH1D transfer function.

With an understanding of the discrepancies between the theoretical and empirical transfer functions observed by Thompson et al. (2009), a follow-up study—Thompson et al. (2012)—resulted in the development of a taxonomy to identify sites that conform to the SH1D assumptions and those that do not and are therefore complex. They proposed two statistics to determine site complexity in Thompson et al. (2012): (1) the interevent variability of the ETFs, and (2) the

goodness of fit between the ETFs and the SH1D theoretical transfer function. With this taxonomy, they could identify sites that can be used to calibrate and validate 1-D constitutive models.

The interevent variability describes the variation in ETFs from event to event. It is defined as the median standard deviation in natural logarithmic space between the first and fourth peaks of the theoretical transfer function and denoted σ_i. A "high" interevent variability is a σ_i value greater than 0.35 and is denoted with an "H", and a "low" interevent variability is a σ_i value less than 0.35 and is denoted with an "L". High interevent variabilities could be indicators of (1) geologic complexity and/or (2) events in the ETF computation with geographically nearby hypocenters. A geologically complex site will cause different reflection and refraction effects depending on the azimuth of wave propagation. Using events with nearby hypocenters in the ETF computation contaminates the receivers with source and path effects, thus increasing scatter in the ETFs and increasing the interevent variability. Stations with high interevent variabilities must be three-dimensionally modeled, considering surface wave contaminations or source and path influence on the empirical transfer function.

The goodness of fit to the SH1D transfer function describes how well the ETF matches the TTF from peak to peak. It is defined as the median correlation coefficient (r) between the ETF and the TTF between the first and fourth peaks of the TTF. A station with "good" fit to the SH1D transfer function has an r value greater than 0.60 and is denoted with a "G", and a station with "poor" fit to the SH1D transfer function has an r value less than 0.60 and is denoted with a "P". ETFs with poor fits to the SH1D transfer function could be attributed to (1) mismeasurement of soil properties at the site and/or (2) a breakdown in the SH1D assumptions.

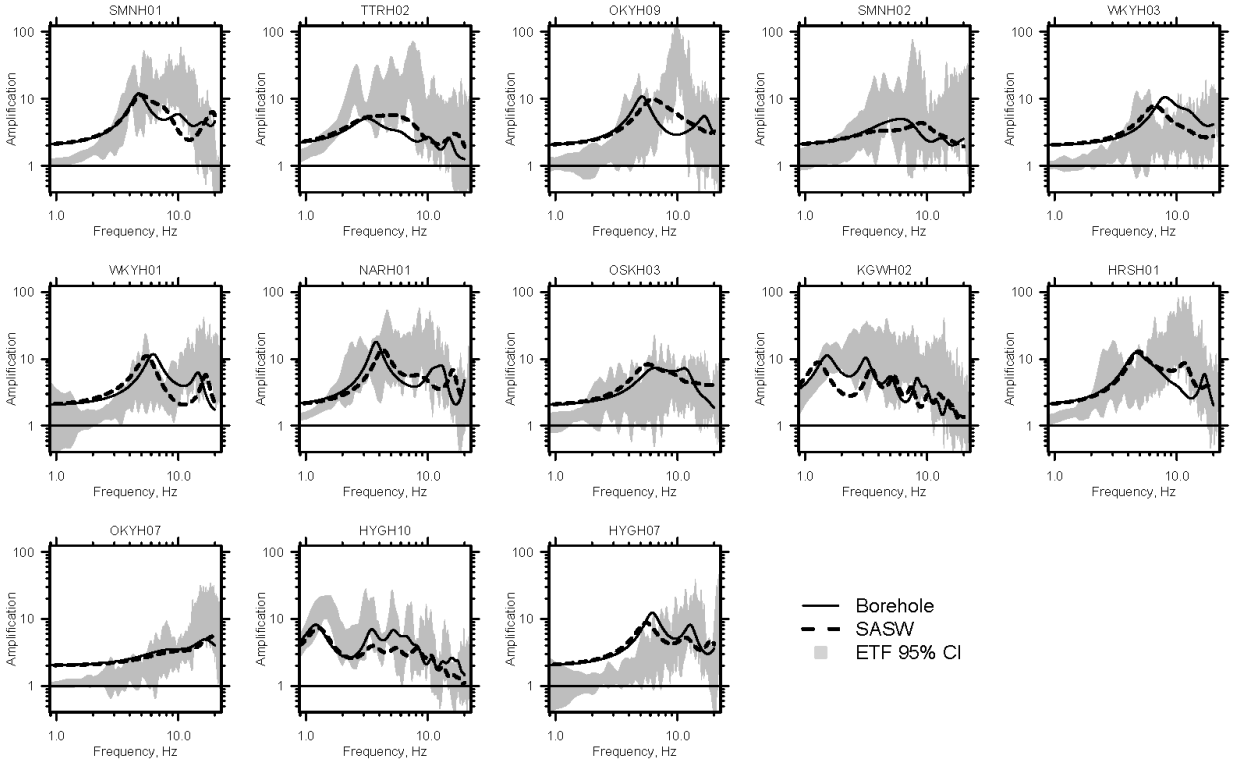

Figure 6. The ETF 95% confidence interval versus TTFu, computed by Nrattle using the SASW and downhole profiles with ${}^{i}Qs$ = 12.5. Figure from Thompson et al. (2009).

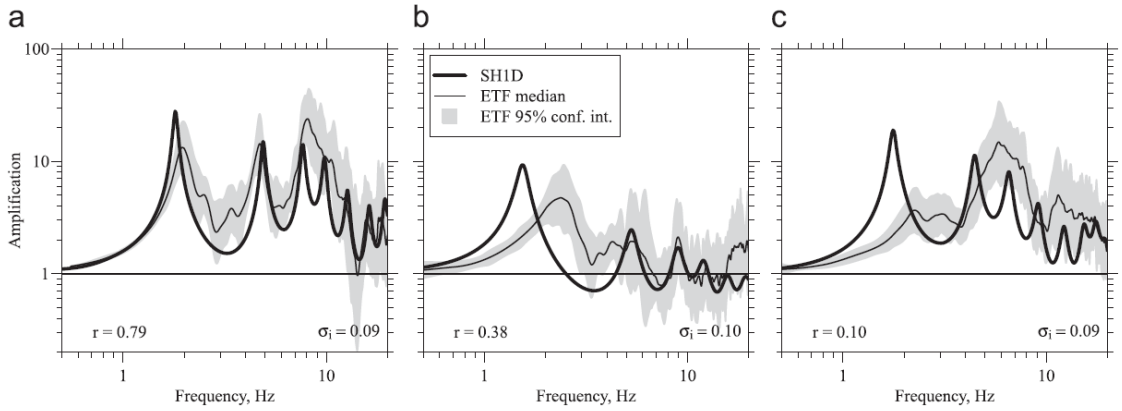

Figure 7. The ETF and SH1D TTF amplifications at sites (a) TKCH08, (b) ISKH02, and (c) TKCH05. The correlation coefficient r and the inter-event standard deviation σ_i are reported for each site. The sites have average shear-wave velocities over the top 30 m (V_{S30}) values of (a) 353 m/sec, (b) 721 m/sec, and (c) 337 m/sec, respectively. Figure from Thompson et al. (2012).

The taxonomy thus has four classifications based on sites' interevent variability and goodness of fit to the SH1D transfer function: LG, LP, HP and HG. LG sites have low σ_i and good

ETF-TTF fit and are therefore good sites to calibrate and validate one-dimensional constitutive models. LP sites have low σ_i and poor ETF-TTF fit and can be used to test non-linear soil models if the sources of their discrepancies (e.g., the mismeasurement of soil properties or a breakdown of the SH1D assumptions) are properly identified (Fig. 7 b and c). HP sites have high σ_i and poor ETF-TTF fit, and therefore have path and source effects associated with their records and can thus only be modeled if these effects are accounted for. HG sites have a high σ_i and good ETF-TTF fit, and are thus difficult to interpret, as we expect high σ_i to be indicative of complexities associated with a breakdown of SH1D assumptions.

1.3 Hypothesis

We perform the HVSR at stations across the Mexico City basin using 218 earthquakes recorded at multiple stations in the Mexico RACM network (http://www.cires.org.mx/). We test the applicability of the Thompson et al. (2012) statistics to the HVSR and then test our observation that the shape of the HVSR changes in spatial patterns across the basin. The Mexico City basin is filled with low density and shear-wave velocity clays overlying a higher density and shear-wave velocity basement. The City has three geotechnical zones: the "hill zone" classified by bedrock, the "transition zone" classified by clays with lenses of silt and sand less than 20 m thick, and the "lake zone" classified by resonant clays greater than 20 m thick (Moisés et al. 2016). We compute the average HVSR from all the small strain events at each of the 70 stations in the network and average the signals together with the horizontal and vertical components of a single station instead of the horizontal components of surface-borehole pairs (Fig. 8, section 3.1.2). Expecting only one distinct peak from the HVSR, at a few sites in the lake zone, we observe distinct resonance peaks in the HVSR that we interpret as shear wave higher mode resonance peaks. These resonance peaks match up with a theoretical transfer function computed using Nrattle (Boore, 2005) of a one-layer

model of Mexico City for the first four peaks and troughs and can be captured by the Thompson et. al (2012) classifications. Many of the stations, however, only exhibit a single peak as expected from the HVSR (Eqs. 8; 9).

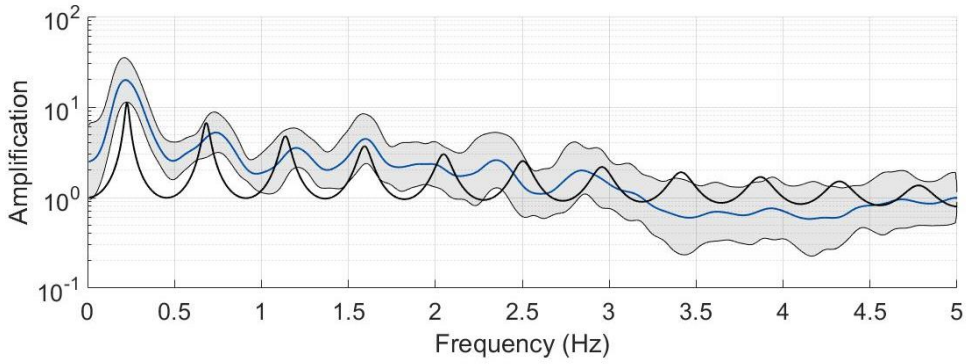

Figure 8. HVSRs of all recorded small-strain events and their median at lake zone site CE32 in Mexico City. The blue line is the maximum likelihood estimator of the median of the HVSRs, and the grey bands are the large-sample confidence interval. The black line is a theoretical transfer function of a one-layer model with β = 70 m/s, ρ = 1.1 g/cm^3, d = 76.89 m, and ^iQs = 0.038.

We also observe a distinct increase in width of the fundamental peak of the HVSR with decreasing depth to the Mexico City halfspace. The Mexico City lake zone stations have thinner fundamental peaks than the transition zone stations (Fig. 9). We hypothesize that it may be possible to identify SH1D sites or complex sites by developing statistics to describe the HVSR shape. Certain shapes should be indicative of complex sites, and certain shapes should be indicative of SH1D sites, where 1D wave propagation assumptions are most valid.

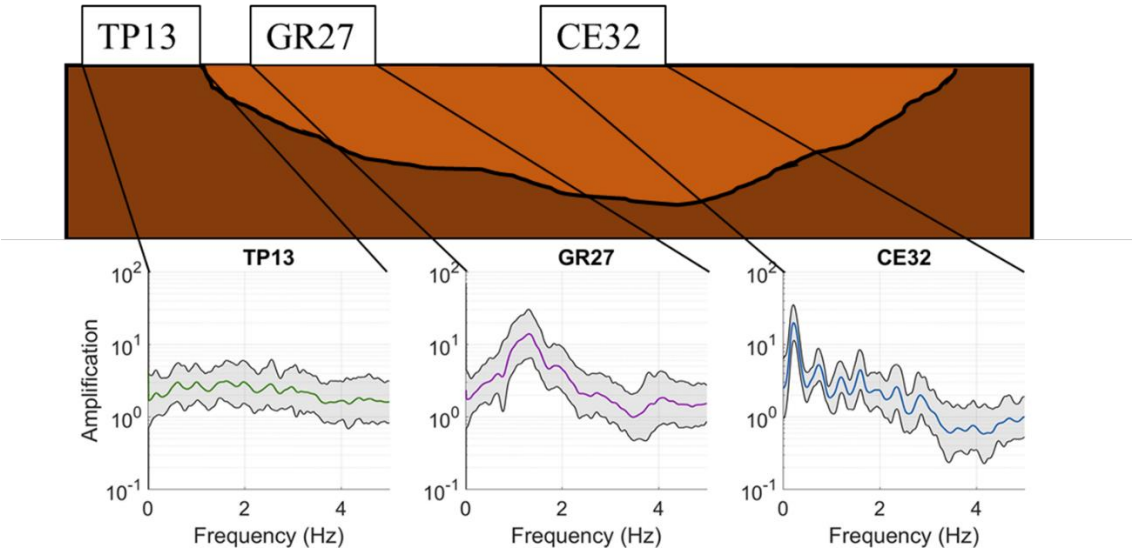

Figure 9. Three selected Mexico City stations and their corresponding HVSRs. These stations run across a transect in Mexico City of increasing depth. TP13 is in the hill zone, GR27 the transition zone and CE32 the lake zone.

We propose 5 statistics to describe the shape of the HVSR: 1) the number of peaks in the HVSR 2) the frequency (f_n) 3) the amplitude (a) 4) the half power bandwidth (HPB) (a value for the width) and 5) the interevent variability (σ_i) of the fundamental peak. The number of peaks allows us to identify sites that have HVSRs that display higher modes and the fundamental peak shape statistics allow us to quantify how the HVSR changes with varying geologic conditions and properties. Using these statistics, we can systematically categorize the shape and properties of the HVSR and correlate them to local geologic complexity.

2.0 DATA

2.1 Mexico City RACM network

2.1.1 Background

Following the 1985 Michoacán earthquake, the government of Mexico City installed the RACM network (http://www.cires.org.mx/) in partnership with the National Autonomous University of Mexico (UNAM) to provide ground motion data for basic research to assess and mitigate vulnerability within the Mexico City basin. Since 1987, 80 devices have recorded 259 events at 72 surface and 8 borehole stations (CIRES website). Of these, we use 218 events recorded at 70 stations: 52 lake zone stations, 8 transition zone stations, 4 compact stations, and 6 hill zone stations and compute Thompson et al. (2012) statistics and fundamental peak shape statistics at 60 of them, the lake and transition zone stations (Fig. 10, Tab. 1).

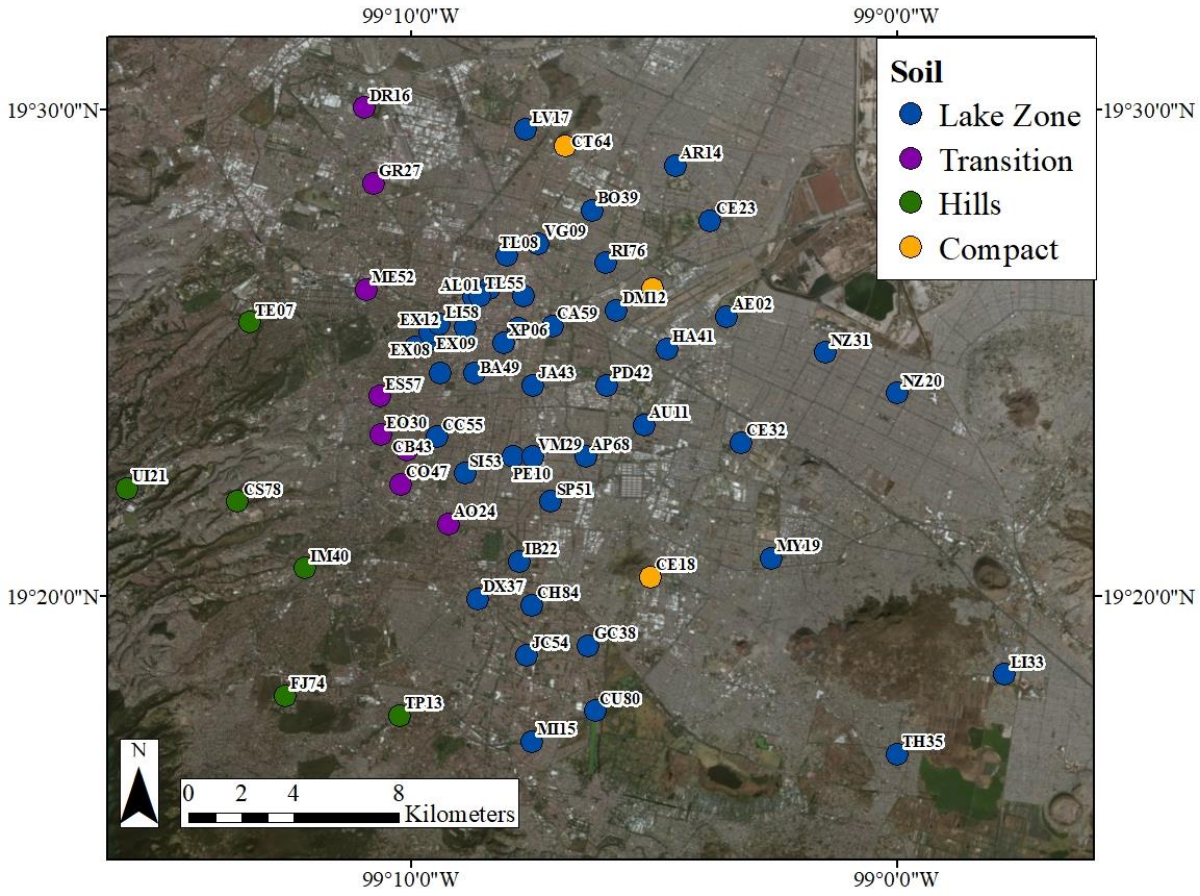

Figure 10. Mexico City RACM network stations with corresponding geotechnical zone.

2.1.2 Earthquake details and tectonic setting

Mexico City is in one of the most seismically active regions in the world at the confluence of four tectonic plates: the Cocos, North American, Rivera and the Caribbean. Most of the events recorded by the RACM network have epicenters on the subduction zone between the Cocos and North American plate (Fig. 11, Tab 2). The events in the database have a minimum magnitude of 2.5 and a maximum magnitude of 8.2. Most of the events come from a southern azimuth.

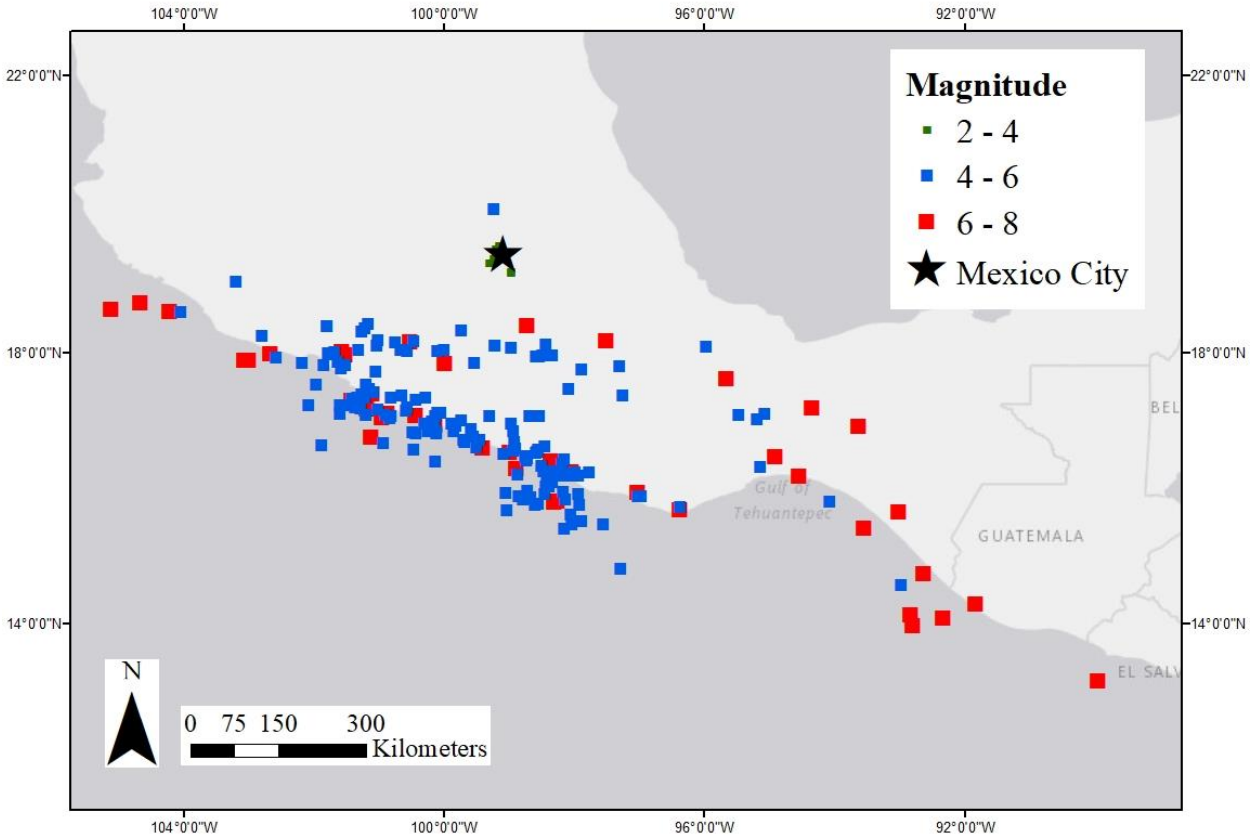

Figure 11. Earthquakes used in this study with Mexico plotted as a black star.

2.2 Geologic and geotechnical properties

2.2.1 Geology

Mexico City is built at the location of three historic shallow lakes: Texcoco, where most of the urban sprawl is now located, Xochimilco, to the southwest of Texcoco and Chalco, to the southeast of Texcoco (Fig. 15). They were filled with windblown volcanic ash during the Wisconsin glacial period and are now characterized by compressible, high plasticity, high water content clays interspersed with horizontal lenses of sand and soil layers (Romo, 1988). The lakes were shallow and therefore never formed any significant deltas while the ash was settling, leaving the lake sediments mostly laterally homogenous (Stephenson and Lomnitz, 2005). The general

stratigraphy of the lakes is a 1-2 meter crust underlain by 25-30 meters Upper Clay Formation (UCF) underlain by the roughly 3 meter thick First Hard Layer (FHL) underlain by around 20 meters of Lower Clay Formation (LCF) until the Deep Deposits (DD) (Fig. 12) (Romo, 1988; Stephenson and Lomnitz, 2005).

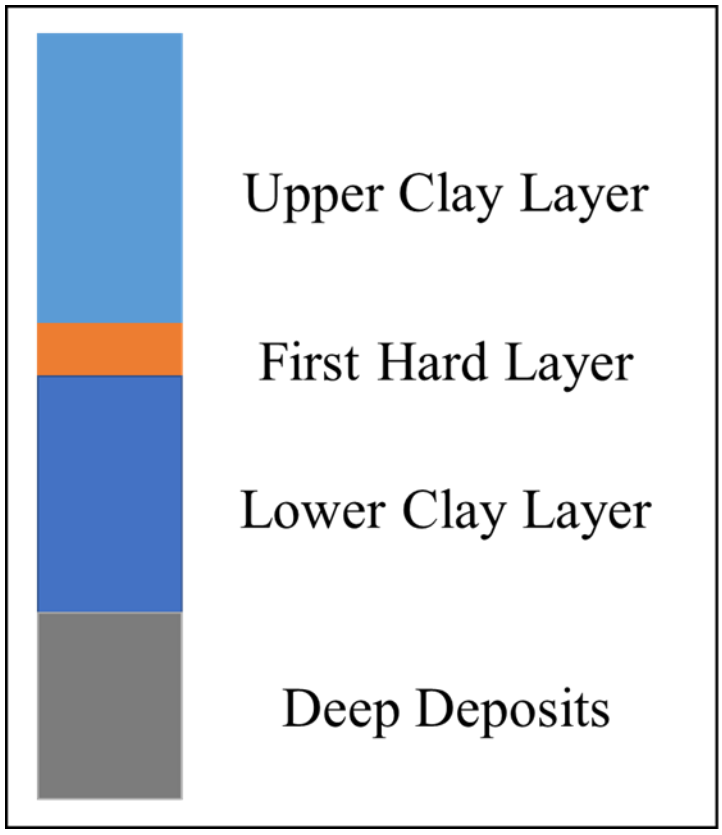

Layer	β (m/s)
UCL	70
FHL	200
LCL	100
DD	475

Figure 12. Generalized geologic and shear wave velocity profile of Mexico City.

For engineering purposes, we assume the first three layers overly a high velocity basement (DD as half-space) (Romo 1988). Stephenson and Lomnitz, (2004) and Mayoral et al. (2016) performed SCPT and SASW tests respectively to compute shear wave velocity profiles for Mexico City (Figs. 12; 13). We use the estimates of ρ_1, β_1, ρ_2, β_2 in the literature for the model parameters (Stephenson 2005; Campillo 1989; Mayoral, 2016). These values vary spatially in Mexico City but are well enough constrained that for this study we approximate the Mexico City stratigraphy

as a single layer halfspace with density and shear wave velocity of the overburden 1.1 g/cm^3 and 70 m/s respectively and density and shear wave velocity of the bedrock 2.7 g/cm^3 and 475 m/s respectively, values provided in Stephenson 2005 and the shear wave velocity profile in Mayoral et al. (2016) (Fig. 13).

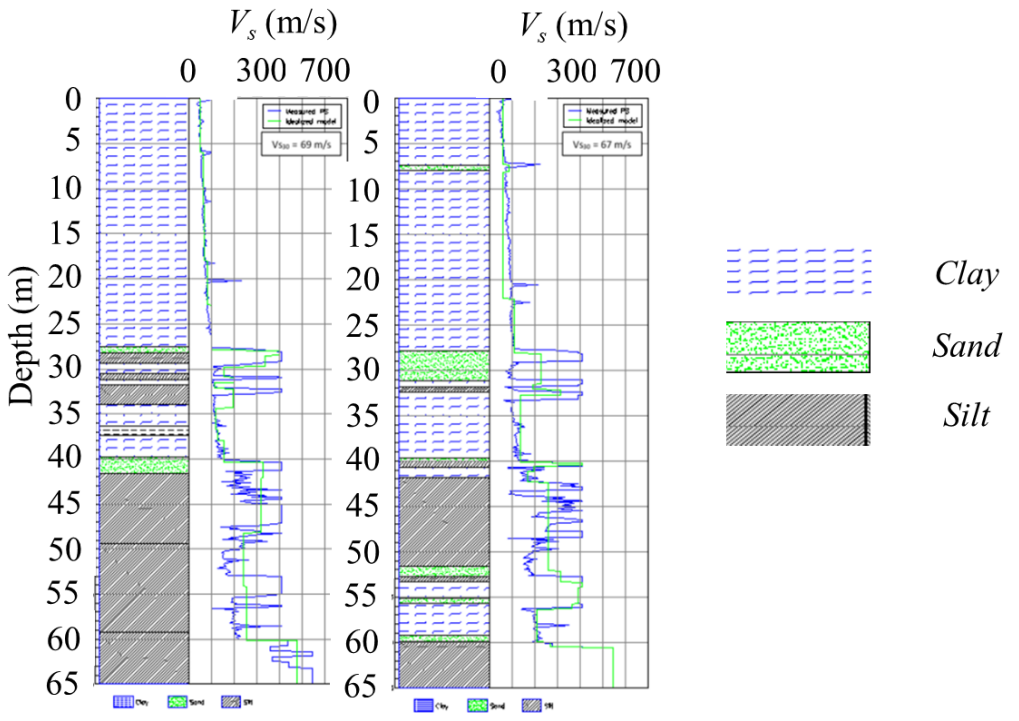

Figure 13. Typical lakebed soil shear wave velocity profiles in Mexico City (From Mayoral et al. 2016)

This is the typical profile for the lake beds: a high impedance contrast, due to the low density, low shear wave velocity UCF and LCF lake sediments overlying the high shear wave velocity high density DD, and a laterally homogenous soft soil layer, a geologic structure indicative of soil amplification that can be modeled with a one-dimensional theoretical transfer function. We model the Mexico City soil profile using the DD as the basement rock because the near surface, high impedance contrast is captured by the HVSR. This layer has a low shear wave

velocity relative to typical bedrock, which is on the order of 1000s of m/s, but there is still a significant impedance contrast of approximately 16.5 because of the very low shear wave velocities of the overlying clays, on the order of 10s of m/s. This impedance contrast is causing the amplification in Mexico City at frequencies of engineering interest: 0.1 – 5 Hz.

2.2.2 Geotechnical zones

The Mexico City ancient lake, high impedance geology made zoning by fundamental site frequency and amplification essential for building code design in response to the 1985 Michoacán earthquake. The City is separated into three geotechnical zones: hill, transition and lake. The hill zone is composed of rock and hard soil with some sandy deposits or soft clays. The transition zone has shallower depths to the DD (< 20 m), greater heterogeneity than the lake zone, and a dipping halfspace. The lake zone is split into four subcategories to improve resolution in the building codes. It is characterized by high plasticity, high water content, low velocity clays which amplify at frequencies depending on the depth to the DD and the shear wave velocity profile (Fig 14; Mayoral et al. 2008; Mayoral et al. 2015; Moisés et al. 2016; Çelebi et al. 2017).

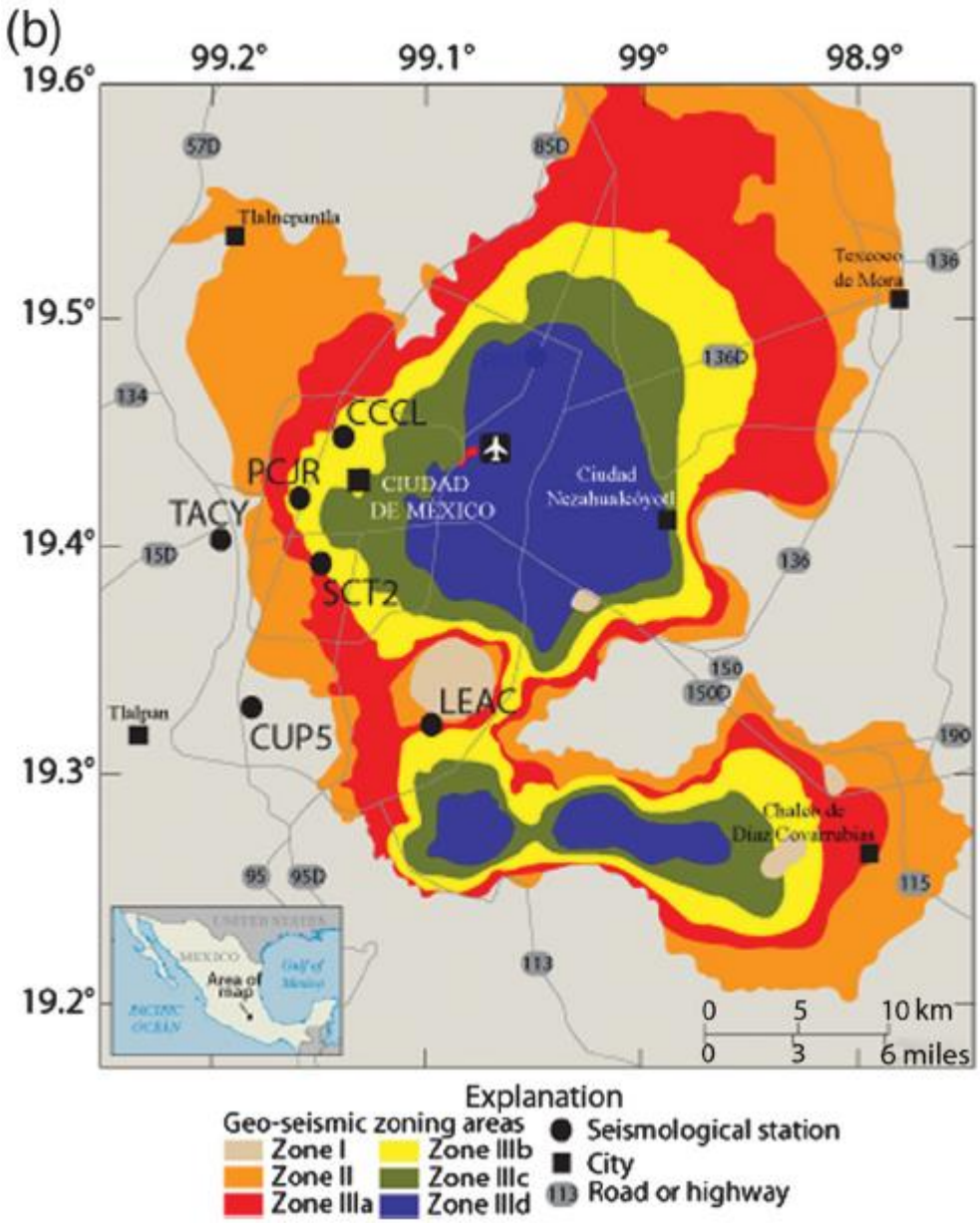

Figure 14. Geotechnical zoning from Çelebi et al. (2017). Zone I is the hill zone, Zone II is the transition zone, Zone IIIa, b, c and d comprise the lake zone (from Çelebi et al. 2017).

2.2.3 Basin structure

The Mexico City basin has 2 distinct areas: the north, which contains one basin with lake sediment filling in Lake Texcoco and the south, which contains two basins, one to the west containing sediment filling Lake Xochimilco and one to the east containing sediment filling Lake

Chalco. The middle of the northern area is roughly 25 km east-west (A-A') and 30 km north south (B-B') through the deepest portion of Lake Texcoco, though there are two longer arms to the northeast and northwest. The middle of the southern area is roughly 35 km across east-west (C-C') and between 8 (D-D') and 15 km (E-E') across north-south, depending on where you measure. Between the northern and southern areas, there is a volcano, Cerro de la Estrella. We can approximate the basin shape by using fundamental site period as a proxy for depth with higher periods equating to a deeper clay layer (Fig. 15; Eq. 2) (Çelebi et al. 2017). The typical depths to the middle of the basin are around 70 m and depths in the transition zone are less than 20 meters (Moisés et al. 2016).

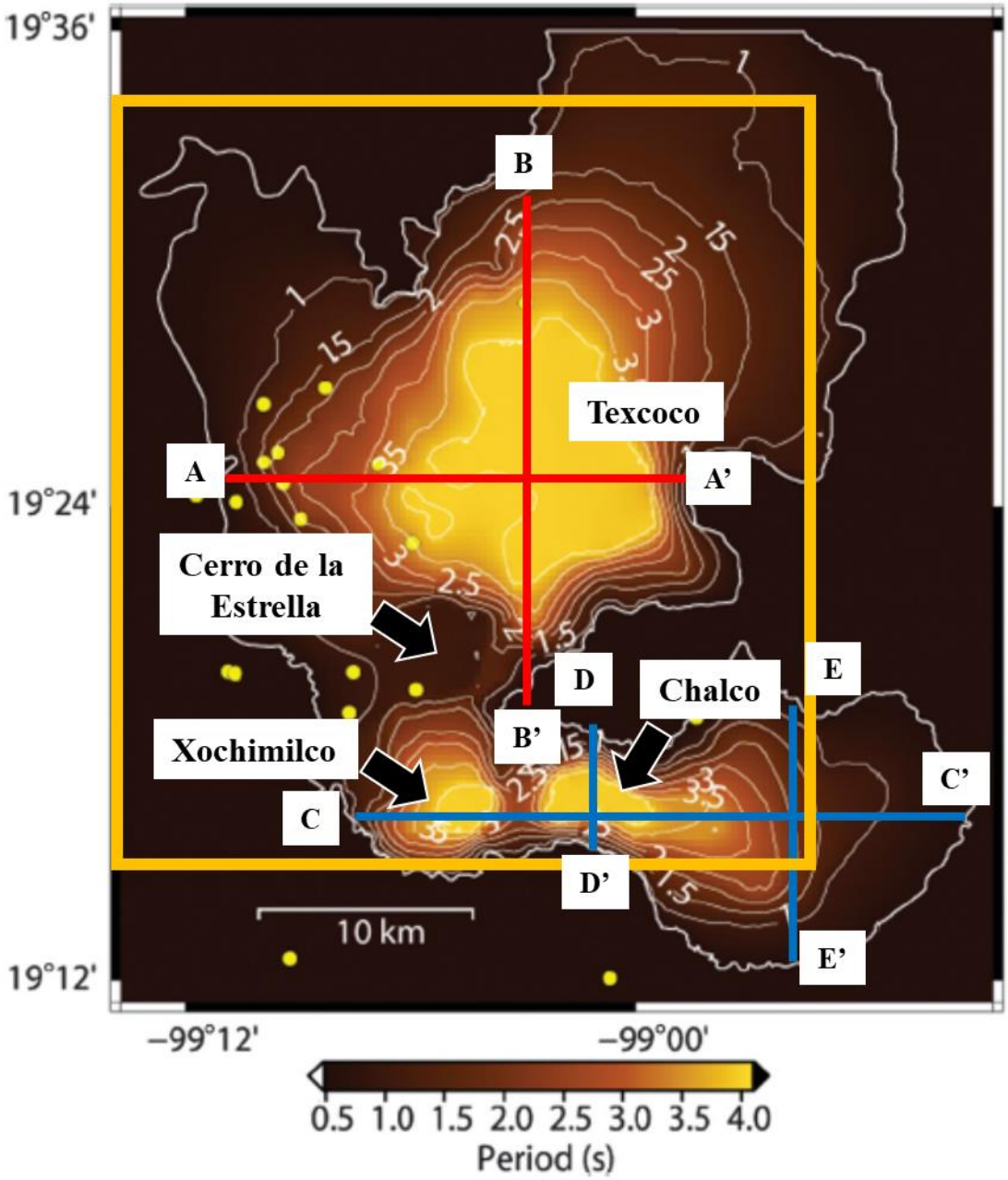

Figure 15. Fundamental period map serving as a proxy for basin shape of Mexico City from Çelebi et al. (2017). The higher longer periods represent deeper parts of the lake. The transects are described in the text and the yellow box is the study area.

3.0 METHODS

3.1 HVSR

3.1.1 Signal processing, magnitude responses and HVSR

We compute $HVSR_{avg}$ from the Mexico City RACM ground motion data using the entire ground motion of each event in the database with PGA < 0.1, the threshold for non-linear shear modulus reduction (Beresnev and Wen, 1996). We apply a two-pole lowpass Butterworth filter (Butterworth, 1930) with a high corner frequency of 49 Hz in the forward and reverse direction to all three components of every record at each station. We then combine the horizontal time records using the two-dimensional (2D) complex time-series (Steidl, 1996)

$$s_H(t) = s_x(t) + is_y(t) \tag{11}$$

where $s_x(t)$ and $s_y(t)$ represent both horizontal components of the record and $s_z(t)$ represents the vertical component of the record. We then take the absolute value of the MATLAB Fast Fourier Transform (Appendix 1) of $s_H(t)$ to compute the horizontal magnitude response. We compute the same for the vertical component $s_z(t)$ and smooth the magnitude responses using a two-way Hamming window average filter with width 0.15 Hz. Next, we compute the HVSR of the record by dividing the combined horizontal magnitude response by the vertical (Fig. 16).

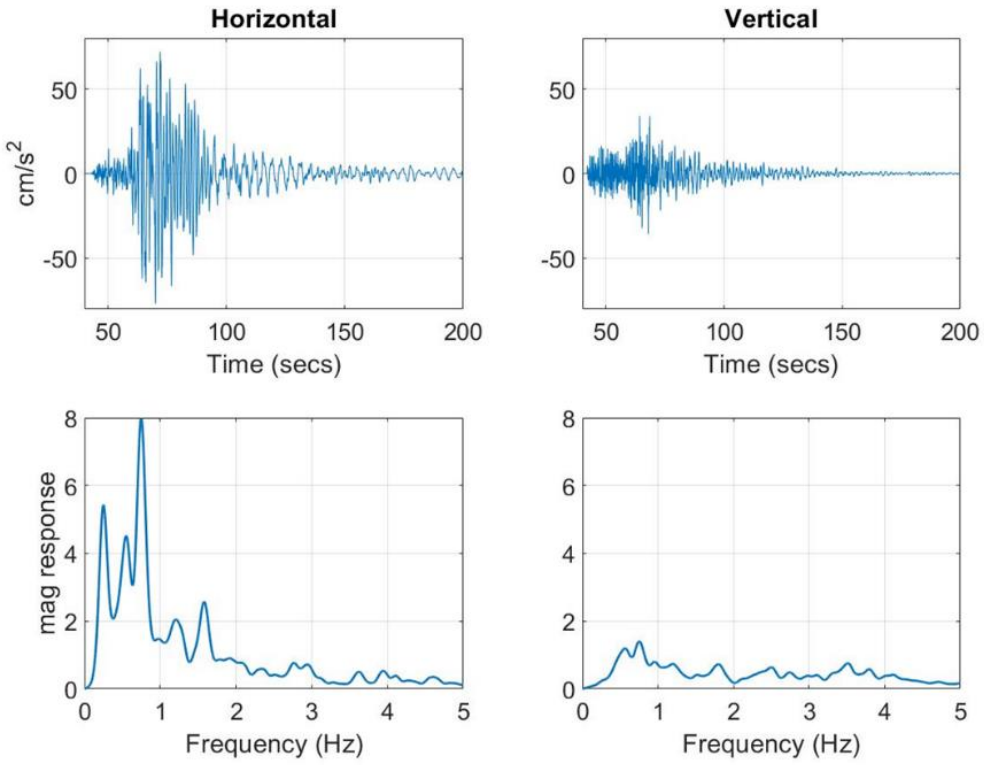

Figure 16. Horizontal and vertical magnitude responses from the waveform from the 2017 Puebla event recorded at lake zone site CE32 in Mexico City. Their ratio is the HVSR.

3.1.2 Computing median, standard deviation and 95% confidence interval

We calculate the median HVSR from all the events recorded at one of the stations in the RACM network using the maximum likelihood estimator:

$$HVSR_{avg}(f) = exp\left(\frac{1}{n}\sum_{i=1}^{n} \ln[HVSR_i(f)]\right) \quad (12)$$

where $HVSR_i(f)$ is the $HVSR(f)$ for i = 1,…,n ground motions. We plot $HVSR_{avg}$ with a large sample 100(1-α) confidence interval:

$$exp\left(\ln\left[HVSR_{avg}(f)\right] \pm z_{1-\alpha/2} \times \sigma_{ln}(f)\right) \quad (13)$$

with standard deviation:

$$\sigma_{ln}(f) = \sqrt{\frac{1}{n}\sum_{i=1}^{n}(\ln[HVSR_i(f)] - \ln[HVSR(f)])^2} \quad (14)$$

(Thompson et al. 2012) (Fig. 17).

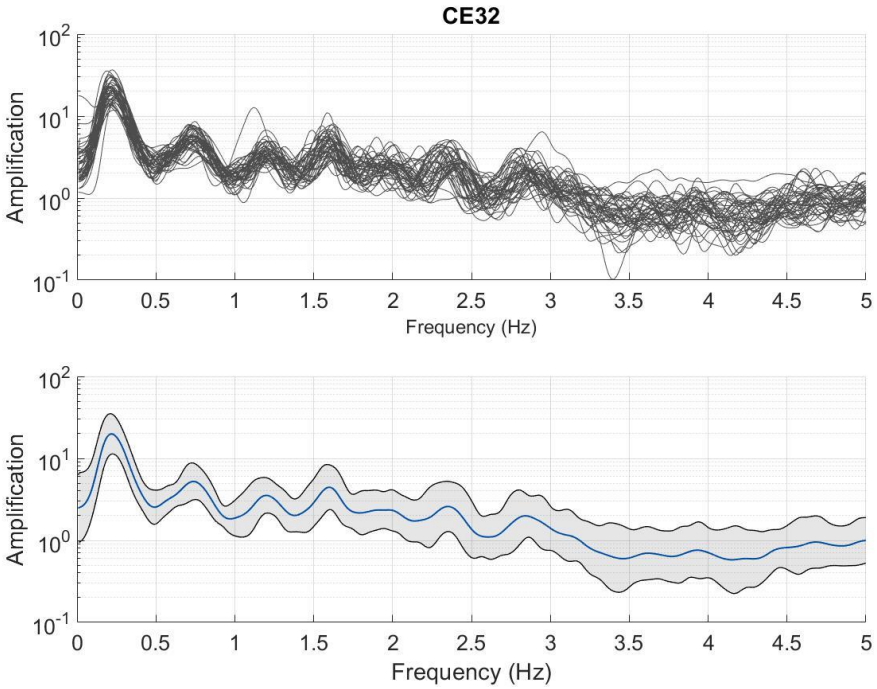

Figure 17. All HVSRs at the same lake zone site as figure with the corresponding averaging from equations 12-14. The grey bars represent the 95% confidence interval.

Hereafter, we refer to $HVSR_{avg}$ as HVSR.

3.2 TTF inversion

The Thompson et al. (2012) statistics require both an empirical transfer function and a theoretical transfer function. In their paper, the authors use the Kik-net database which provides shear wave velocity profiles at each station to use to calculate the site theoretical transfer function. In Mexico City, we do not have access to specific shear wave velocity profiles at each site, so we approximate the soil profile using typical values shown in Figure 2 (Stephenson and Lomnitz,

2004; Mayoral et al. 2016), and use inversion to approximate the TTF based on the HVSR. We assume a two-layer system with upper soil layer shear wave velocity and density 70 m/s and 1.1 g/cm^3 respectively and basement layer shear wave velocity and density 475 m/s and 2.7 g/cm^3 respectively.

To compute the theoretical transfer function, we use the Nrattle Fortran routine, which calculates the Thomson-Haskell plane SH-wave transfer function (Thomson, 1950; Haskell, 1953) for horizontally stratified, laterally homogenous layers with vertically propagating shear waves (written by C. Mueller with modification by R. Herrmann and distributed in the Boore (2005) SMSIM ground motion simulation program). The input parameters for Nrattle are a shear wave velocity profile (β), and corresponding depths (d), densities (ρ) and attenuations (^iQ_s) of the overburden; and the density and shear wave velocity of the basement. The outputs of Nrattle are the TTF amplification as a function of frequency in Hz.

We fit the Thomson-Haskell theoretical transfer function to the HVSR using an objective function which minimizes the sum of squared residuals between each frequency of the TTF and HVSR. We denote the HVSR "y_i" and the TTF "$f(x_i, \beta)$" then the residual r_i between the two is

$$r_i = y_i - f(x_i, \beta) \tag{15}$$

And the sum of squared residuals is

$$S = \sum_{i=1}^{n} r_i^2 \tag{16}$$

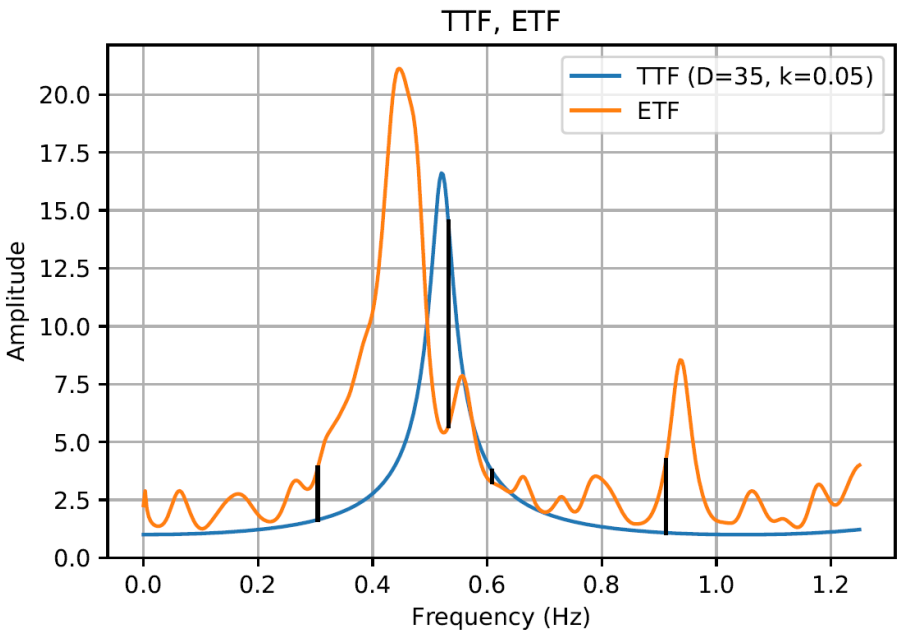

Figure 18. Demonstration of the objective function (Eq. 15). Black lines are residuals r_i, the blue line is a TTF computed from NRATTLE and the orange line is the HVSR computed from H/V analysis from Mexico City ground motion data.

In Figure 18, the orange function is the station HVSR and the blue function is the TTF at a point during the inversion. Selected residuals at three example frequencies are shown in black. The output of the objective function to be minimized is *S*, the sum of the squared residuals across all frequencies. We tested a few minimization techniques on *S* before settling on differential evolution because it required the shortest average amount of time to perform the inversion (Appendix 4.3).

We use the estimates of ρ_1, β_1, ρ_2, β_2 described in section 2.2.1 and invert to solve for the depth and Q^{-1} of the upper soil layer , generating a map of the depth to the high velocity layer and the spatial distribution of damping values across Mexico City, both important for future ground motion simulations. For the remainder of this paper, we convert Q^{-1} values obtained from the inversion into damping values using Equation 6. We use these TTFs at each station to compute the Thompson et al. (2012) statistics using the HVSRs in Mexico City.

3.3 Thompson et al. (2012) statistics

We compute the Thompson et al. (2012) statistics by using the HVSR and its corresponding inverted TTF at each station. We compute the interevent variability by finding the median sigma (Eq. 14) between the station HVSR and the TTF between the first and fourth peaks of the TTF. We compute the goodness of fit to the SH1D TTF by finding Pearson's *r* between the HVSR and the TTF between the first and fourth peaks of the TTF. We then classify each station using the cutoffs provided in Thompson et al. (2012): a σ_i value less than 0.35 is classified as "low" interevent variability, denoted with an "L" and a σ_i value greater than 0.35 is classified as "high" interevent variability, denoted with an "H". An *r* value below 0.6 is classified as a "poor" fit to the SH1D transfer function, denoted with a "P" and an *r* value greater than 0.60 is classified as a "good" fit to the SH1D transfer function denoted with a "G". This yields four classifications: "LG", "LP", "HG" and "HP". We plot each station with interevent variability on the y-axis and goodness of fit to the SH1D transfer function on the x-axis and indicate each quadrant's Thompson et al. (2012) classification.

3.4 Peak identification

To attempt to identify higher resonance in the HVSR beyond the fundamental peak, we systematically define a peak using the MATLAB "findpeaks" function, which identifies each peak in the signal and calculates the "prominence" of a peak. Illustrated in Figure 19, the algorithm finds prominence in the following way: draw a line to the left and right of the peak, indicated by the black arrows in Figure 19 until the line either crosses the signal or reaches the end of the signal. In either of these instances, label the point of crossing either left end or right end, depending on which direction the line is going, indicated by purple squares. Between the peak and these endpoints is called the left or right interval. The lowest point in each of these intervals is called

left and right interval minimum, indicated by orange triangles and the prominence of the peak is defined as the difference between the peak amplitude and the highest interval minimum between the left and right interval minimum, indicated by a lime green line (Fig. 19) (MathWorks, 2019). In this study we define a significant peak as one in which the peak amplitude / $\sqrt{2}$ is greater than the highest interval minimum (Tab. 3). We solve this by defining a significant peak on the condition

$$peak - prominence < peak/\sqrt{2} \tag{17}$$

Peak – prominence is the highest interval minimum.

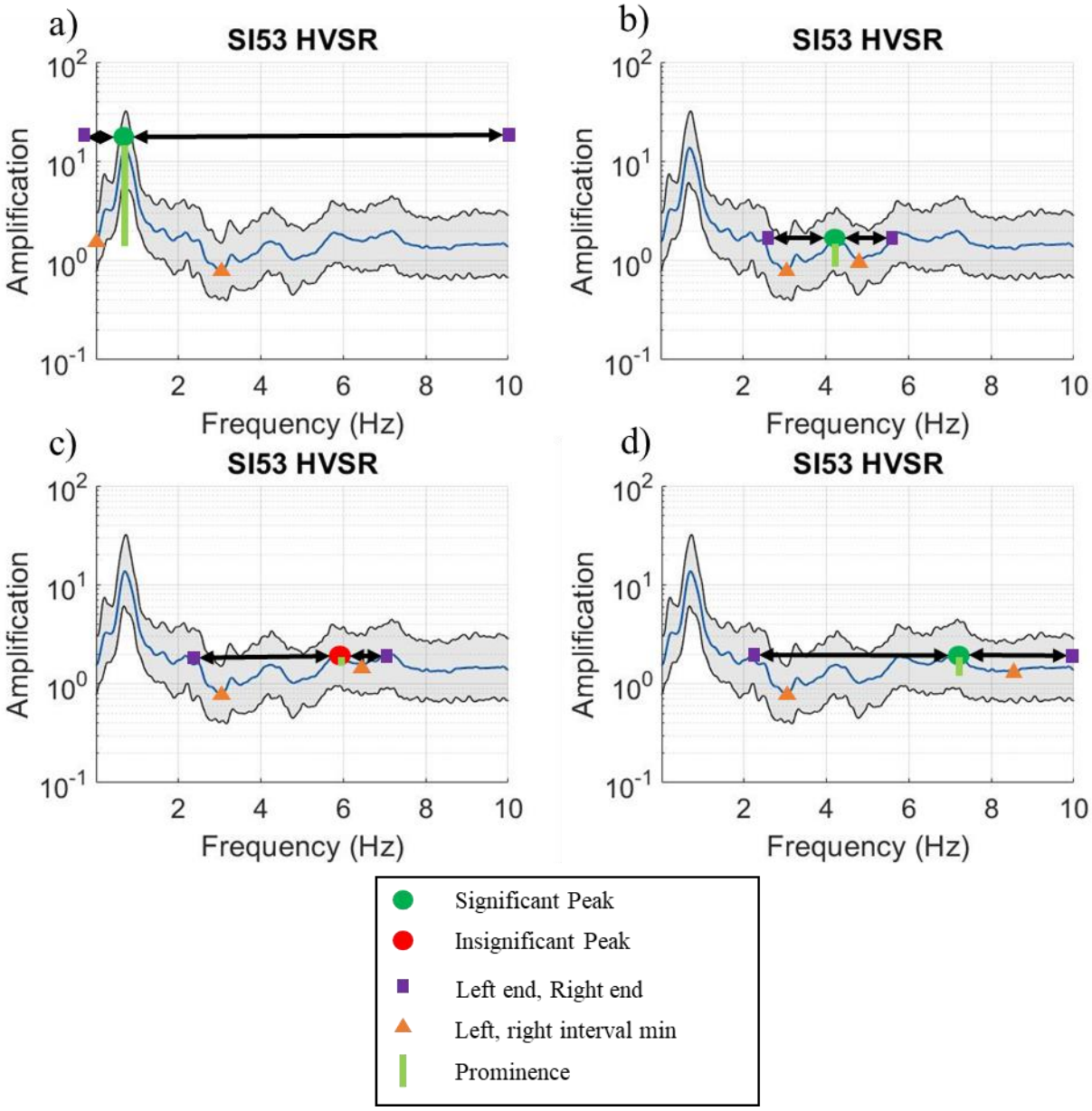

Figure 19. Four selected peaks with their significance, left end and right end, left interval and right interval and prominence indicated. The accompanying table puts values to each identified point. This basic algorithm is how peaks were systematically selected in this study.

	Frequency	amplitude		Frequency	amplitude
Peak 1	0.71	13.69	**Peak 2**	4.24	1.56
Left End (LE)	0	1.53	Left End (LE)	2.53	1.56
Right End (RE)	10	1.39	Right End (RE)	5.56	1.56
Left Interval Minimum (LEM)	0	1.53	Left Interval Minimum (LEM)	3.02	0.78
Right Interval Minimum (REM)	3.02	0.78	Right Interval Minimum (REM)	4.8	1.01
Prominence	12.16		Prominence	0.78	
Highest Minimum	1.53		Highest Minimum	1.01	
Peak amp / sqrt(2)	9.68		Peak amp / sqrt(2)	1.10	
Peak?	Yes		Peak?	Yes	
	Frequency	amplitude		Frequency	amplitude
Peak 3	5.78	1.92	**Peak 4**	5.78	1.93
Left End (LE)	2.2	1.92	Left End (LE)	2.17	1.93
Right End (RE)	7.1	1.92	Right End (RE)	10	1.39
Left Interval Minimum (LEM)	3.02	0.78	Left Interval Minimum (LEM)	3.02	0.78
Right Interval Minimum (REM)	6.46	1.56	Right Interval Minimum (REM)	8.57	1.298
Prominence	1.14		Prominence	1.15	
Highest Minimum	1.56		Highest Minimum	1.298	
Peak amp / sqrt(2)	1.36		Peak amp / sqrt(2)	1.36	
Peak?	No		Peak?	Yes	

Table 3. Accompanying table to Figure 19, assigning values to the points indicated in the figure. If the value "Peak amp / sqrt(2)" is greater than the "Highest Minimum" value, the peak is selected as a peak.

Using this definition of a peak the number of peaks in HVSR at example station SI53 is reduced to 3. We use this value as our statistic to identify stations which display higher modes of resonance in the HVSR: the total number of peaks is the number of peaks in HVSR that are selected using this algorithm.

3.5 Peak shape statistics

In addition to the Thompson et al. (2012) statistics and the number of peaks in the HVSR, we propose and analyze four additional statistics to quantify the shape of the HVSR fundamental peak: 1) the frequency (f_n), 2) amplitude (a), 3) half power bandwidth (HPB), and 4) the interevent variability (σ_i) between the half-power bandwidth of the fundamental peak. The frequency and amplitude of the fundamental peak are computed using the "findpeaks" algorithm. The half power

bandwidth is a definition of the width of the fundamental peak of the transfer function that uses the damping ζ (Eq. 6, section 5.3.3). As illustrated in Figure 20, we compute the half power bandwidth by dividing the amplitude of the fundamental peak by $\sqrt{2}$, drawing a horizontal line at this value, and recording the corresponding frequencies f_a and f_b that intersect the $1/\sqrt{2}$*amplitude line. The difference between f_a and f_b is the half power bandwidth (Fig. 20a) (Chopra, 2007). To compute the inter-event variability, we compute the standard deviation of the HVSR at each frequency and find the median standard deviation value between f_a and f_b (Figure 20b). We compute this definition of the interevent variability between each f_a and f_b at each HVSR fundamental peak.

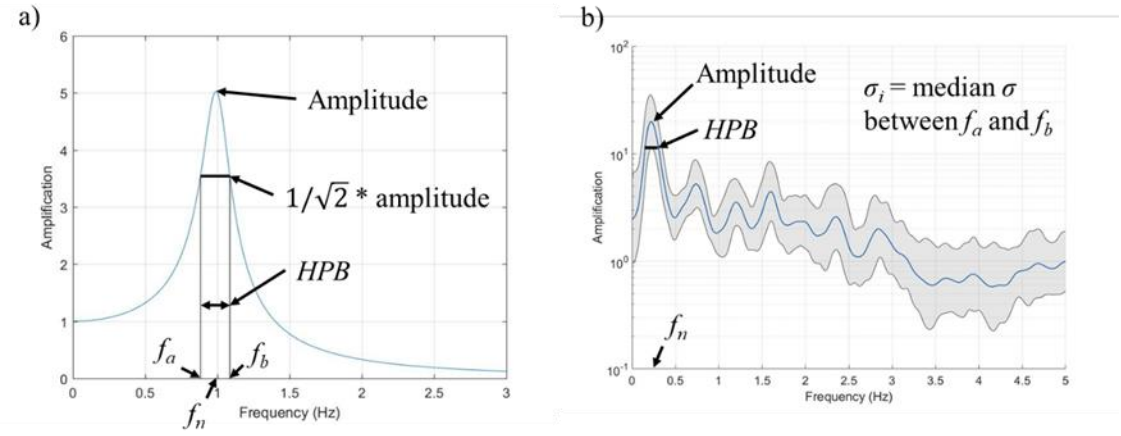

Figure 20. a) Example of *HPB* computation of a transfer function with $\zeta = 0.1$ as a measure of the width of the fundamental peak. b) Mexico City lake zone station HVSR with amplitude, *HPB*, and f_n. The σ_i value is the median standard deviation between f_a and f_b.

3.6 Peak finding and statistics system design

We store the Mexico City RACM network database in two layers: an upper layer with a directory of station folders and a lower layer containing all the event datafiles recorded at that station. We open the station folder, read the datafiles and perform the HVSR as is described in section 3.1. Then, we compute the average, standard deviation and 95% confidence interval at each

frequency and plot. We define significant peaks of this HVSR and determine the fundamental peak shape statistics (Fig. 21). Finally, we analyze the peak shape statistics spatially and correlate to local geologic complexity (Fig. 22). In this study, we look at the spatial variation of the statistics of the fundamental peak of each station.

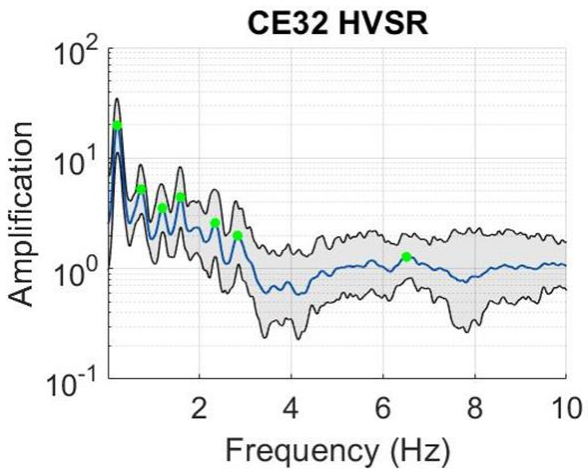

CE32				
Peak #	fn	a	HPB (Hz)	σ
1	0.22	19.77	0.12	0.28
2	0.74	5.22	0.20	0.24
3	1.20	3.53	0.20	0.26
4	1.60	4.44	0.16	0.33
5	2.35	2.59	0.24	0.40
6	2.84	1.99	0.28	0.36
7	6.52	1.28	2.54	0.31

Figure 21. Significant peaks and the output table of their corresponding shape statistics for Mexico City Lake zone station CE32. We include peak shape statistics for all seven peaks at station CE32 though in this study, we only analyze the shape statistics of the fundamental peak.

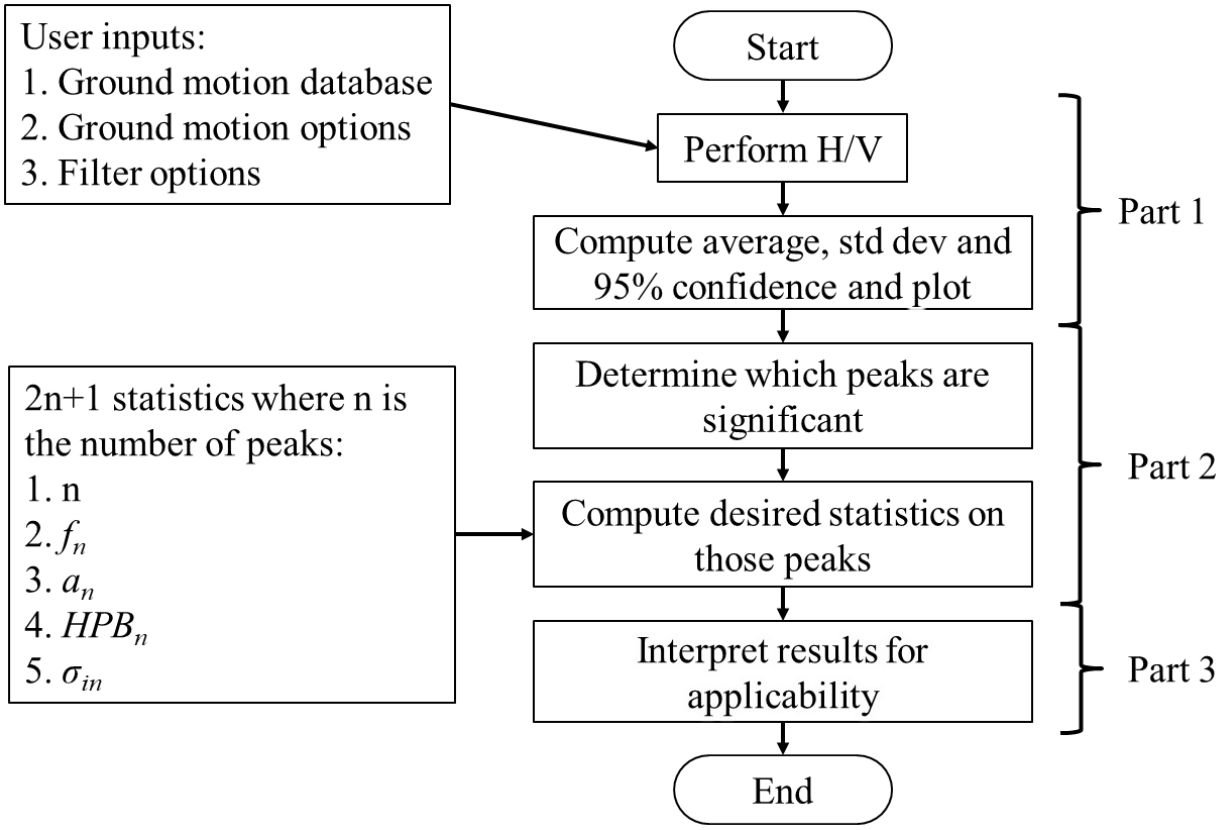

Figure 22. Workflow diagram for the HVSR shape statistics system.

The codes for this algorithm are contained in the Github repository:

https://github.com/mpontrelli/HVSR.

4.0 RESULTS

4.1 Inversion results

The inversion of the HVSR onto a TTF using the soil profile in Figure 2 yields depths ranging from 8.5 to 95 meters (Fig. 23a) and damping values ranging from 1.3 to 5% with an average of 2.9% (Fig. 23b). The depth values increase from the basin edge to the middle of the basin, as expected from the description of the basin shape given in Moisés et al. (2016) (Fig. 39) and the damping values decrease from the basin edge to the center of the basin. The inversion program successfully finds each HVSR fundamental peak and, in some cases, correlates to higher modes of resonance if the station HVSR displays them. The TTFs are not, however, able to capture the widths of the HVSR in either the transition zone stations or the lake zone stations. The amplitudes of the TTFs are correlated to the damping, with higher damping values yielding smaller amplitudes of the fundamental peaks. The TTFs are presented with their corresponding HVSRs in section 4.2 and a table with their depth and damping values are in the appendix (Tab. 5).

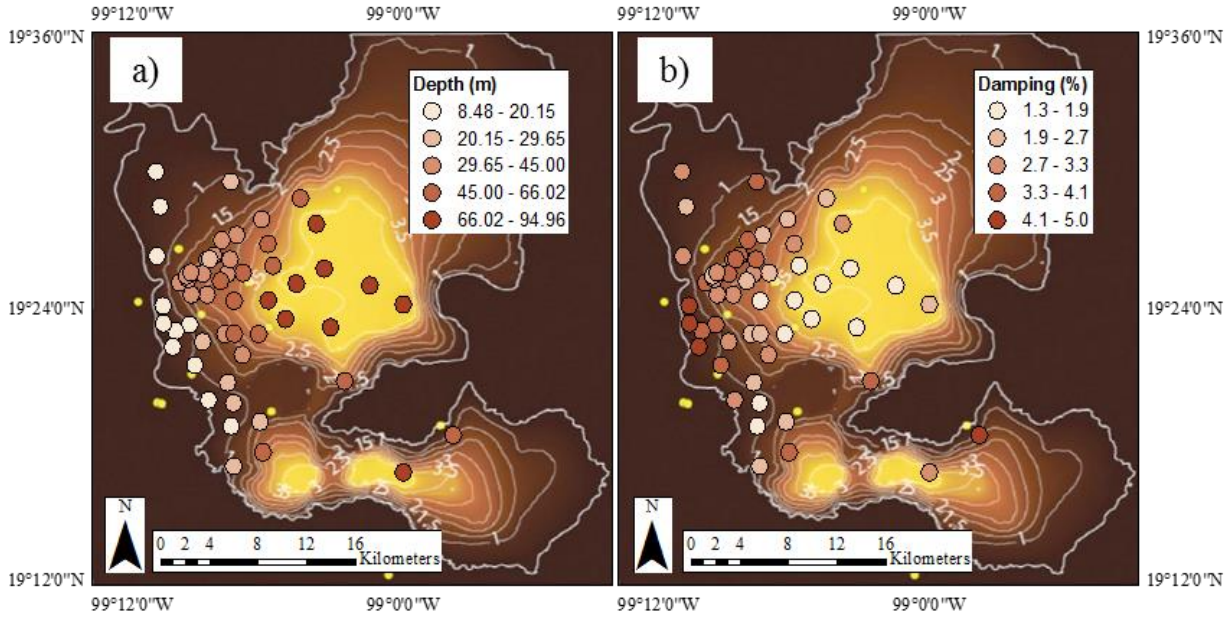

Figure 23. Results from the inversion of the HVSR onto a TTF a) depth in meters b) damping in percent.

4.2 Thompson et al. (2012) statistics

The differential evolution inversion program generates TTFs that capture the fundamental peaks of the HVSRs at the stations in the Mexico City basin. Using the cutoffs from the Thompson et al. (2012) taxonomy for good vs. poor and low vs. high goodness of fit to the SH1D transfer function and interevent variability respectively, most of the stations in the Mexico City RACM network plot in the LP quadrant, second most in the HP quadrant, third in the LG quadrant and fourth in the HG quadrant. The transition zone stations all plot within a cluster between 0.30 and 0.40 σ_i and 0.50 and 0.70 r (Fig. 24).

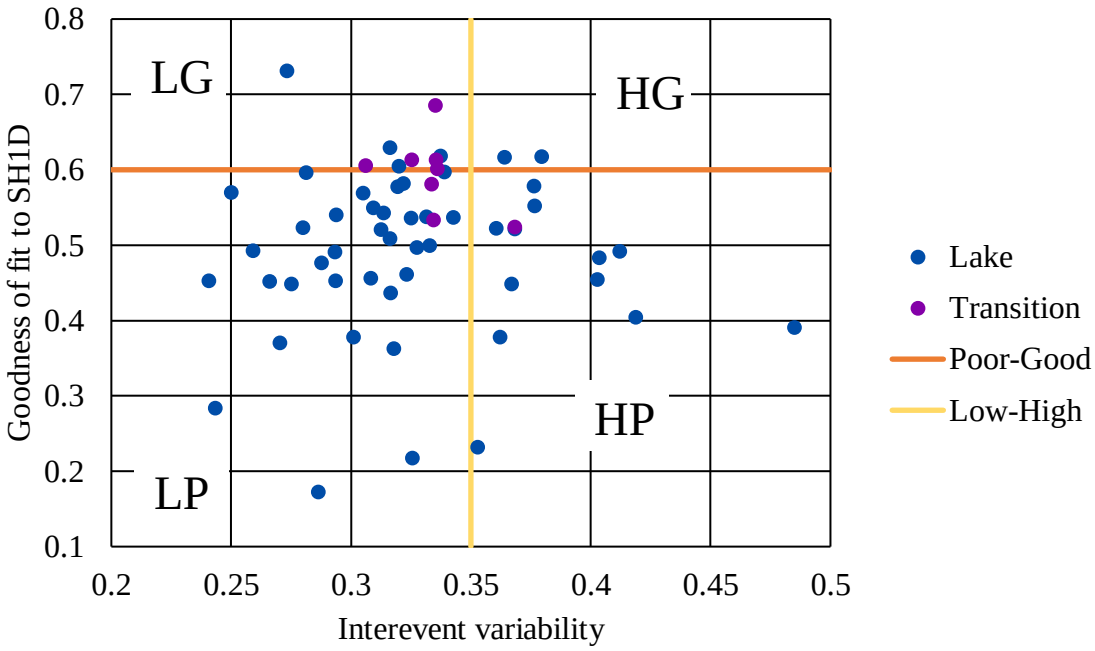

Figure 24. Lake and transition zone station HVSRs in this study plotted with their Thompson et al. (2012) statistics. Lines on the chart are the cutoffs for good or poor fit to the SH1D transfer function and low or high interevent variability. These lines form four quadrants which are the Thompson et al. (2012) taxonomy statistics: LG, HG, LP and HP.

All the TTFs have higher modes while in many cases the HVSRs do not (Figs 25; 26; 27; 28). The fundamental peak of the TTFs tends to be much wider than the fundamental peak of their corresponding HVSR. There are 9 stations in the LG quadrant: CA20, CC55, CJ03, MY19, AO24, CO47, DR16, EO30 and ES57. Of these, four are lake zone stations indicated in blue and five are transition zone stations, indicated in purple in Figure 25. Their inverted theoretical transfer functions are plotted in black. These stations have higher modes that show up in the HVSR and correlate to the higher modes of resonance in the TTF. These higher modes in the HVSR, however, still tend to have lower amplitudes than the higher modes of their corresponding TTF. MY19 in the lake zone, for instance, has an HVSR with several higher modes which match up peak to peak and trough to trough with its TTF. The MY19 *r* value is 0.73, a high correlation reflecting matching higher modes of resonance. Even with the high inverted damping value of 4.05% which decreases

the higher mode TTF amplitudes, however, the HVSR higher mode amplitudes are still lower than the higher mode TTF amplitudes. This high TTF damping is displayed in MY19 as the black line tailing off significantly at higher frequencies.

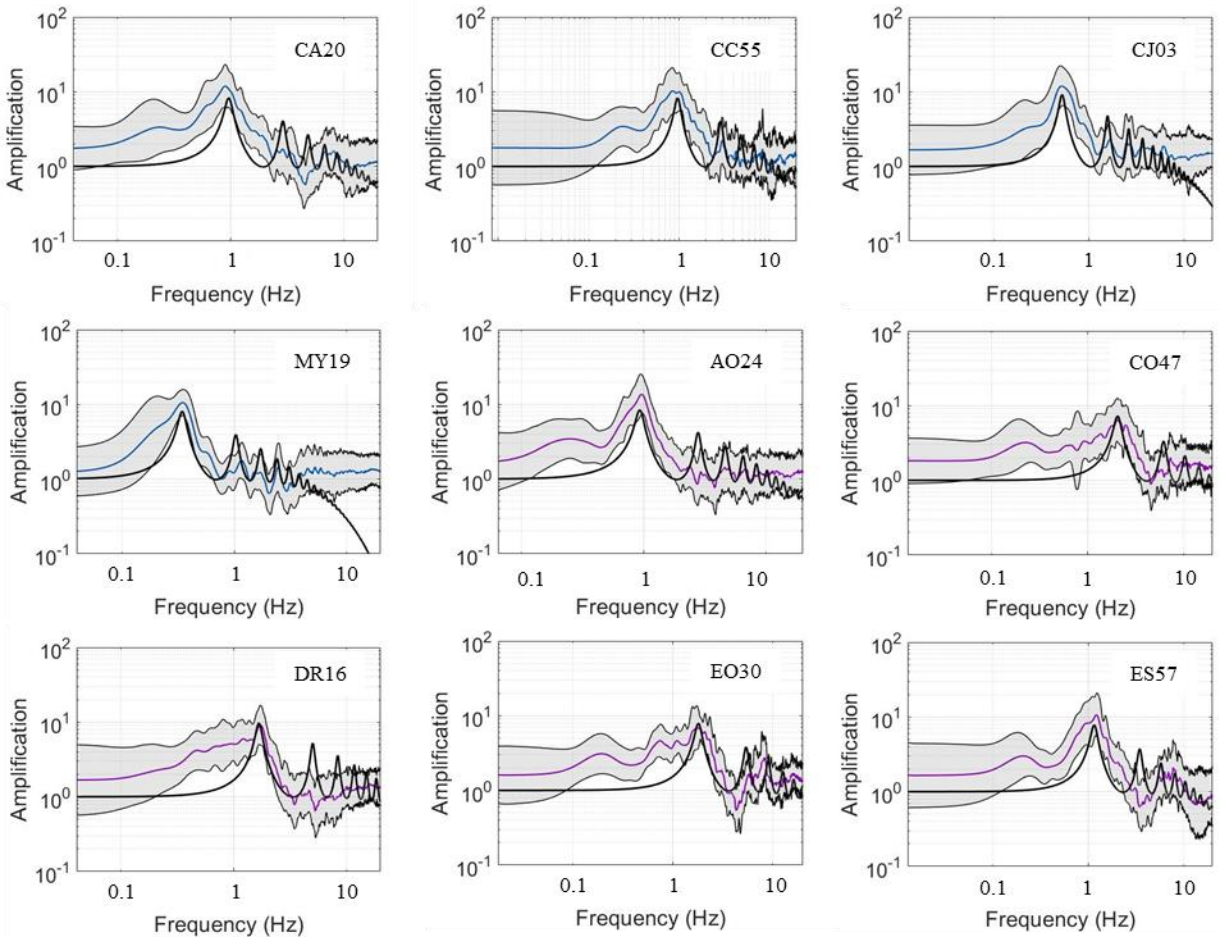

Figure 25. Nine stations classified as LG by the Thompson et al. (2012) statistics. Their HVSR is indicated in blue (lake zone) or purple (transition zone station) and their inverted TTF is in black.

To see how the other stations behave at lower *r* values, we shifted the poor-good line in Figure 24 down to an *r* value of 0.55 and plotted the stations that fall in this portion of the LP space: seven stations in total, six classified as lake zone stations and one classified as a transition zone station (Fig. 26). Some of these stations display higher resonance peaks like stations CE32, which has higher mode amplitudes comparable to that of the TTF, CJ04 which has one higher

mode peak of comparable amplitude to the TTF and CB43 which has a broad set of peaks at its second mode. In general, these stations still tend to have lower amplitude higher modes and some, like ME52 and DX37 have no evidence for higher modes of resonance. The stations displaying small amounts of resonance increase their Thompson et al. (2012) goodness of fit to the SH1D *r* values.

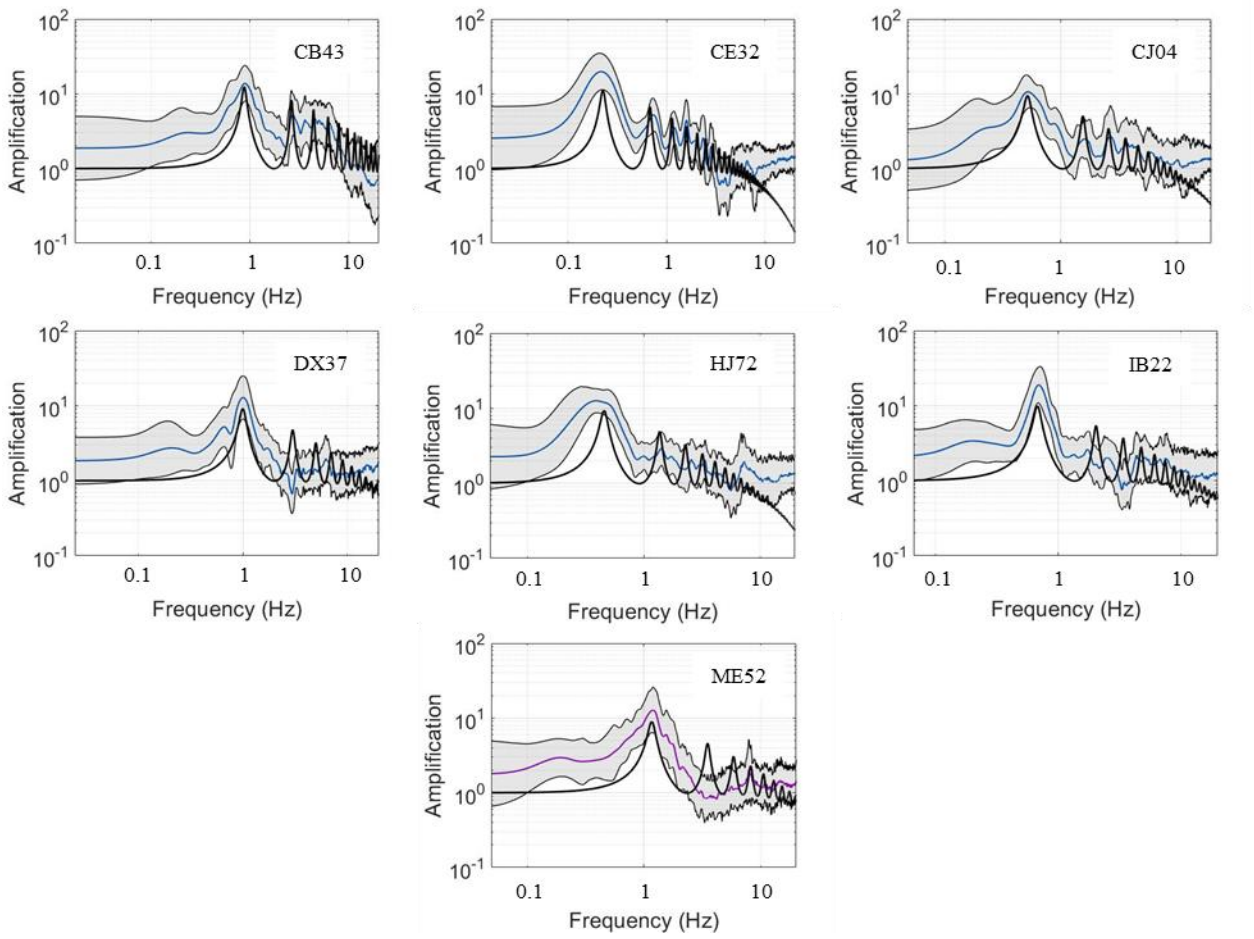

Figure 26. Seven stations classified as LP by the Thompson et al. (2012) statistics except the value of *r*, the interevent variability, is between 0.55 and 0.60. Their HVSR is indicated in blue (lake zone) or purple (transition zone station) and their inverted TTF is in black.

We expected the HVSR to have a single peak due to the influence of the Rayleigh wave term correction in Nakamura's derivation of the HVSR (Eq. 9). Some of the shown LG stations, and LP stations with $r > 0.55$ however, have high goodness of fit to the SH1D transfer function

and higher mode resonances being picked up by the HVSR. Their higher mode amplitudes tend, however, to be lower than the higher mode amplitudes of the TTF with some exceptions. Since the Thompson et al. (2012) statistics are designed to calculate statistics between the first and fourth peaks of the TTF, they may not serve as good a tool for HVSR shape classification as a scheme in which statistics are only computed at the fundamental peak. Though the HVSR is designed to image only one peak, The Thompson et al. (2012) statistics do allow us to parse out some similarities between the HVSR shape and that of an inverted TTF with a 2-layer SH1D soil model of varying depth and damping.

4.2.1 Transition zone stations

The transition zone stations have higher fundamental frequencies and larger half power bandwidths than the lake zone stations and don't have any stations, such as MY19 and CE32 that display as many higher modes of resonance. Some of them display higher resonance peaks but often not as pronounced as in the lake zone. There are no transition zone stations that fall in the HG quadrant of the Thompson et al. (2012) taxonomy and all the stations are clustered together in Figure 24 indicating that their HVSRs are very similar in shape. When compared to the TTF computed from the inversion, the HVSRs in the transition zone tend to have *r* values around 0.60 but this is a bias from the strong correlation with the fundamental peak (Fig. 27), not the *r* value capturing the higher modes. We show all eight transition zone stations: AO24, AU46, CO47, DR16, EO30, ES57, GR27 and ME52, and their accompanying TTF in Figure 27. Stations AU46, EO30 and ES57 display a significant second mode peak whereas station GR27 has a more expected HVSR, that is, a single peak with no significant peaks at higher modes.

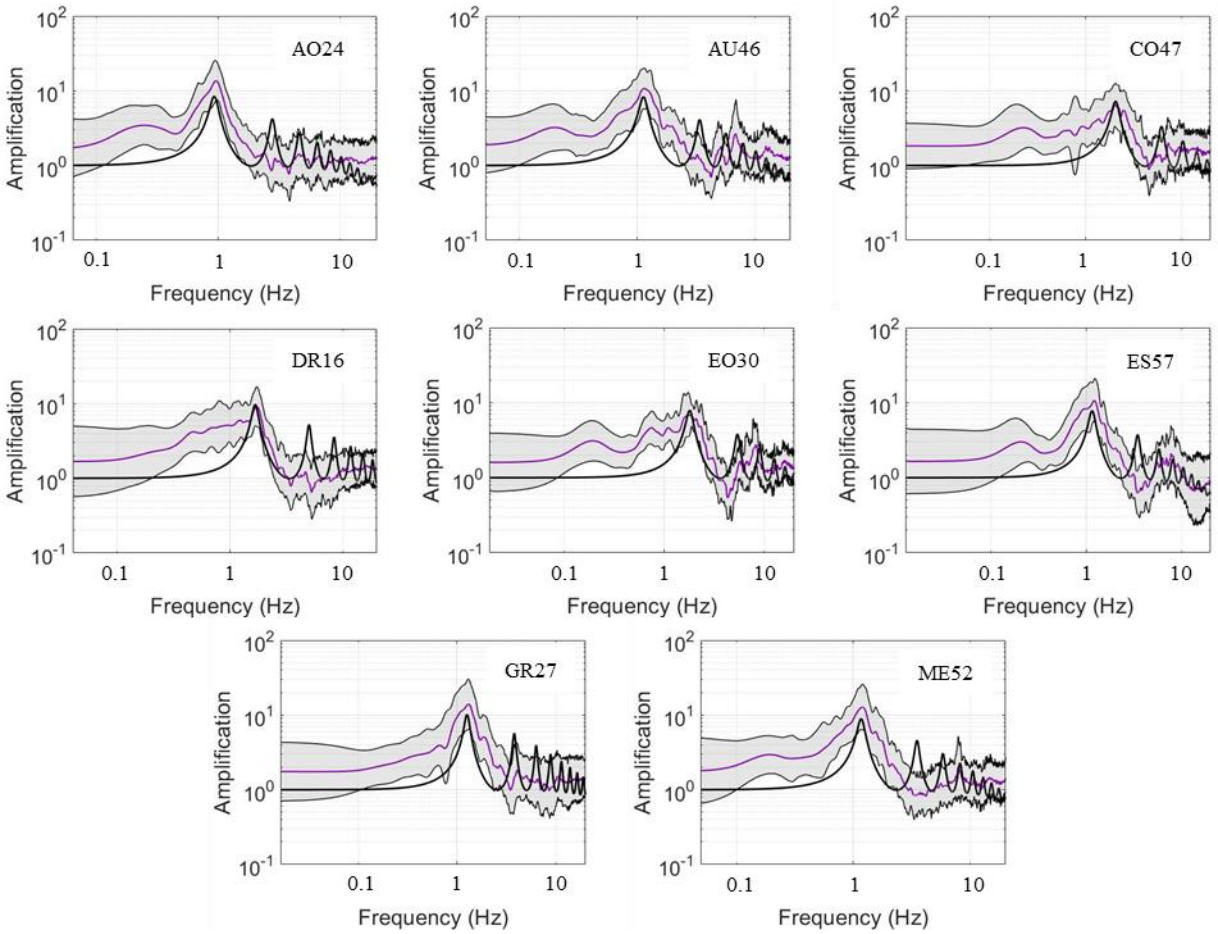

Figure 27. All the transition zone stations in the RACM network their classifications are AO24: LG, AU46: LP, CO47: LG, DR16: LG, EO30: LG, ES57: LG, GR27: HP and ME52: LP.

4.2.2 Lake zone stations

Lake zone stations have lower fundamental frequencies and thinner halfpower bandwidths than transition zone stations. A few have HVSRs with several higher modes of resonance such as CE32, MY19, CJ04 and AU11. We show 2 stations from each classification of the Thompson et al. (2012) taxonomy (Fig. 28). In the lake zone, several stations have HVSRs that are well modeled by the single layer over halfspace SH1D model with high correlation to the TTF and low interevent variability. For example, station MY19 has an HVSR with four peaks that match the SH1D transfer function peaks. This station also has a low interevent variability. We observe several stations like

this in the lake zone that have peaks that are close together and well modeled by the SH1D TTF. Some stations, however, like AE02 (LP) and EX09 (HP) are poorly modelled by the SH1D TTF. These stations have one or two peaks that are identified by the peak finding algorithm and therefore don't have higher modes of resonance, bringing down the *r* value.

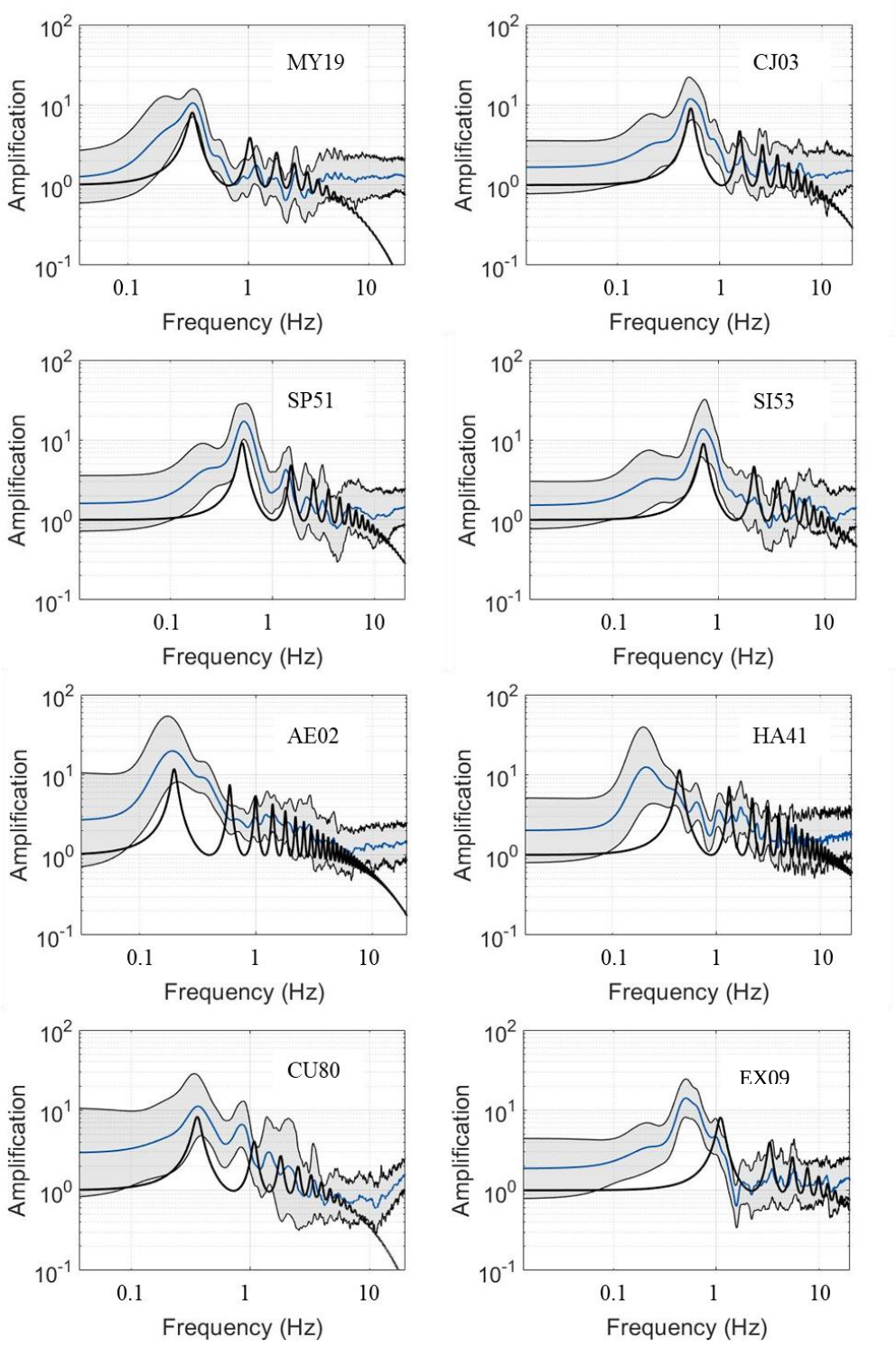

Figure 28. Lake zone stations with the four Thompson et al. (2012) taxonomy classifications 1st row) LG, 2nd row) HG, 3rd row) LP and 4th row) HP. The black lines are the TTF derived from the inversion.

The median interevent variability for the Thompson et al. (2012) statistics is slightly lower in the lake zone than in the transition zone but the data are more scattered with some σ_i values as low as 0.25 and some as high as 0.5. The goodness of fit to the SH1D transfer function values in the transition zone are consistently higher in the transition zone than the lake zone (Fig. 29).

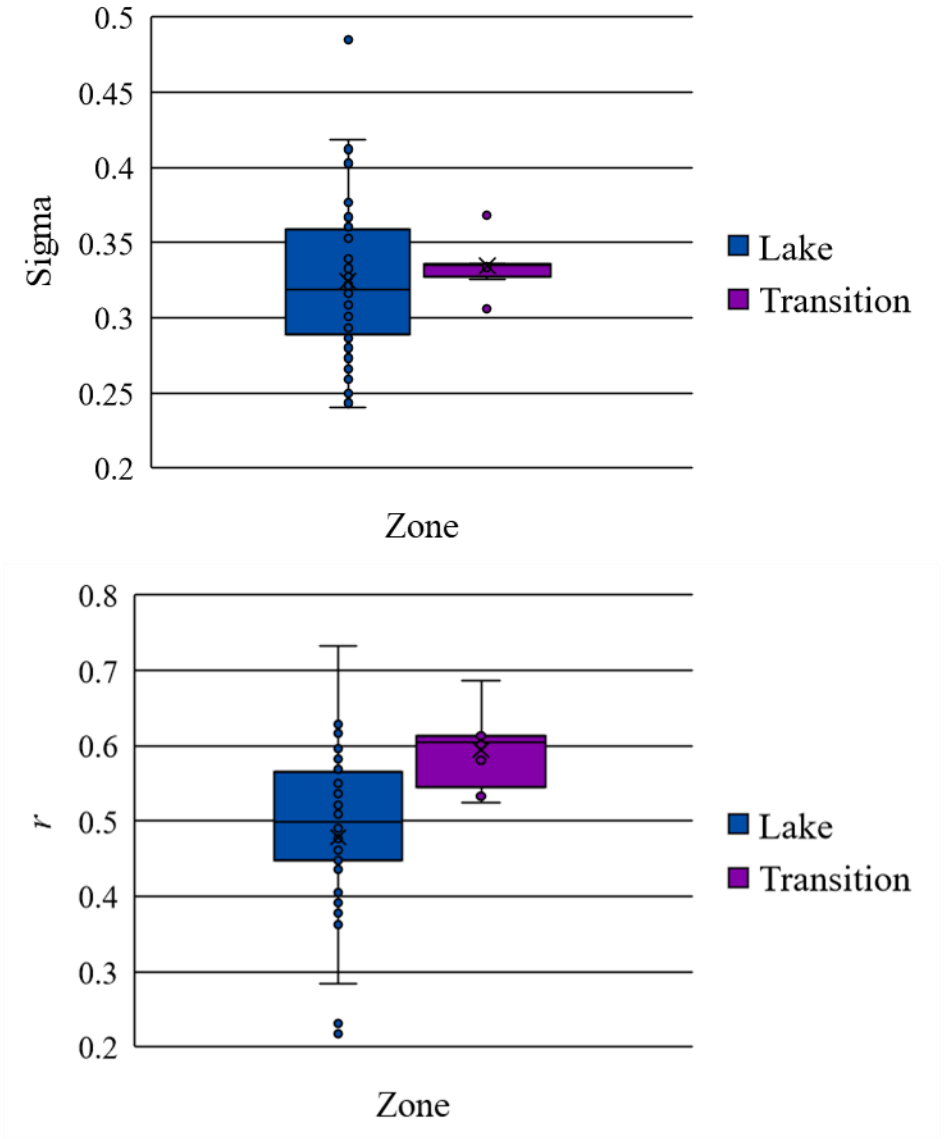

Figure 29. Box and whisker plots with the Thompson et al. 2012 statistics in the transition (purple) and lake (blue) zones a) interevent variability b) goodness of fit to the SH1D.

Most of the LP stations fall within the lake zone and most of the LG stations fall in the transition zone. There are several pockets of HP stations, indicated in red which identify areas of geologic complexity, significantly differing from our 2-layer SH1D model.

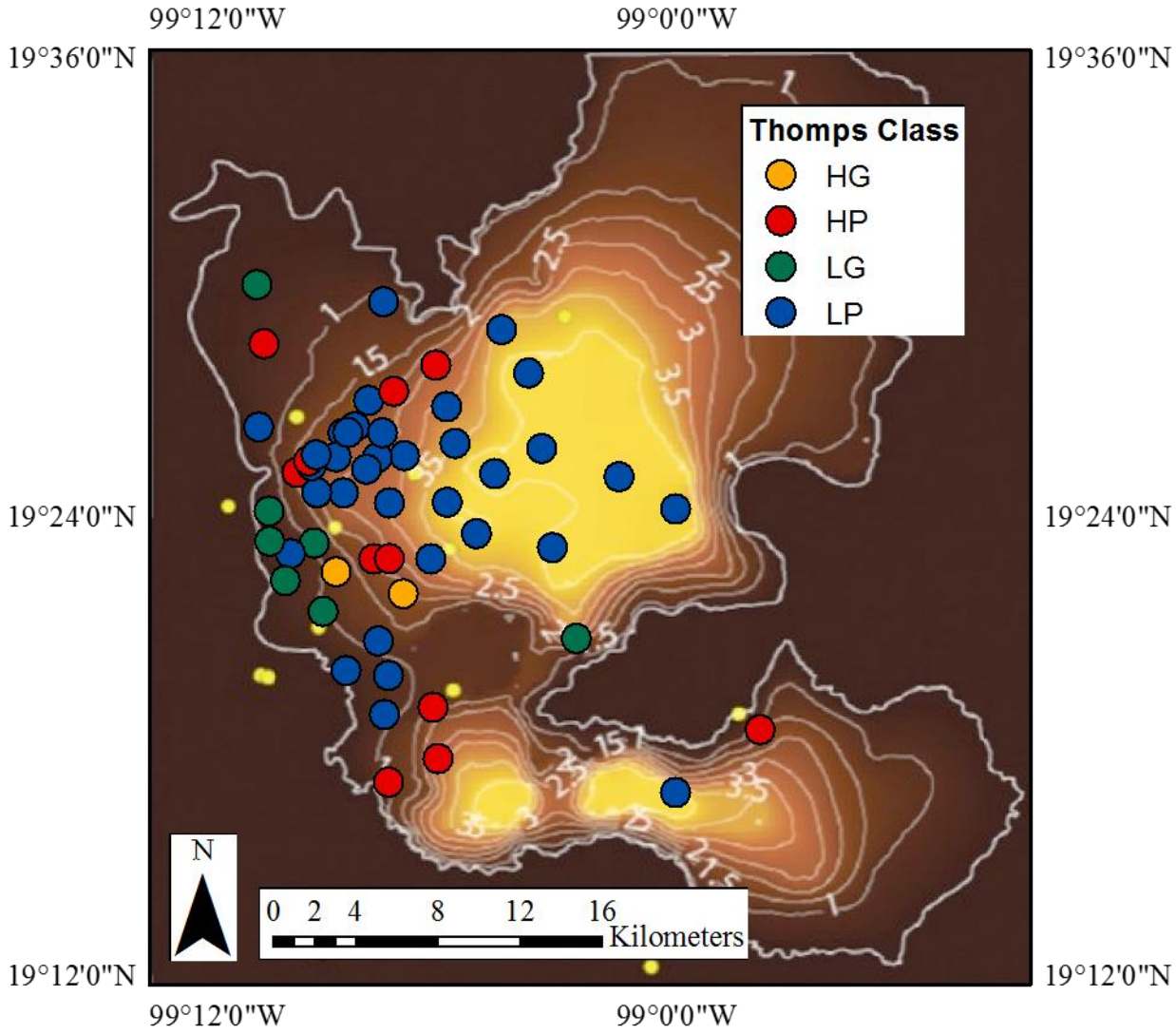

Figure 30. Thompson et al. (2012) classifications for Mexico City using an inverted TTF to match the HVSR.

4.3 Transect using HVSR shape statistics

Since the HVSR is used to image the fundamental peak of the SH1D transfer function, we classify this fundamental peak using the fundamental frequency, amplitude, half power bandwidth and interevent variability between the half power bandwidth. Using these statistics, we analyze just the fundamental peak shape as opposed to the broader frequency range analyzed by the Thompson et al. (2012) statistics. We compute the HVSR shape statistics along a transect running from west to east across the Mexico City basin starting in the transition zone and ending in the lake zone using stations CO47, SI53, PE10, VM29, AU11 and CE32. These stations in the transect generally have an increasing number of significant peaks, decreasing fundamental frequency, increasing amplification, decreasing half power bandwidth and no trend in sigma of their fundamental peak (Figs. 31; 32; 33; 34).

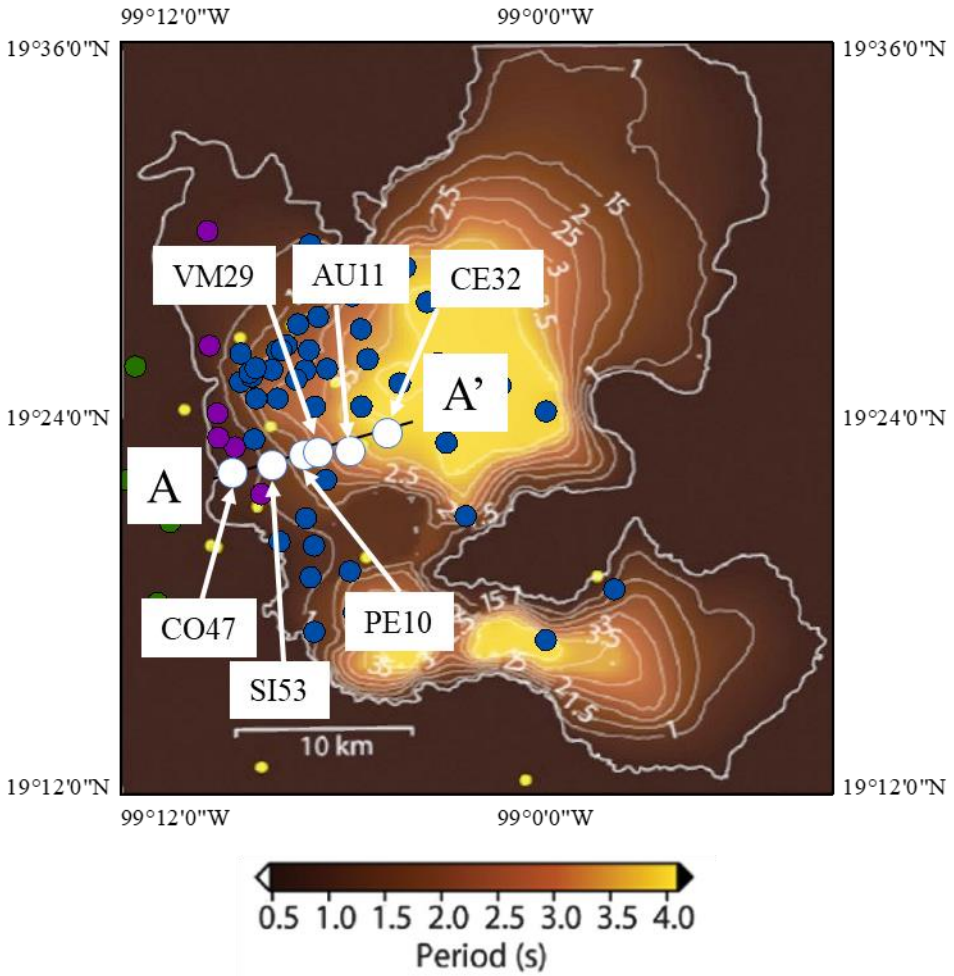

Figure 31. Transect A-A' running east-west across the Mexico City basin. Stations are indicated with a white dot and their corresponding HVSRs are plotted in the following figure.

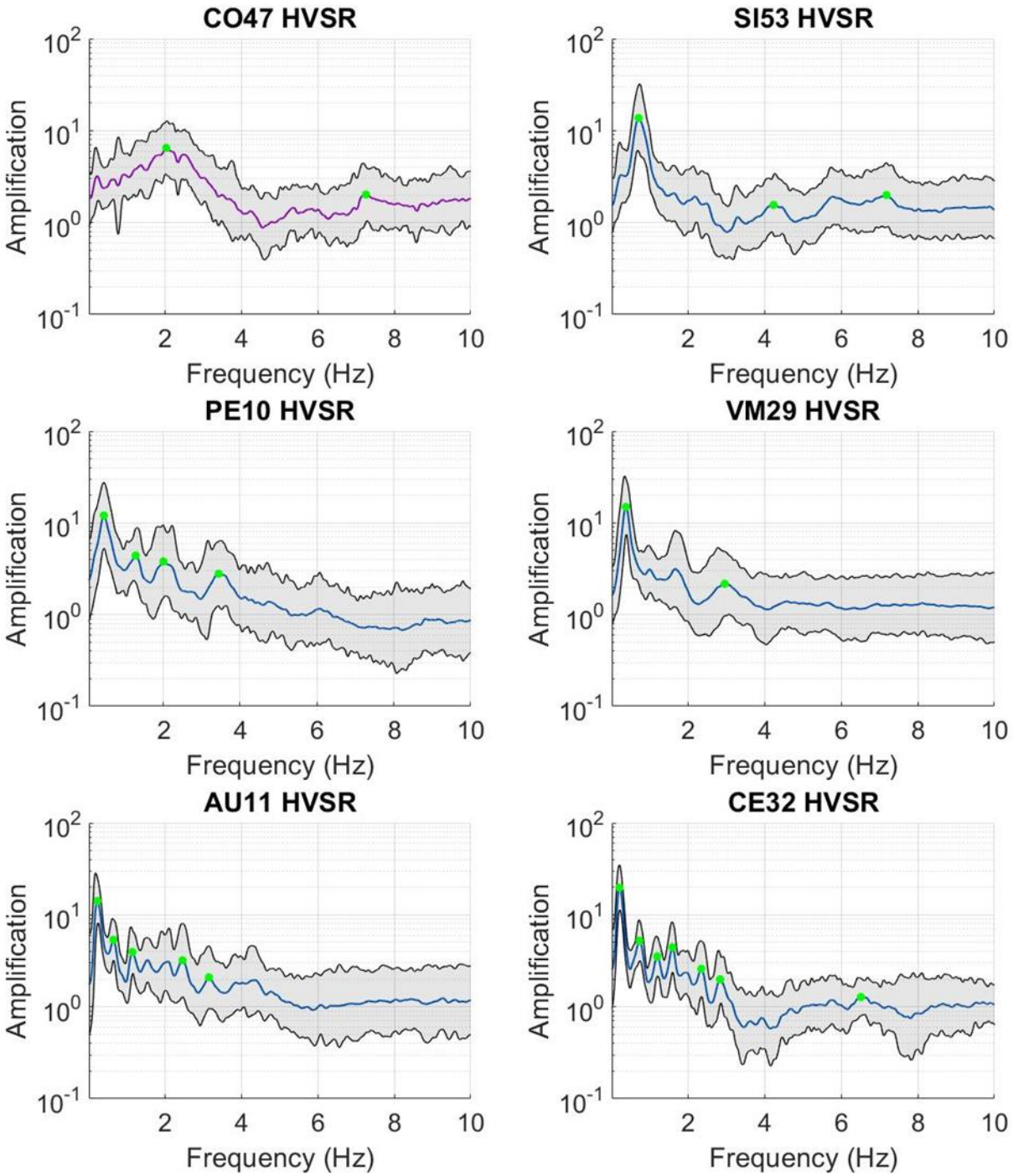

Figure 32. HVSRs of the stations along the transect the green dots indicate the significant peaks. These are plotted without a logarithmic x-axis to highlight the thinning fundamental peak from transition to lake zone.

Station	Lat	Lon	Distance	Depth	# Peaks	f_n	a	HPB	σ_i
CO47	19.37	-99.17	0	-8.58	2	2.04	6.49	0.67	0.34
SI53	19.38	-99.15	2.35	-24.51	3	0.71	13.69	0.25	0.40
PE10	19.38	-99.13	4.19	-38.42	4	0.46	12.05	0.21	0.43
VM29	19.38	-99.13	4.90	-45.61	2	0.38	14.96	0.15	0.38
AU11	19.38	-99.11	6.81	-74.83	5	0.23	14.13	0.14	0.28
CE32	19.39	-99.09	9.23	-80.32	7	0.22	19.77	0.12	0.28

Table 4. Peak statistics computed for the fundamental peak of each HVSR along the transect.

We compute the depths using Eq. 2 and the fundamental frequency of the station HVSR. This transect has a consistently increasing depth from CO47 to CE32, reflected by the shape of the HVSR.

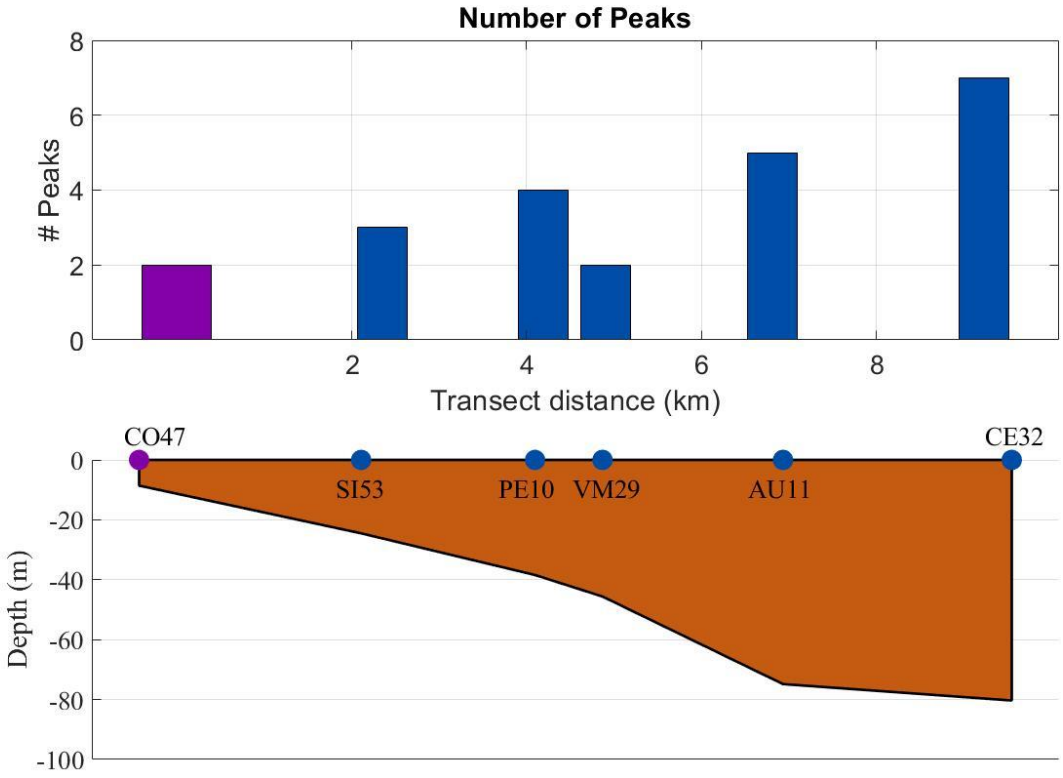

Figure 33. Number of peaks at each station in transect A-A'. The depths are computed using the relationship in Equation 2.

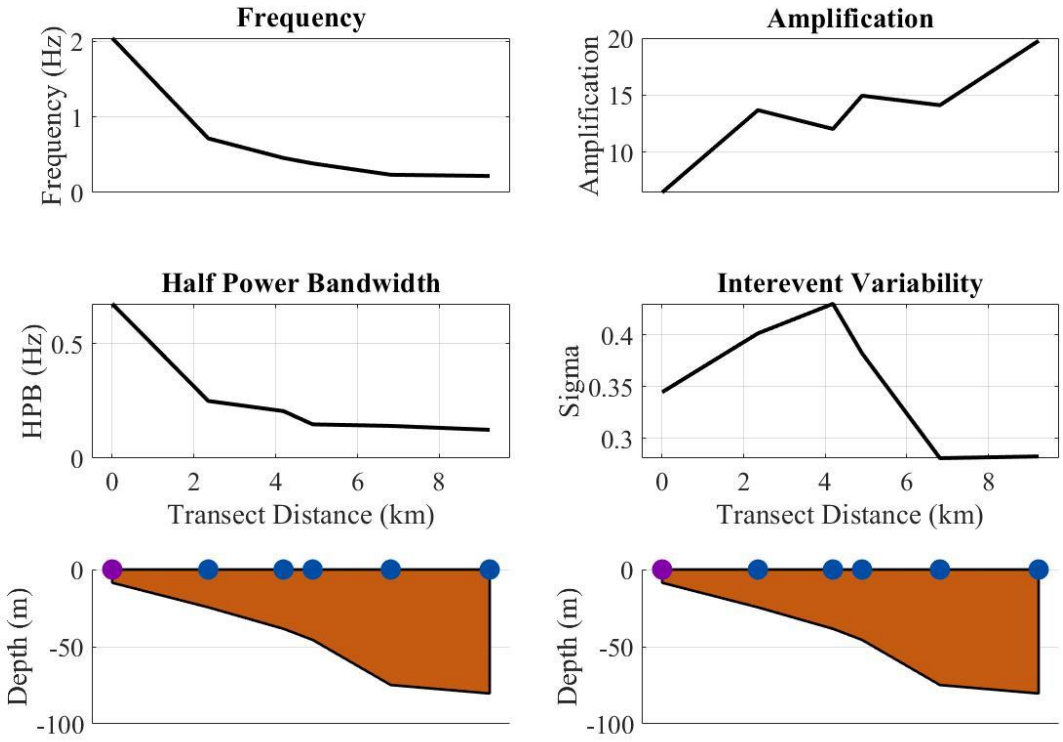

Figure 34. The four peak statistics computed at the fundamental peak of all the stations across the transect.

4.4 Spatial statistics

4.4.1 Number of peaks

Most of the station HVSRs have two significant peaks identified by the peak finding algorithm. The lake zone has a mean number of peaks of 3.08 and a median number of peaks of 3 while the transition has a mean number of peaks of 2.5 and a median of two, thus the mean and median number of peaks in the lake zone are higher than the mean and median number of peaks in the transition zone. The lake zone stations, however, have a wider range in the number of peaks, one to seven, than the transition zone, two to four (Fig. 35).

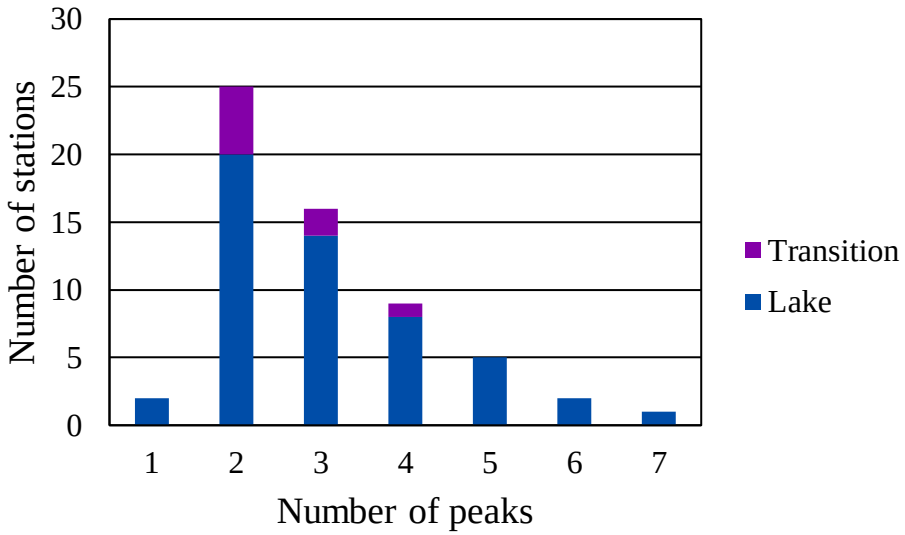

Figure 35. Number of peaks at each station with the zone indicated in blue (lake) and purple (transition). The stations with a higher number of peaks exhibit more resonance than stations with fewer number of peaks

There is a trend in of increasing number of peaks from the basin edge to the middle of the basin but the stations with two to three peaks dominate most of the basin. Additionally, there are pockets of stations within the transition zone and just to the east of it that have more than three peaks, indicating higher resonance in that area than in areas with fewer peaks (Fig. 36).

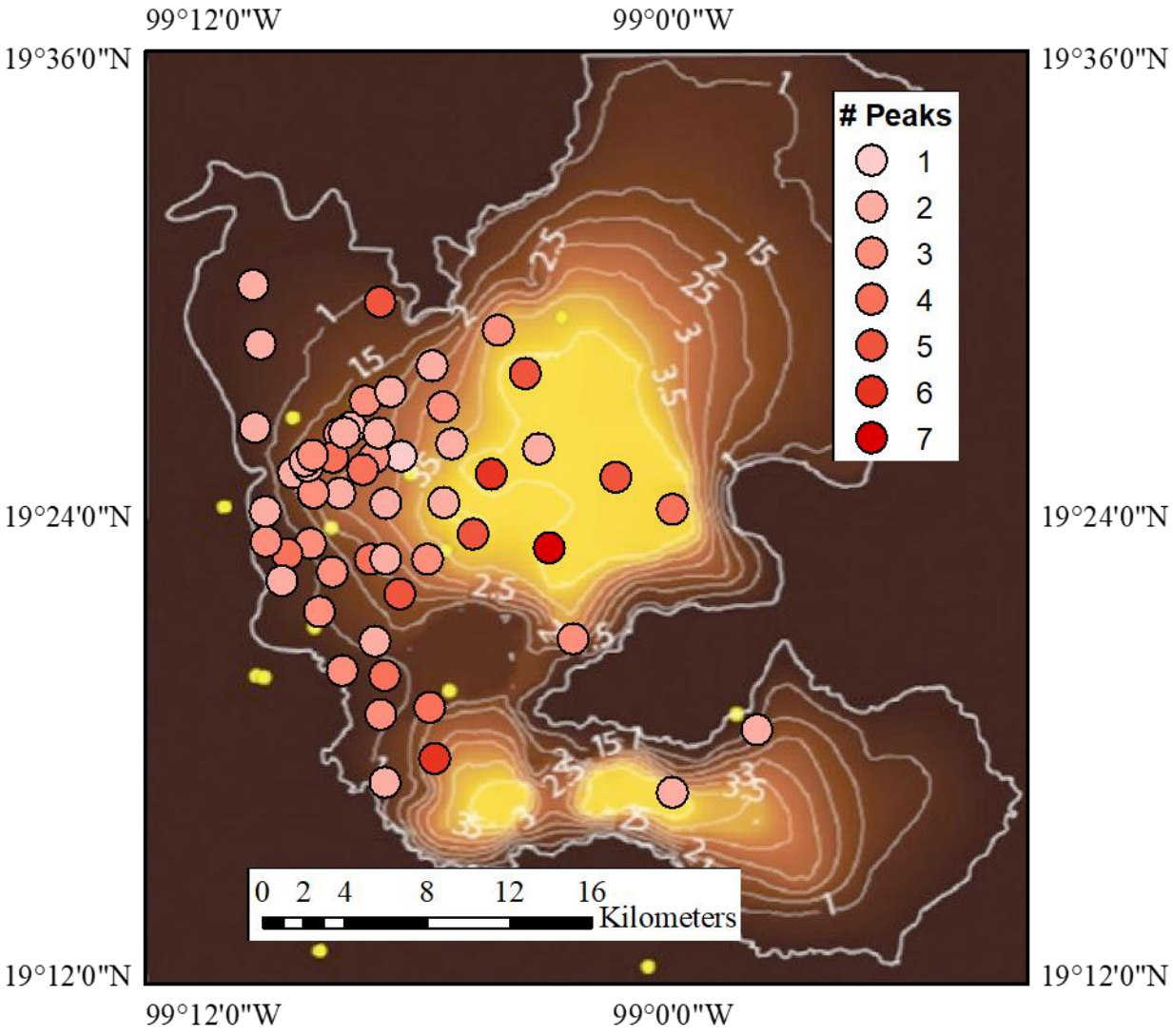

Figure 36. Number of peaks plotted across the basin at each station. A darker shade of red indicates a larger number of peaks in the HVSR. These values are in Table 6 in the appendix.

Spatially, most stations, those with two to three peaks, fall in the transition zone and just to the east of the transition zone. The stations with the greatest number of peaks tend to be in the middle of the basin though some are located elsewhere.

4.3.2 Fundamental peak statistics f_n, a, HPB and σ_i

Stations in the Mexico City basin tend to have decreasing f_n, increasing amplification, decreasing half power bandwidth and no trend in interevent variability moving from the transition zone into the lake zone (Fig. 37; 38; 39). The relationship between f_n and depth (Eq. 2) justifies the discrepancy in f_n between the lake and transition zone: as the depth increases, the fundamental frequency decreases so moving into the basin into deeper clay deposits in the lake zone increases the fundamental frequency. The amplifications in the lake zone stations are, on average, greater than those in the transition zone but the spread of the data is higher (Fig. 38b). Some lake zone station amplifications are lower than all the transition zone station amplifications. A few half power bandwidths in the lake zone are as large as half power bandwidths in the transition zone, though these are on the boundary of the lake and transition zone. The interevent variabilities are close in median with a significantly wider spread in the lake than the transition zone.

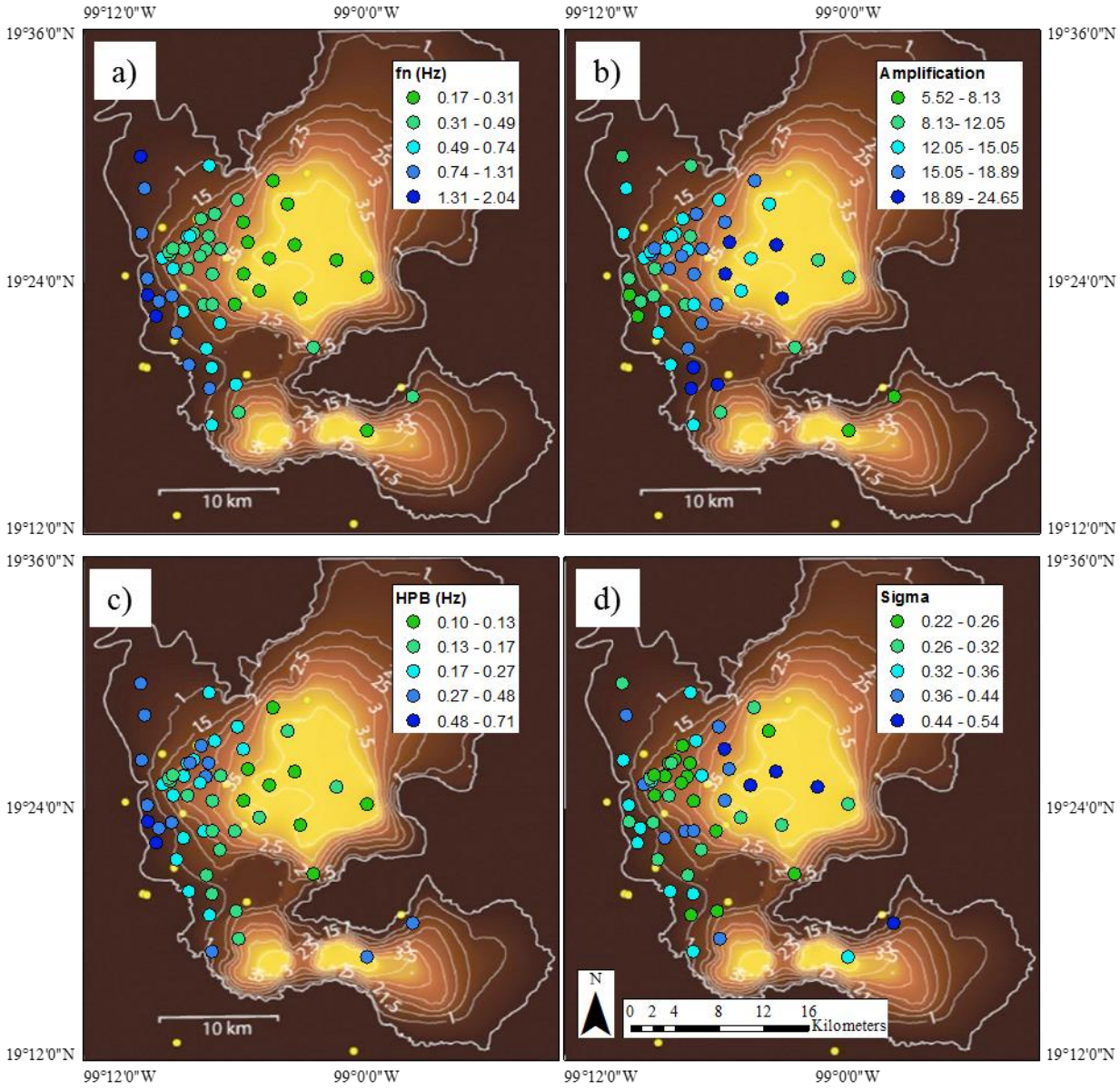

Figure 37. Fundamental period map of Mexico City from Çelebi et al. (2017) overlaid with stations from the transition and lake zones with peak statistics from the fundamental peak: a) fundamental frequency, b) amplification, c) half power bandwidth and d) interevent variability. The white lines indicate lines of equal fundamental period. These values are in Table 7 in the Appendix.

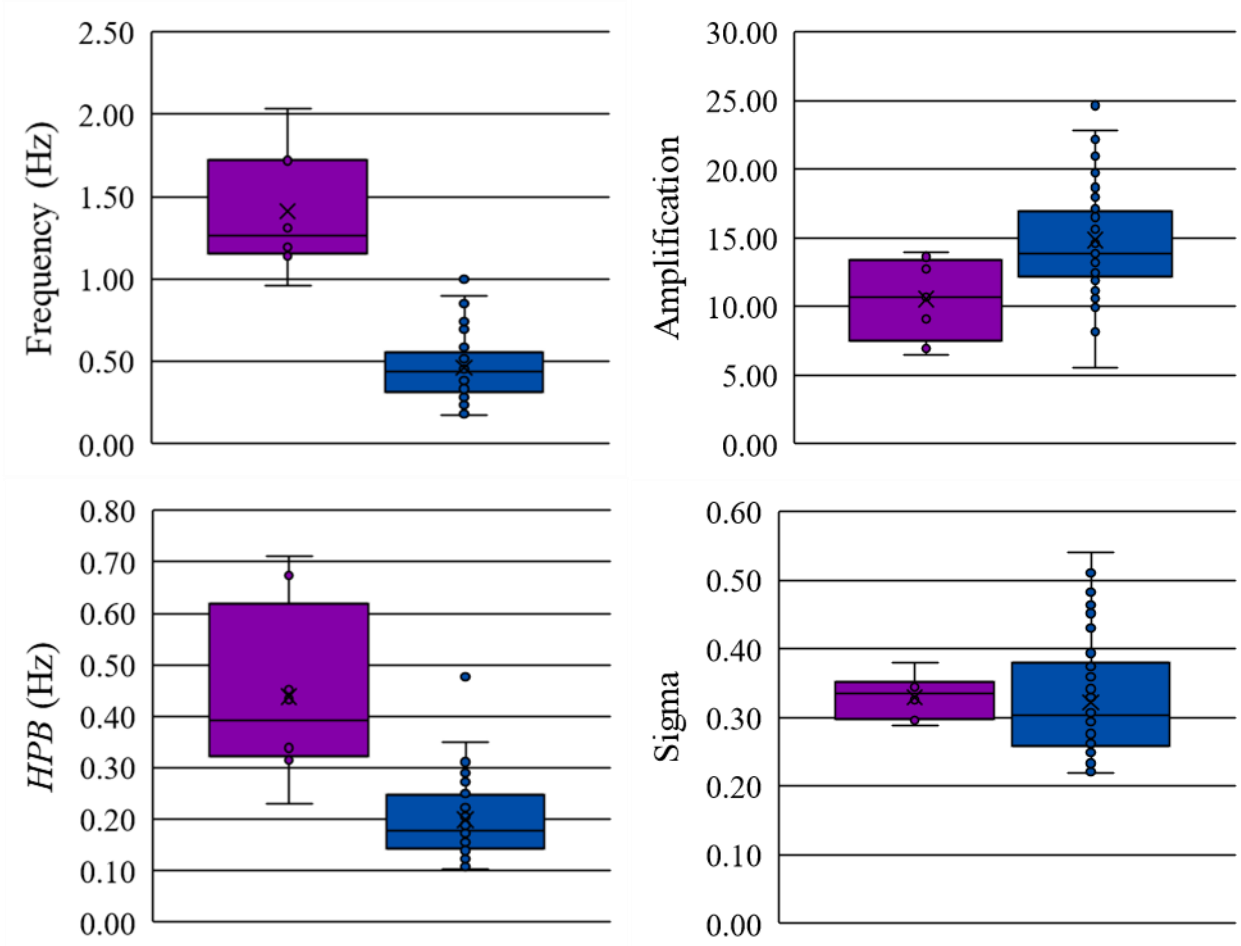

Figure 38. First peak statistics for the HVSR, transition zone is in violet and lake zone is in blue *a)* f_n *b)* amplification *c) HPB d)* σ_i between f_a and f_b.

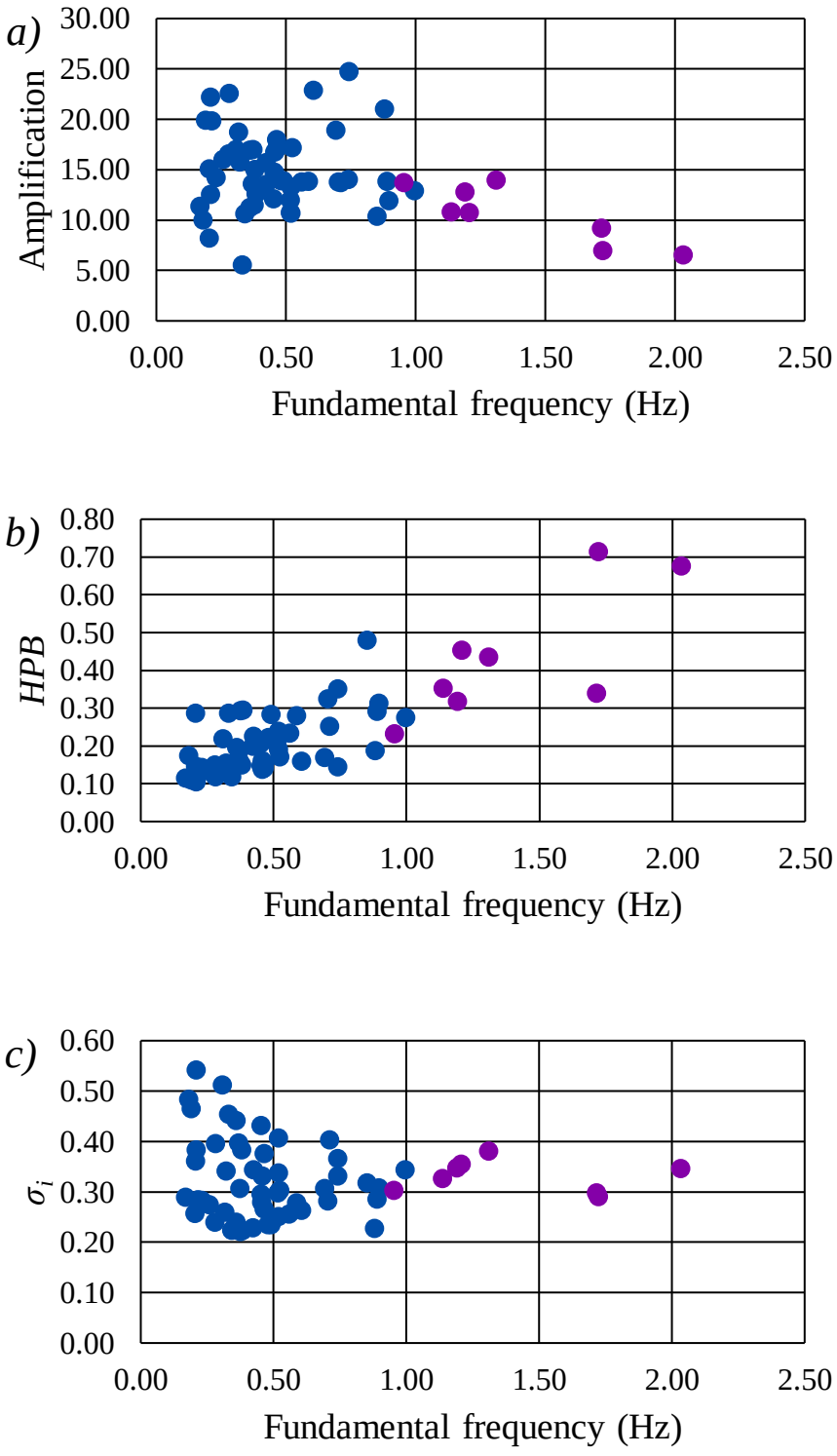

Figure 39. Using f_n as a proxy for the depth, we can image the Mexico City Basin from the edge to the center radially using these plots a) a vs f_n b) HPB vs f_n c) σ_i vs f_n.

5.0 DISCUSSION

5.1 Thompson et al. (2012) statistics

The Thompson et al. (2012) site classification statistics interevent variability and goodness of fit to the SH1D assumptions applied to an inverted HVSR onto a TTF yields four significant results. First, at some station in the Mexico City basin, the HVSR captures higher modes of resonance that are well modelled by the SH1D model. These stations are the LG stations presented in Figure 25 with high *r* values as well as some stations in the LP quadrant which display higher modes. Second, these statistics image pockets in the basin that are geostatistical different from those around them and thus expose stations that significantly vary from the two-layer SH1D soil model of Mexico City used in this study. Third, the Thompson et al. (2012) statistics allow us to quantify how well the HVSR is modeled by the shear wave transfer function. Fourth, the inverted TTFs have much thinner fundamental peaks than any of the HVSRs. Most of the stations only have two peaks identified by the peak finding algorithm and don't display significant higher modes of resonance as we expect from the HVSR and thus the definition of the Thompson et al. (2012) statistics, using four peaks in the TTF, isn't an ideal quantification of the HVSR. The Thompson et al. (2012) statistics do, however, provide a baseline model for a set of statistics to define the HVSR, mainly, one in which statistics are defined only at the fundamental peak.

5.2 Number of peaks in the HVSR

We expect the HVSR to be a single peak due to the canceling out of the Rayleigh wave term in Equation 9 and observe this at many stations within the basin but also identify stations that display higher modes of resonance. Stations such as CE32 (Figs. 26; 42) are in the middle of the

basin and have multiple peaks selected by our peak finding algorithm. This station's horizontal magnitude response (Fig. 42) has significant higher modes of resonance indicating strong shearing, strong enough to show up in the HVSR. Searching for multiple significant peaks using our algorithm provides a systematic way to indicate sites where the HVSR identifies higher modes of resonance and may be modelled by multiple peaks of the SH1D transfer function.

5.3 Shape statistics

The Thompson et al. (2012) statistics describe station HVSRs in the Mexico RACM network that are well modeled by an SH1D transfer function with a two-layer soil model. Many of the stations, however, are not well-modelled both because the fundamental peak is significantly wider than the fundamental peak in the theoretical transfer function and higher resonances that show up in the TTF don't show up in the HVSR. This spurred us to design a different classification scheme using just the fundamental peak of the HVSR. These statistics are f_n, a, HPB and σ_i of the HVSR fundamental peak. We search for trends in these peak statistics and reveal spatial patterns of the HVSR.

5.3.1 Fundamental frequency

The fundamental frequency of the HVSR is a well-established measure of the fundamental frequency of the site, thus its value has a relationship to depth and shear wave velocity (Eq. 2). The HVSRs that we compute in this study display a strong correlation with the geometry of the Mexico City basin, confirming this relationship (Figs. 15; 41). The fundamental frequencies we compute at the RACM stations are therefore good proxies for the depth to the Deep Deposits in the Mexico City basin if we use a proper estimate of shear wave velocity of the Mexico City clay. Using 70 m/s for the shear wave velocity of Mexico City clay as we did for the TTF inversion, the depth to Deep Deposit map (Fig. 40) yields depths of around 100 meters in the middle of the lake

to depths between 8 and 20 meters in the transition zone. These values are deeper than those from Moisés et al. (2016) who derived a depth to Deep Deposit map using 10,000 boreholes across the City. Their values for depth to Deep Deposits in the middle of the lake are around 70 meters (Fig. 41). The discrepancy between our analysis and that of Moisés et al. (2016) is due to the higher shear wave velocities in the FHL and LCL (Figs. 12; 13) than the 70 m/s we used. Increasing the shear wave velocity would decrease the estimate of depth to Deep Deposits and more strongly correlate with the values obtained by Moisés et al. (2016). The depth values derived from applying Equation 2 to the HVSR also match the depth values derived from the inversion of the HVSR onto a TTF using the soil profile in Figure 2.

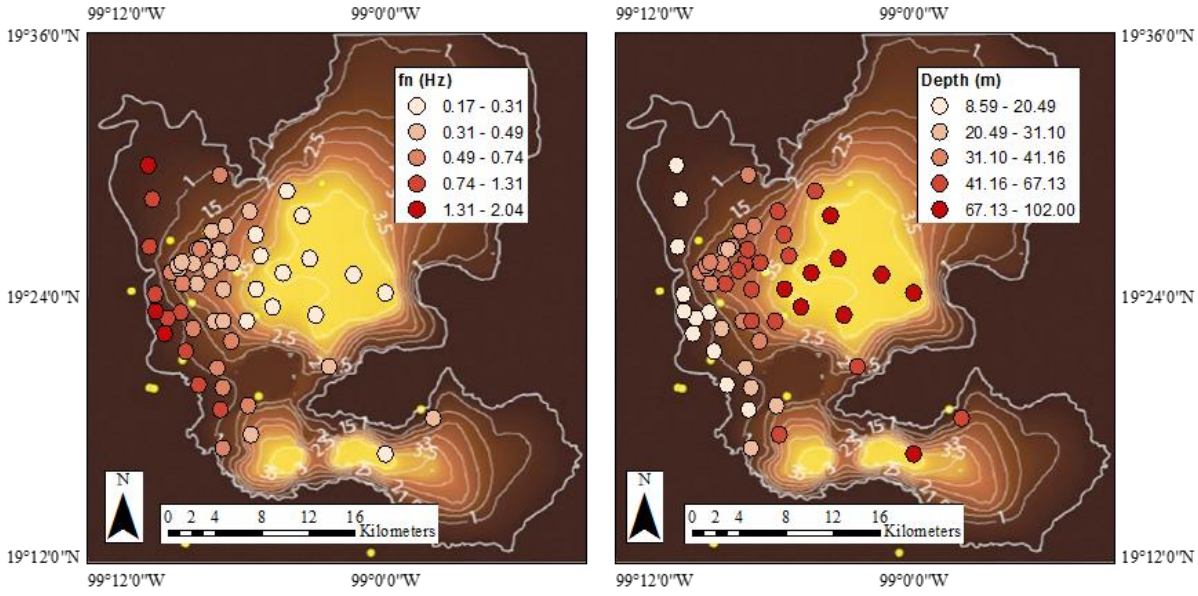

Figure 40. Fundamental frequency from the HVSR and corresponding depth to Deep Deposit map using 70 m/s as a value for Mexico City clay shear wave velocity and Eq. 2 to calculate depth.

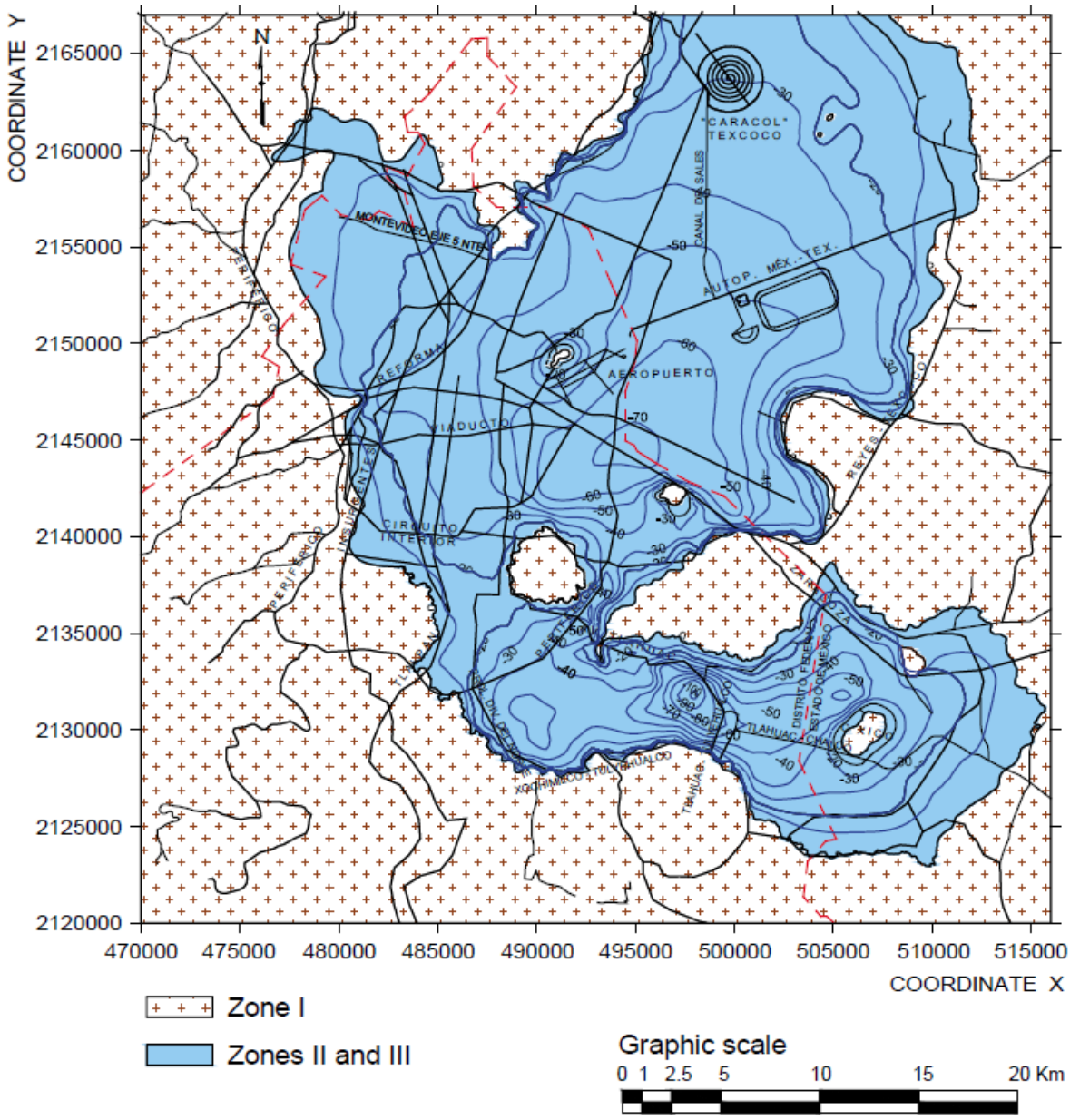

Figure 41. Contour map of depth to deep deposits from Moisés et al. 2016. This map is kriged from 10,000 existing soil profiles within the City.

5.3.2 Amplification

The amplification of the HVSR is less straight forward than the fundamental frequency. We parsed out a small trend of increasing amplification from the transition zone into the lake zone, but all this tells us is that the ratio of the horizontal motion to the vertical motion at the peak

frequency. The vertical motion could be made up of any number of things, multiple reflecting P-waves at a shallower impedance contrast, Rayleigh waves of the same contrast or even non-vertical incidence S waves contaminating the vertical signal. In this way, the HVSR is unable to reliably capture the shear wave amplification in the same way that a more direct measurement, like a borehole transfer function, would. The slight trend that we found, however, indicates significantly stronger shear wave influence at some stations than vertical influence which, if we assume equal vertical influence at sites around the basin, means that the shear wave resonance is stronger at these stations than at lower amplification stations.

In Figure 42, we show the horizontal and vertical magnitude response of CH84, the station with the highest amplification in the study, and CE32, a lake zone station which displays significant resonance in the horizontal component. We also compute the amplitude of each normalized magnitude response at the fundamental frequency identified by the HVSR. The horizontal magnitude response of CH84 at the fundamental peak is 2.33 times greater than the amplitude of the horizontal component of CE32 at the same frequency. The vertical component, however, is just 2 times greater indicating that the change in the difference in the horizontal component has a greater effect in the HVSR amplitude than the vertical component. CH84 has an HVSR amplification 1.26 times greater than CE32, the majority of which is accounted for in the magnitude of the horizontal component. Given vertically propagating shear waves, this indicates that there is more shear at CH84 than at CE32.

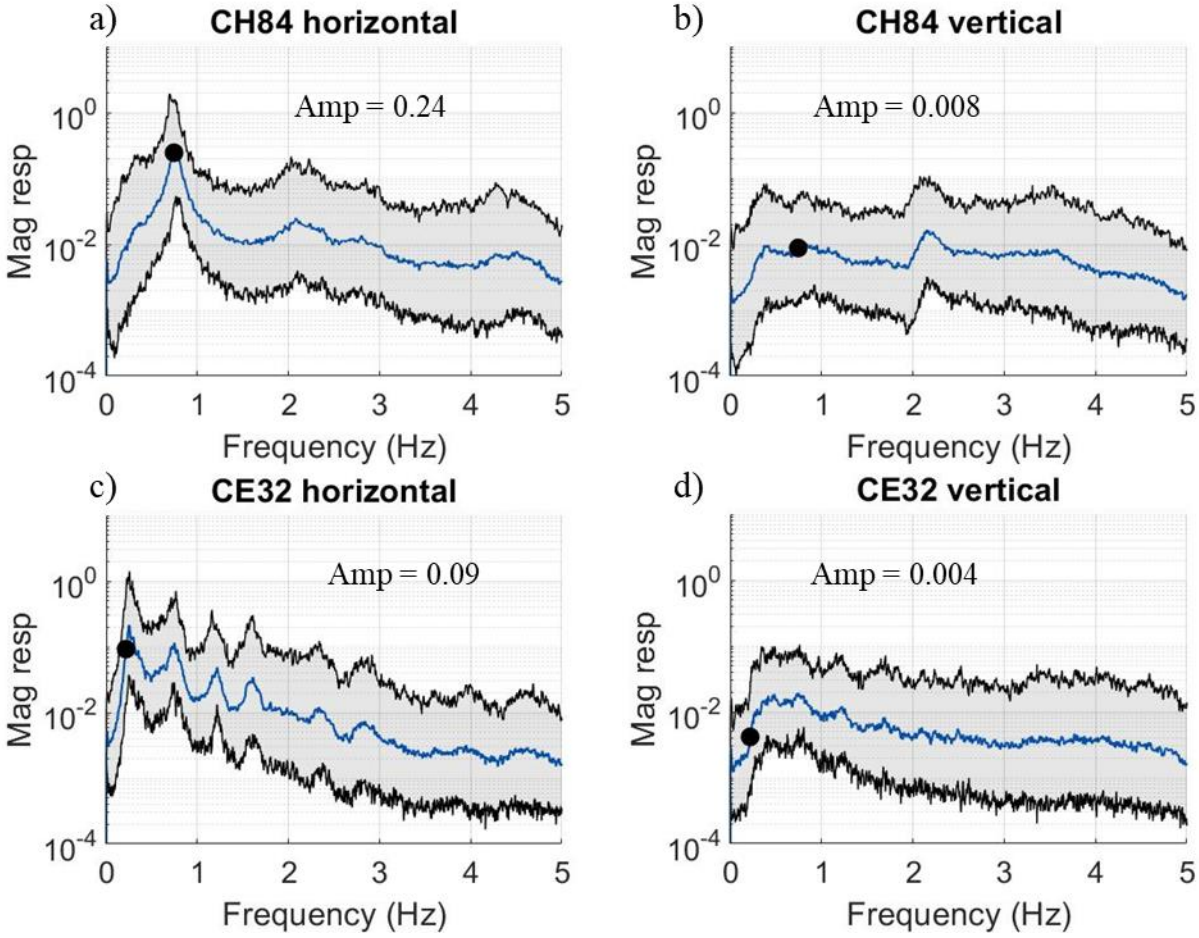

Figure 42. Amplitudes of the normalized magnitude response at a) station CH84 which has the highest HVSR amplification in the dataset and b) CE32 which displays strong resonance in the horizontal component. The amplification values are computed at the fundamental frequency identified by the HVSR. These unfiltered and stacked magnitude responses of all the events at the stations.

In Figure 43, we show the horizontal and vertical magnitude response of CO47, the station with the smallest amplification, and GR27, a transition zone station which displays a typical transition zone response. Performing the same ratio analysis as we did for stations CH84 and CE32, the horizonal component of GR27 is 2.55 times greater than the that of CO47 whereas the vertical component is 0.75 times that of CO47. GR27 has an amplification 2.63 times that of CO47, most of which is accounted for by the horizontal component, but some of which is accounted for by the lower vertical component.

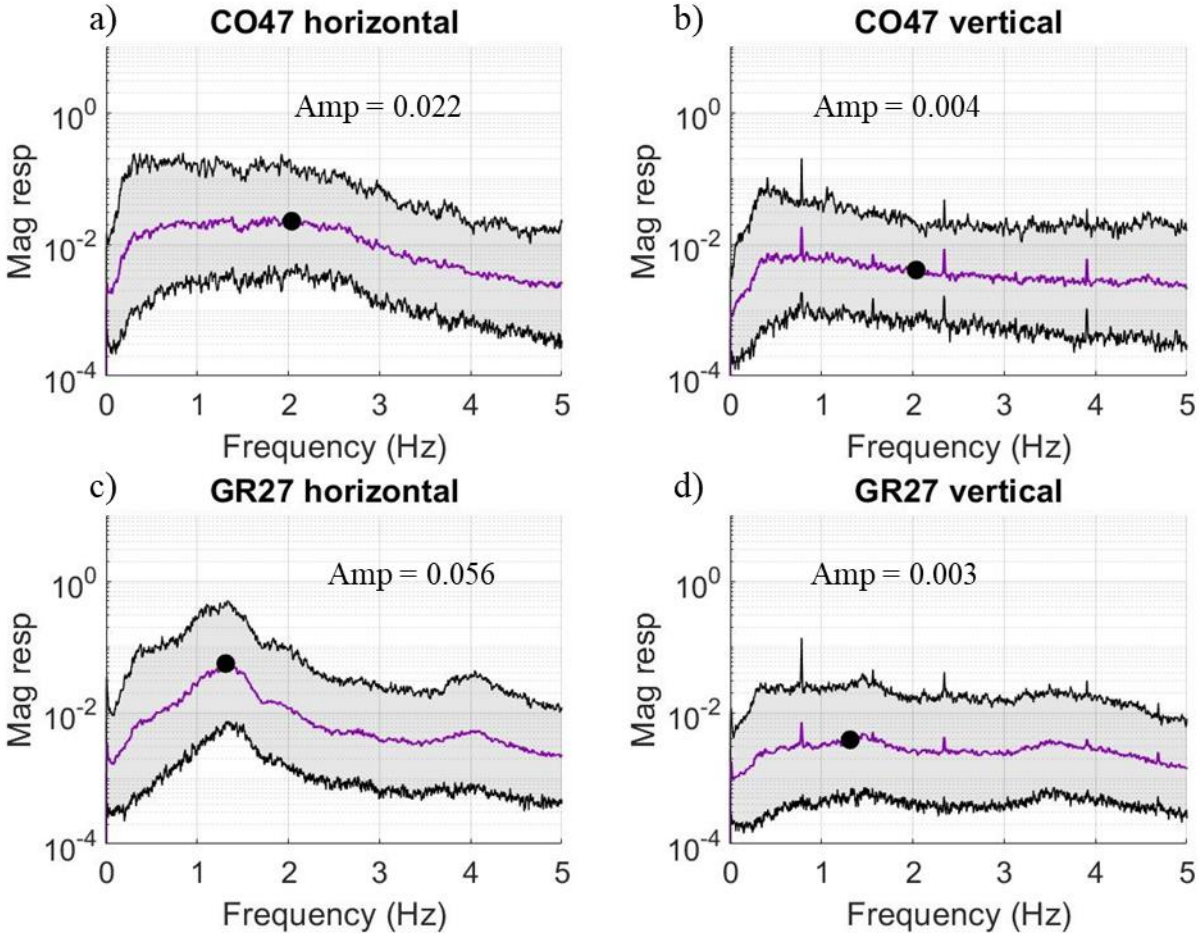

Figure 43. Amplitudes of the normalized magnitude response at two transition stations a) station CO47 which has the smallest HVSR amplification in the dataset and b) GR27 which displays a typical Mexico City basin transition zone HVSR.

In addition to using the magnitude responses to better understand how each component affects the HVSR, it also displays waves other than shear waves influencing the signal. Because P waves travel at higher velocities than S waves, (App. Eq. 3.1; 3.2), multiple reflecting P waves will influence the vertical magnitude response at higher frequencies than the S wave fundamental peak. This is key to Nakamura's derivation of the HVSR (Sec. 1.1.3.3, Eq. 9; 10). The CH84 vertical component (Fig. 42b) has a peak at around 2 Hz, which we identify as multiple reflecting P wave influence. The peak amplification for the HVSR is unreliable for peaks beyond the fundamental peak as it is affected by Rayleigh and P wave influence that manifest themselves in

the vertical component magnitude response. This explains why only some HVSRs exhibit distinct higher mode resonances, the vertical component magnitude response removes their influence from the HVSR as it is designed to do (Eqs. 8; 9).

5.3.3 Half power bandwidth

There is a distinct trend of increasing half power bandwidth with fundamental frequency (Fig 38b). The *HPB* is related to the damping ζ (Eq. 6), by

$$\zeta = \frac{HPB}{2f_n} \tag{18}$$

where f_n is the fundamental frequency (Chopra, 2007). Thus, theoretically, *HPB* varies linearly with f_n with a slope of 2ζ.

$$HPB = 2\zeta f_n \tag{19}$$

If we assume that the Mexico City basin is a uniform half space with a density and shear wave velocity of the overburden of 1.1 g/cm^3 and 70 m/s respectively and a density and shear wave velocity of the basement of 2.7 g/cm^3 and 475 m/s respectively as we did for the inversion of the TTF onto the HVSR, we can use the fundamental frequency of the HVSR to calculate the *HPB* using equation 19 with any ζ value. This scenario is a uniform, SH1D basin where the only varying property is depth to the halfspace. As the depth varies, the fundamental frequency varies (Eq. 2) and thus the halfpower bandwidth varies (Eq. 19). We use a ζ value of 2.9%, the average ζ value of those generated during the inversion. Using this value, this realization of the Mexico City basin half power bandwidth becomes a straight line with respect to the fundamental frequency with a slope two times the damping (Fig. 44)

$$HPB = 0.057 f_n \tag{20}$$

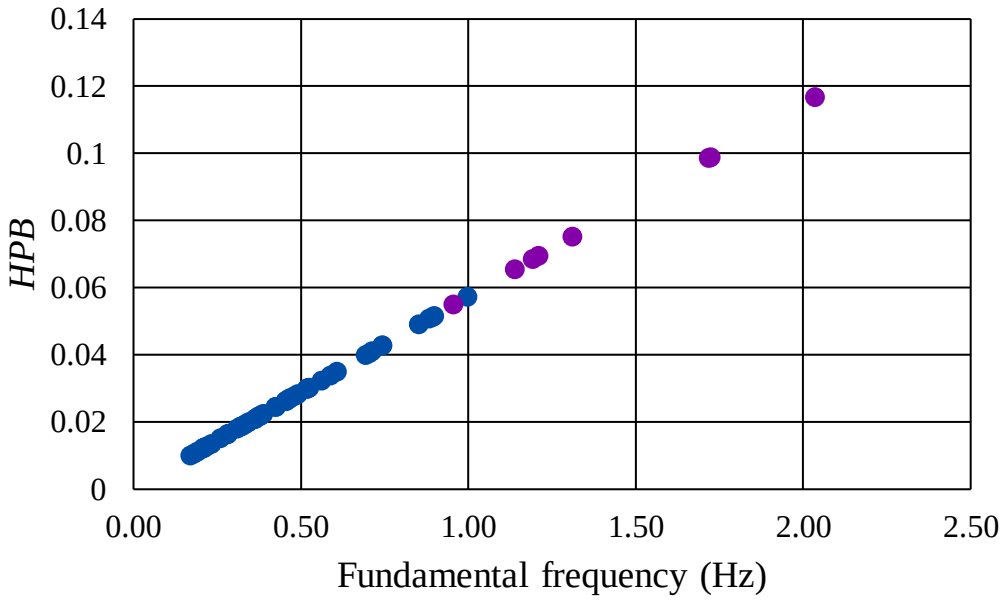

Figure 44. Realization of the Mexico City basin as uniform, SH1D throughout with varying depth and uniform damping using fundamental frequencies obtained from the HVSR and Eq. 20 to compute *HPB*. Lake zone stations are in blue and transition zone stations are in purple.

If we then account for the small perturbations in ζ generated by the inversion, the realization of the

Mexico City Basin becomes:

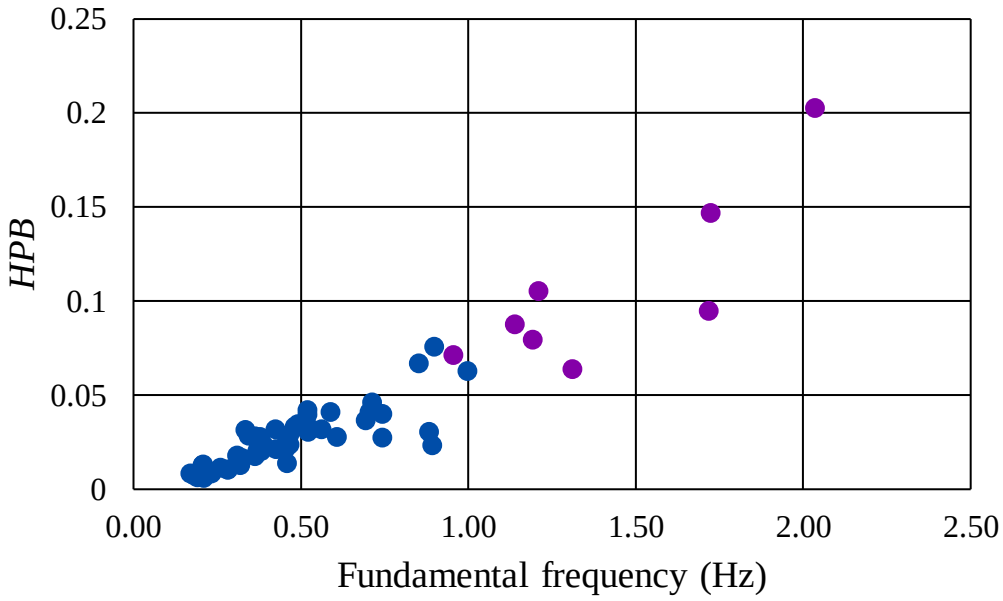

Figure 45. Realization of the Mexico City basin using fundamental frequencies obtained from the HVSR, the damping values obtained from the inversion of the TTF onto the HVSR and Eq. 20 to compute *HPB*.

This realization has a slope the same as that in Figure 44, the noise coming from varying values of ζ. If we create the same figure using the values of half power bandwidth and fundamental frequency of the HVSR, however, we still get a linear trend, but with significantly higher scatter than the second realization (Fig. 46) of Mexico City.

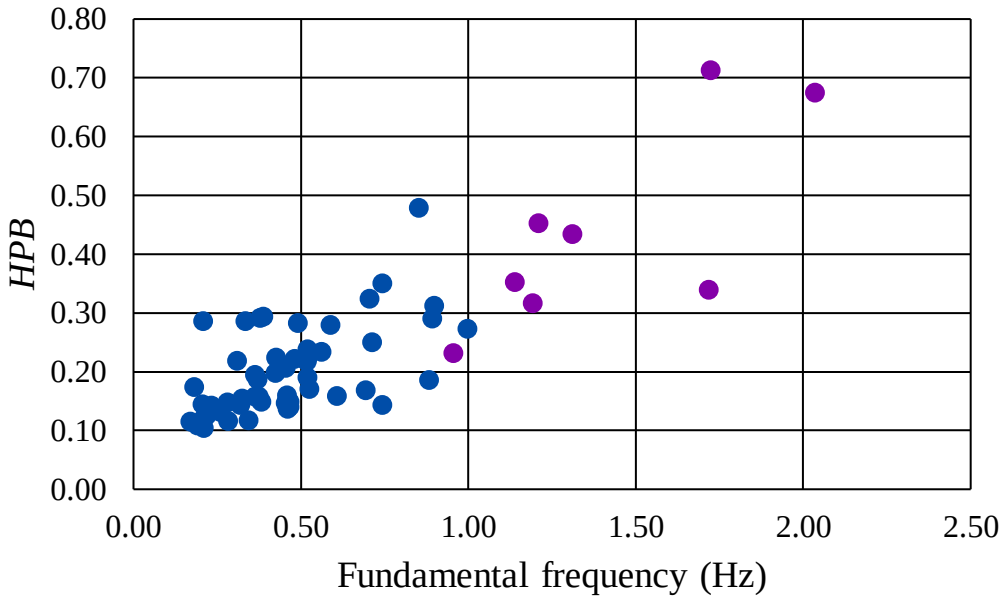

Figure 46. Mexico City basin using fundamental frequencies and *HPB*s obtained from the HVSR

If we plot both realizations (Figs. 44; 45) with the data derived from the HVSR, the slope of the HVSR line is significantly greater than either of the two realizations.

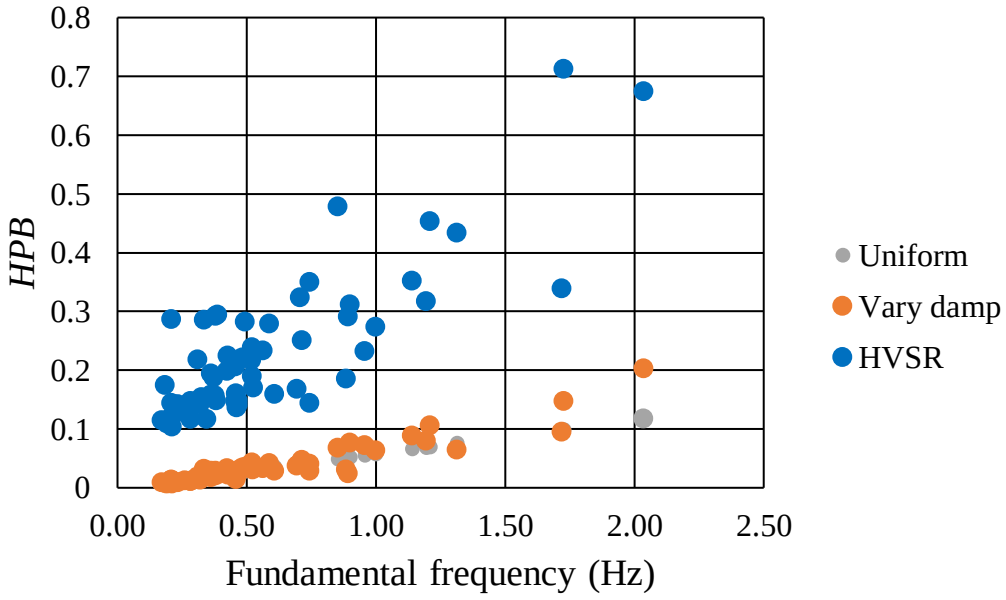

Figure 47. Both realizations and the fundamental frequency and half power bandwidth of the HVSR. Vary damp stands for varying damping.

The linear regression of the HVSR plot yields a slope of 0.35, which, using Eq. 20, translates to a damping value of 17.5%, significantly higher than either of the realizations. The small strain estimations of ζ in the literature are between 2% and 4% in Mexico City at strains below 0.1% (Mayoral et al. 2016). The TTF, inversion estimates these values well with an average of 2.9% and a range between 1.3% and 5% but the HVSR does not. We attribute this discrepancy to wave scattering due to geologic complexity. This interpretation is coupled with the much thinner TTFs derived from the inversion and is guided by the assumption that the HVSR images the fundamental peak of the SH1D TTF. The damping discrepancy could also be a breakdown of Nakamura's assumptions in the HVSR derivation and what we're imaging is a fundamental peak whose shape is manipulated by the processing but results from Thompson et al. (2009) and (2012) yield similar results: a broader fundamental peak in the empirical transfer function than the theoretical transfer function which they also attribute to wave scattering due to geologic complexity. We conclude that the higher slope of the *HPB* vs f_n plot of $HVSR_{avg}$ vs the TTF is an indication of wave scattering due to geologic complexity and that the HVSR captures the linear relationship between *HPB* and f_n in the Mexico City basin.

5.3.4 Interevent variability

The Thompson et al. (2012) statistics identify station HVSRs in the Mexico City basin that can be modeled by a two-layer SH1D system and those that cannot. They also provide a baseline to compare other σ_i measurements, specifically the median σ_i between f_a and f_b, which is the value we calculate in this study for the fundamental peak shape statistics. The Thompson et al. (2012) definition of sigma has a higher σ_i value than the definition provided in this paper at stations in the Mexico City basin 67% of the time (Fig. 48).

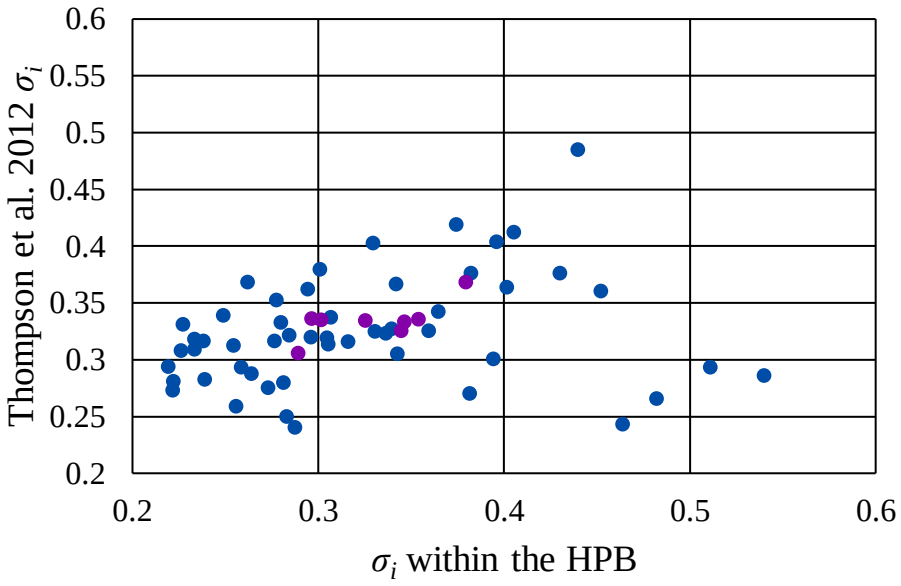

Figure 48. σ_i comparison between the Thompson et al. (2012) definition on the y-axis and our definition between the *HPB* on the x-axis.

This could be due to the influence of the Rayleigh and P wave on the HVSR that complicates the signal at higher frequencies, frequencies that the Thompson et al. (2012) statistics consider. To analyze this, we plot the sigma vector of four stations in the transition zone and four in the lake zone. Especially in the lake zone stations, this sigma vector reaches its minimum around the fundamental frequency, the frequency that the HVSR is designed to image, and then it increases at higher frequencies. This explains the greater percentage of Thompson et al. (2012) σ_i values being greater than *HPB* σ_i values: the median is being picked from a broader range of frequencies, many of which are larger than the σ values around the fundamental peak, especially in the lake zone (Fig. 50). We think, therefore, that our formulation of σ_i is more appropriately applicable to the HVSR than the Thompson et al. (2012) definition.

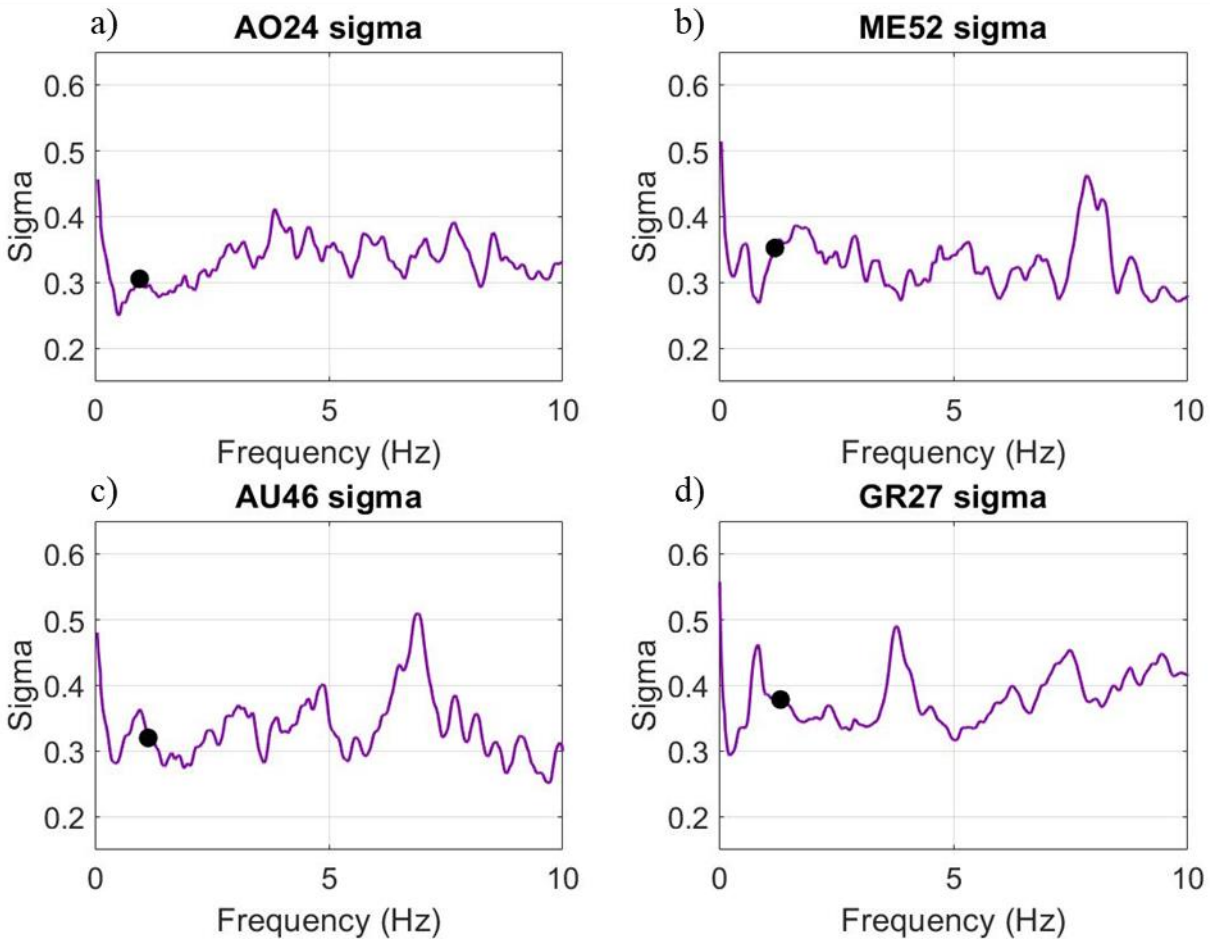

Figure 49. Sigma vector for the four transition zone stations from Figure 27. The black dot indicated the fundamental frequency.

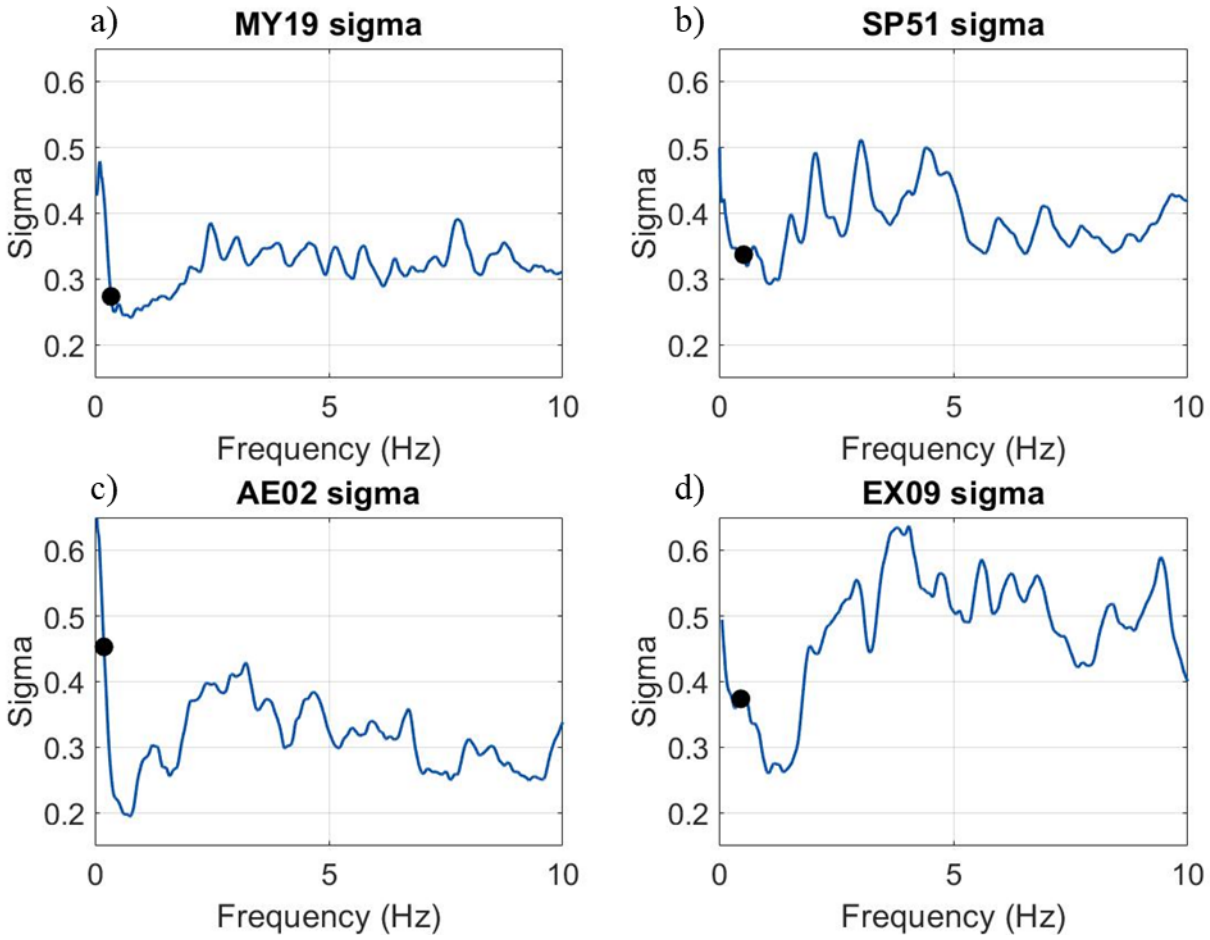

Figure 50. Sigma vector for the four lake zone stations from Figure 28. The black dot indicated the fundamental frequency.

There are several other details of note about these sigma vectors and our formulation of σ_i. First, an advantage of using our definition of σ_i is that we can compute it at multiple locations along the signal, thus getting a more robust view of signal variations at different frequency bands. Second, the high values of sigma at frequencies above the fundamental shear resonance in the lake zone sigma vectors may be indicators of the multiple reflecting P waves or the influence of the Rayleigh wave complicating the signal. Third, often the peaks in the frequency vector match up with peaks in the HVSR (Figs 27; 28; 49; 50). These details are important for a user of the HVSR's awareness.

We expected σ_i values in the transition zone to be higher than those in the lake zone because the sloping halfspace and increase in geologic complexity due to sand lenses would increase wave scattering and thus HVSR from event to event. The transition zone does have higher σ_i than the lake zone in many instances under both formulations of interevent variability though it is slight and has a slightly higher median interevent variability (Fig. 38d). We think, therefore, that the results do not prove that the HVSR interevent variability is higher in the transition zone than the lake zone. This is likely due to the lack of diverse azimuths of the events in the study which all come from the south and west (Fig. 11). With limited azimuthal angles, the full complexity of wave propagation with a sloping halfspace (transition) vs flat halfspace (lake) is not captured. We think that more analyses must be carried out to determine whether σ_i is greater in the transition zone than in the lake zone or not.

6.0 CONCLUSIONS

The HVSR can be a useful tool for assessing site response complexity. Classifying the shape of the HVSR using the number of peaks, peak frequency, amplitude, half power bandwidth and interevent variability between the half power bandwidth of the fundamental peak allows us to get an idea of the higher mode resonance of the HVSR and to quantify the shape of the HVSR peak, interpret its meaning, and determine its relationship to an SH1D TTF fundamental peak. These results provide a cheap, single station tool to give a first estimate on subsurface amplification properties. It gives us a better understating about how the HVSR behaves under different conditions and allows us to use the HVSR as a tool to predict information about an unknown site.

Inverting the HVSR onto a TTF and solving for the damping and depth yields a depth map that correlates well with the known depths of Mexico City and damping values that increase from the lake zone to the transition zone. The depths are a function of our two-layer soil model (Fig. 2) and therefore are slightly greater than the ground-truth estimates provided in Moisés et al. (2016). This is a similar result to our depth to Deep Deposit map derived from f_n and Equation 2 which uses the same shear wave velocity value. The damping values derived using this inversion are consistent with the estimates provided in the literature for Mexico City damping values (Mayoral et al. 2016). Their increase is a function of an increase in width of the fundamental peak from the lake zone to the transition zone. This inversion onto a simple model of Mexico City provides a good estimate of the Mexico City basin shape and damping values and thus shows that the HVSR is a good tool to approximate basic basin properties using the SH1D model given an SH1D environment like Mexico City.

The HVSR can be applied using the Thompson et al. (2012) statistics as a baseline for its approximation of an SH1D transfer function. In this study we inverted for the TTF, giving a TTF

not as robust as one calculated from a known site shear wave velocity profile. An inverted TTF provided a comparison between the HVSR and an idealized realization of the Mexico City basin. Deviations between the HVSR and these TTFs indicate their difference from the 2-layer SH1D model. The HVSR approximated the fundamental peaks of the Mexico City basin, though in all cases was significantly wider than its inverted TTF, a detail we attribute to wave scattering due to geologic complexity. The HVSR also often doesn't display the modelled higher mode resonances at many stations because it is designed to only image the fundamental peak. We think, therefore, that it is not always a proxy for the shear wave transfer function at frequencies higher than the shear wave fundamental frequency unless, in LG cases like stations MY19 and CJ03, the station exhibits significant resonant behavior, behavior that we can identify using our peak finding algorithm.

The number of peaks in the HVSR gives an estimate of the resonance associated with a site. Our peak finding algorithm uses prominence to define a peak as any that has a computable half power bandwidth: the left and right interval min must be less than the amplitude / $\sqrt{2}$ (Sec. 3.4). Most of the stations in Mexico City have two or three peaks, the latter two being small with the fundamental peak always being the most significant (Fig. 36). The stations that have many peaks selected by the algorithm exhibit resonance that we do not expect for the HVSR. These higher modes tend to, however, not capture the full resonance in the horizontal direction because they are diminished by the influence of the Rayleigh and P wave (Eq. 8; 9). The same algorithm can be applied to other empirical transfer functions such as borehole or SSR. With more direct types of measurements of the empirical transfer function like the borehole transfer function using databases like Kik-net, this peak finding algorithm can help identify resonances systematically and automated.

The HVSR is a good tool to measure of the site fundamental frequency and can be used to map the depth to the Deep Deposits in the Mexico City basin (Fig. 40), a map which correlates to a map derived from borehole information (Moisés et al. 2016) (Fig. 41) as well as the depths derived from our TTF inversion (Fig. 23a).

The HVSR amplification has a slight trend from the basin edge to the center of the basin which we attribute to a greater influence of the horizontal component magnitude response compared to the vertical on the HVSR. The horizontal component amplitudes change more significantly than the vertical component amplitudes and thus have a more significant effect on the amplification of the HVSR at the peak fundamental frequency. The vertical component, however, varies throughout its magnitude response and thus changes the amplification of the HVSR (Figs. 42; 43). Given the same horizontal motion, for the amplification of the HVSR to equal the amplification of a borehole transfer function, the value of the vertical component magnitude response at the fundamental frequency would have to equal the value of the horizontal component of the magnitude response at the coupled borehole station.

The *HPB* of the $HVSR_{avg}$ of small strain active source events in Mexico City has a linear relationship with the fundamental site frequency. Given that the HVSR images the fundamental peak of the shear wave transfer function, the slope of the linear regression should give an estimate of the average basin damping. The value we obtained in the linear regression, however yields a damping value higher than expected for Mexico City soil damping, 17.5% instead of the 2% to 4% found in the literature (Mayoral et al. 2016). We attribute this discrepancy to wave scattering due to geologic complexity, an observation reflected both by the slope of the *HPB* vs f_n plot and the wider peaks shown in the inverted TTFs than HVSRs.

The Thompson et al. (2012) definition of interevent variability includes four peaks of the TTF, peaks not designed to be imaged by the HVSR. We observe the effects of this definition in two instances: 1) greater σ_i values using the Thompson et al. (2012) statistics than the *HPB* σ_i formulation and 2) higher σ_i values at frequencies above the fundamental frequency which are included in the Thompson et al. (2012) formulation (Figs. 50; 51). We think that our σ_i value is therefore more applicable to the HVSR than the Thompson et al. (2012) formulation of σ_i. We were unable to parse out any distinct trends in σ_i in the Mexico City basin though this could be a result of the limited azimuths in our database.

We can use the Thompson et al. (2012) statistics to observe how well the HVSR approximates a site's SH1D transfer function and use it as a model to develop more HVSR specific statistics. In this study, we present five statistics 1) the number of significant peaks of the HVSR and 2) the frequency 3) the amplitude, 4) the half power bandwidth and 5) the interevent variability of the fundamental peak. The number of significant peaks identifies stations in which the HVSR displays higher modes of resonance. In Mexico City, the number of significant peaks increases from the transition zone to the lake zone. The latter four statistics use only the fundamental peak, what the HVSR was designed to image, to describe the shape of the HVSR. We conclude that the high slope of the half power bandwidth vs. fundamental frequency plot and the discrepancy between the width of the inverted TTF and the HVSR fundamental peak are indicators of wave scattering due to geologic complexity. For our analysis of the Mexico City Basin, the number of peaks in the HVSR increases, the fundamental frequency decreases, the amplification increases, the half power bandwidth decreases and there is no distinct trend in the interevent variability with increasing depth in the Mexico City Basin from the transition to the lake zone.

ACKNOWLEDGEMENTS

I would like to first and foremost thank Dr. Laurie Baise for her continuing support of this research, insightful comments, attention to detail and weekly meetings. Thank you to Dr. Plumb who often took time out of his day to meet with me discuss my research both technically and philosophically as it integrates science and applied engineering. Thank you to Dr. Lamontagne who has guided me in statistical analysis and optimization as well as simply communicated with me with informal meetings that are small, yet over time, powerful. Thank you to Dr. Pestana, who taught Earthquake Engineering this spring and opened my eyes to an entirely different way of thinking about the site response problem, teaching me time domain analyses and providing a historic and holistic setting for the practice. Thank you to Dr. Jim Kaklamanos who played a major role in editing sections 1.1.3.3, 1.2 and 1.3 as well as several iterations of editing on figure 40 and consultation on the design of the shape statistics. Thank you to my colleagues, Lichen Wang, Parker Aubin, Stephen Lambert, Deniz Ranjpour, Vahid Rashidian, Fatemah K., Illaria Cinelli, Avis Carrero, Mark Zoblacki, Sofia Puerto, Caitlin Barber, Flannery Dolan, Ashkan M., Liz Fletcher, Amanda Parry, Justin Reyes and many others who have helped me with technical problems and have also become my friends. Thank you to the faculty of the CEE department as well as the staff on whom I constantly rely for aid in all things administrative, particularly Laura Sacco and Debra Mcknight. Finally, I thank you to my family and friends who make it all worth it, especially my mother, Heather Cox Richardson, who has inspired me as a researcher and driven me to always strive for excellence both with work, and with life.

REFERENCES

Baise, L. G., Dreger, D.S., Glaser, S.D. (2003a). Site Response at Treasure and Yerba Buena Islands, California. Journal of geotechnical and Geoenvironmental Engineering. Vol. 93, No. 1: 465-479.

Baise, L. G., Dreger, D.S., Glaser, S.D. (2003b). The Effect of The Effect of Shallow San Francisco Bay Sediments on Waveforms Recorded during the M_W 4.6 Bolinas, California, Earthquake. Bulletin of the Seismological Society of America. 10.1061/(ASCE)1090-0241(2003)129:6(415).

Baise, L. G., Kaklamanos, J., Berry, B.M., Thompson, E.M. (2016). Soil Amplification with a strong impedance contrast: Boston Massachusetts. Engineering Geology 202 (2016) 1-13.

Beresnev IA, Wen KL. (1996) Nonlinear soil response—a reality? Bulletin of the Seismological Society of America 1996;86(6):1964–78.

Bonilla, L. F., J. H. Steidl, J. C. Gariel, and R. J. Archuleta (2002). Borehole response studies at the Garner Valley Downhole Array, southern California, 92, 3165–3179. Bulletin of the Seismological Society of America.

Boore, D. M. (2004). Estimating V_s30 (or NEHRP Site Classes) from Shallow Velocity Models (Depths < 30 m). Bulletin of the Seismological Society of America, Vol 94. No. 2, pp. 591-597.

Boore, D. M. (2005). SMSIM-Fortran Programs for Simulating Ground Motion from Earthquakes: Version 2.3-A of OFR 96-80-A. United States Department of the Interior. U. S Geological Survey.

Borcherdt, R.D., (1970). Effects of Local Geology on Ground Motion Near San Francisco Bay. Bulletin of the Seismological Society of America. Vol. 60, No. 1, pp. 29-61.

Butterworth, S., (1930). On the theory of filter amplifiers. Exp. Wirel. Wirel. Eng. 7, 536–541.

Campillo M., Gariel, J. C., Aki, K. Sanchez-Sesma, F.J. (1989). Destructive Strong Ground Motion in Mexico City: Source, Path, and Site Effects During Great 1985 Michoacan Earthquake Bulletin of the Seismological Society of America 79(6): 1718-1735.

Carlton, B.D., Pestana, J.M., Bray, J.D. (2005). Selection of Target Ground Motion Parameters for Nonlinear Site Response Analyses. GeoEngineering Report No UCB/GE/2015-01. June 2015.

Castellaro, S., Mulargia, F., Rossi, P. L. (2008) V_s30 as a proxy for seismic amplification?. Seismological Research Letters 79(4):540-543.

Castro Cruz, D. A., Regnier, J., Etienne, B., Courboulex, F., (2018). Seismic Non-Linear Behavior of Soil Inferred by Analysis of Borehole Data. Conference Paper at 16th European Conference on Earthquake Engineering.

Çelebi M, Sahakian V, Melgar D, Quintanar L. (2017). The 19 September 2017 M 7.1 Puebla-Morelos Earthquake: Spectral Ratios Confirm Mexico City Zoning. Bulletin of the Seismological Society of America. Vol. 20, No. 20.

Centro de instumentación y registro sísmico a.c. Accelerographic Network of Mexico City. Web accessed 3/27/2019. http://www.cires.mx/racm_es.php.

Centro de instrumentación y registro sismic, a. c. cires.org.mx. Accessed October 2017 and September 2018 to request data.

Chopra, A.K. (2007). Dynamics of Structures: Theory and Application to Earthquake Engineering. Pearson Prentice Hall, Upper Saddle River, New Jersey.

Ebel, J.E., (2006) The Cape Ann, Massachusetts Earthquake of 1755: A 250th Anniversary Perspective. Seismological Research Letters, Vol. 77, No. 1: 74-86.

Field, E.H., Jacob, K.H., (1995). A comparison of Various Site-Response Estimation Techniques, Including Three that are not Reference-Site Dependent. Bulletin of the Seismological Society of America. Vol. 85, No. 4: 1127-1143.

Haskell N. A. (1953) The dispersion of surface waves on multilayered media. Bulletin of the Seismological Society of America; 72:17–34.

Haskell, N. A. (1960). Crustal Reflection of Plane SH Waves. Geophysical Research 65(12): 4147-4150.

Kaklamanos, J., Bradley, B.A., Thompson, E. M., Baise, L. G. (2013). Critical Parameters Affecting Bias and Variability in Site-Response Analyses Using Kik-net Downhole Array Data. Bulletin of the Seismological Society of America. Vol. 103, No. 3: 1733-1749.

Kaklamanos, J., Baise, L.G., Thompson, E.M., Dorfmann, L. (2015). Comparison of 1D linear, equivalent-linear, and nonlinear site response models at six KiK-net validation sites. Soil Dynamics and Earthquake Engineering 69, 207-219.

Kaklamanos, J., Bradley, B.A. (2018a). Challenges in Predicting Seismic Site Response with 1D Analyses: Conclusions from 114 KiK-net Vertical Seismometer Arrays. Bulletin of the Seismological Society of America, Vol. 20, No. 20.

Kaklamanos, J., and B. A. Bradley (2018b). Insights from KiK-net data: What input parameters should be addressed to improve site response predictions? *Geotechnical Earthquake Engineering and Soil Dynamics V: Seismic Hazard Analysis, Earthquake Ground Motions,*

and Regional-Scale Assessment, 10–13 June 2018, Austin, Texas, American Society of Civil Engineers (ASCE) Geotechnical Special Publication No. 291, S. J. Brandenberg and M. T. Manzari (eds.), pp. 454–464.

Kramer, S.L. (1996). Geotechnical Earthquake Engineering, Prentice Hall, Upper Saddle River, N.J.

Lermo, J., and J. F. Chávez-García (1993). Site effect evaluation using spectral ratios with only one station, Bull. Seismol. Soc. Am. 83, 1574–1594.

Lermo J, Chávez-Garcia F.J. (1994a) Site effect evaluation at Mexico City: dominant period and relative amplification from strong motion and microtremor records. Soil Dynamics and Earthquake Engineering. 13(1994): 413-423.

Lermo, J., and J. F. Chávez-García (1994b). Are microtremors useful in site response evaluation? Bull. Seismol. Soc. Am. 84, no. 5, 1350–1364.

MathWorks, (2019). *Signal Processing Toolbox: User's Guide (R2019a)*. Retrieved July 19, 2019 from https://www.mathworks.com/help/signal/ref/findpeaks.html

Mayoral, J.M., Castañon, E., Alcantara, L., Tepalcapa, S. (2016). Seismic Response Characterization of High Plasticity Clays. Soil Dynamics and Earthquake Engineering,84 (2016) 174-189.

Mayoral, J.M., Castañon, E., Sarmiento, N. (2015). Seismic Response of High Plasticity Clays During Extreme Events. Soil Dynamics and Earthquake Engineering, 77 (2015) 203-207.

Mayoral, J.M., Hutchinson, T.C., Franke, K.W. (2017) Geotechnical Engineering Reconnaissance of the 19 September 2017 M_W 7.1 Puebla-Mexico City Earthquake: Version 2.0. Geotechnical Extreme Events Reconnaissance Team.

Mayoral, J.M., Romo, M.P., Osorio, L. (2008). Seismic Parameters Characterization at Texcoco Lake, Mexico. Soil Dynamics and Earthquake Engineering, 28 (2008) 507-521.

The Modified Mercalli Intensity Scale, USGS Earthquake Hazards Program Webpage, Accessed 3/26/2016. https://earthquake.usgs.gov/learn/topics/mercalli.php

Moisés, J.C, Gabriel, A.G, Edgar, M.S. (2016) Geotechnical Zoning of Mexico Valley Subsoil. Ingeniería Investigación y Tecnología, volumen XVII (número 3), julio-septiembre 2016: 297-308.

Mooser, F., 1987. Antecedentes geológicos. *In:* Manual de Diseño Geotécnico, E. Tamez, E. Santoyo, F. Mooser and C. Gutiérrez, eds. (COVITUR, México, vol. 1).

Nakamura, Y. (1989) A Method for Dynamic Characteristics Estimation of Subsurface using Microtremor on the Ground Surface. Railway Technical Research Institute 30(1): 25-33.

Nakamura, Y. (2019). What is the Nakamura method? Seismological Research Letters, early addition. Vol XX, No. XX -2019.

Nogoshi, M., Igarashi, T. (1970b) On the amplitude characteristics of the microtremor-Part 1, *Zisin* **23**, 281-303 (in Japanese with English abstract)

Nogoshi, M., Igarashi, T. (1971) On the amplitude characteristics of the microtremor-Part 2, *Zisin* **24**, 26-40 (in Japanese with English abstract)

Parolai, S., Bormann, P., Milkereit, C., (2002). New Relationships between *Vs* , Thickness of Sediments, and Resonance Frequency Calculated by the H/V Ratio of Seismic Noise for the Cologne Area (Germany). Bulletin of the Seismological Society of America, Vol. 92, No. 6, pp. 2521–2527, August 2002.

Pratt, T.L., Brocher, T.M. (2006). Site Response and Attenuation in the Puget Lowland, Washington State. Bulletin of the Seismological Society of America, Vol. 96, No. 2, pp. 536–552.

Pratt, T.L. (2018b). Characterizing and Imaging Sedimentary Strata Using Depth-Converted Spectral Ratios: An Example from the Atlantic Coastal Plain of the Eastern United States. Bulletin of the Seismological Society of America, Vol. 108, No. 5A, pp. 2801–2815, October 2018.

Rathje, E. M., Kottke, A. R., Trent, W. L. (2010). Influence of Input Motion and Site Property Variabilities on Seismic Site Response Analysis. Journal of Geotechnical and Geoenvironmental Engineering, 136(4).

Rodriguez-Marek, A., Montalva, G.A., Cotton, F., and Bonilla, F. (2011). Analysis of single-station standard deviation using the KiK-net data. Bull. Seism. Soc. Am. 101 (3), 1242-1258.

Romo, M.P., Jaime, A., Reséndiz, D (1988). The Mexico City Earthquake of September 19, 1985-General Soil Conditions and Clay properties in the Valley of Mexico. Earthquake Spectra, Vol 4, No. 4, 731-752.

Sanchez, R.J. (1989) Geology and tectonics of the basin of Mexico and their relationship with the damage caused by the earthquakes of September 1985. International Journal of Mining and Engineering, 1989, 7, 17-28.

Sato, H., and M. C. Fehler (1998). Seismic Wave Propagation and Scattering in the Heterogeneous Earth, Springer-Verlag, New York.

Schilling, R.J., Harris, S.L. (2016). Introduction to Digital Signal Processing using MATLAB. Cengage Learning, Boston, MA.

SESAME (2004a). Guidelines for the implementation of the H/V spectral ratio technique on ambient vibrations. European Commission - Research General Directorate.

SESAME (2004b). Site Effects Assessment Using Ambient Excitations. European Commission - Research General Directorate. Project No. EVG1-CT-2000-00026 SESAME.

Shearer PM, Orcutt JA. (1987) Surface and near-surface effects on seismic waves—theory and borehole seismometer results. Bulletin of the Seismological Society of America 1987;77(4):1168–96.

Sheriff, R.E., Geldart, L.P. (1995). Exploration Seismology, Second Edition. Cambridge University Press.

Steidl JH, Tumarkin AG, Archuleta RJ. (1996) What is a reference site? Bulletin of the Seismological Society of America 1996;86(6):1733–48.

Stephenson, B. Lomnitz, C. (2005). Shear-wave velocity profile at the Texcoco strong-motion array site, Valley of Mexico. Geofisca Internacional 44(1): 3-10.

Storn, R and Price, K. (1997) Differential Evolution - a Simple and Efficient Heuristic for Global Optimization over Continuous Spaces, Journal of Global Optimization, 1997, 11, 341 - 359.

Thomson WT. (1950). Transmission of elastic waves through a stratified solid. Journal of Applied Physics: 21:89–93.

Thompson EM, Baise LG, Kayen RE, Guzina BB. (2009) Impediments to Predicting Site Response: Seismic Property Estimation and Modeling Simplifications. Bulletin of the Seismological Society of America. Vol. 99, No. 5: 2927-2949.

Thompson EM, Baise LG, Tanaka K, Kayen RE. (2012) A taxonomy of site response complexity. Soil Dynamics and Earthquake Engineering. 41(2012): 32-43.

Wormington, M., Panaccione, C., Matney, K. M., Bowen, D. K., - Characterization of structures from X-ray scattering data using genetic algorithms, Phil. Trans. R. Soc. Lond. A, 1999, 357, 2827-2848

Yilar, E., Baise, L.G., Ebel, J.E. (2017) Using H/V measurements to determine depth to bedrock and Vs30 in Boston, Massachusetts. Engineering Geology 217, 12-22.[2]

Zalachoris, G., and Rathje E.M. (2015). Evaluation of one-dimensional site response techniques using borehole arrays, J. Geotech. Geoenviron. Eng., 10.1061/(ASCE)GT.1943-5606.0001366, 04015053.

APPENDIX

1. Fourier transform

An infinite sum of sinusoids makes up every signal. We model these summed sinusoids using the convolution operator

$$y(k) = \sum_{i=0}^{k} h(i)x(k-i), \;\; k \geq 0 \tag{1.1}$$

where *y(k)* is the response of system *x(k)* to impulse *h(i)*.

The Fourier transform takes a signal in the time domain and represents it as its frequency components. Convolution in the time domain is equivalent to multiplication in the frequency domain. This transform is analogous to taking a smoothie and decomposing it into its ingredients and its output is called the *Fourier response spectra*.

$$X_a(f) = \int_{-\infty}^{\infty} x_a(t) \exp(-j2\pi ft)\, dt \tag{1.2}$$

The *frequency response* of a system is the Fourier response spectra of the output of the system divided by the Fourier response spectra of the input of a system. This is analogous to the site transfer function (Eq. 5).

$$H_a(f) = \frac{Y_a(f)}{X_a(f)} \tag{1.3}$$

where $Y_a(f)$ is the output of the system and $X_a(f)$ is the input of the system. In our case, this is the free surface ground motion and the input ground motion respectively.

The Fourier transform yields a solution that is made of two components, the *phase response*, which describes the phase of each sinusoid

$$\varphi_a(f) = < H_a(f) \tag{1.4}$$

where < is the angle operator (the angle between the complex and real parts of the Fourier transform on the complex plane), and the *magnitude response* which describes the magnitude of each sinusoid

$$A_a(f) = |H_a(f)| \tag{1.5}$$

We use the magnitude response in this analysis because we are interested in the magnitude of each frequency to convert to amplification of waves.

We compute the Fourier response spectra numerically using the Fast Fourier Transform (FFT) function instead of the Discrete Fourier Transform (DFT) because it is computationally more efficient.

2. Single Degree of Freedom Systems

A single degree of freedom system (SDOF) is a model of a concentrated mass on a frame. The frame is only allowed to move in one horizontal direction, vibrating back and forth in that direction when subjected to a force or displacement. The amount and frequency of the vibration is controlled by the mass, the stiffness and the damping of the frame. A SDOF system is described by the acceleration, velocity and displacement using the equation of motion:

$$p(t) = m\ddot{u} + k\dot{u} + cu \tag{2.1}$$

where $\ddot{u}$ = acceleration, $\dot{u}$ = velocity, u = displacement, m = mass, k = stiffness and c = damping. To solve for the motion of a linear SDOF system of motion, we set *p(t)* equal to 0 and assume that the initial displacement, velocity and acceleration are also equal to zero. The circular frequency of the system is

$$\omega_n = \sqrt{\frac{k}{m}} \tag{2.2}$$

where k is the stiffness, the force over the length of the member, and m is the mass. K can also be derived by

$$k = m\omega_n{}^2 \tag{2.3}$$

The period of the vibration represents the length of the sinusoid from peak to peak or trough and is given by the relationship with the circular frequency

$$T_n = \frac{2\pi}{\omega_n} \tag{2.4}$$

The natural frequency of the vibration is the number of cycles that occurs every second and is the inverse of the period

$$f_n = \frac{1}{T_n} \tag{2.5}$$

A structure subjected to an initial displacement *u(0)* and released to freely vibrate is given by the equation

$$u(t) = u(0)e^{-\zeta\omega_n t}cos(\omega_d t) \tag{2.6}$$

where ζ is the viscous damping ratio

$$\zeta = \frac{c}{c_r} \tag{2.7}$$

And c is the measure of the amount of energy loss each vibration cycle and c_r is the critical damping

$$c_r = \frac{2k}{\omega_n} \tag{2.8}$$

The damping ratio determines the rate at which the vibrating SDOF system returns to a steady state. A damping ratio greater that 1 is called overdamped. An overdamped system will not vibrate

after being subjected to an initial displacement. A damping ratio of 1 is called critically damped. A critically damped system will return to a steady state the fastest. A damping ratio of less than 1 is called underdamped. An underdamped system will vibrate around the midpoint dissipating energy every cycle (Chopra, 2007).

2.1 Structure or column response to a vibration

In earthquake engineering, we evaluate the response of an SDOF system to a vibration. For example, seismic waves propagating through the bedrock come in to contact with the overburden in a basin and cause it to vibrate. In this instance, the seismic waves are the "forcing function" and they excite the overburden depending on the relationship between the frequency of the seismic waves and the fundamental frequency of the overburden. The closer the fundamental frequency is of the overburden to the frequency of the forcing function, the greater the ratio of the maximum amplification of the overburden to the initial displacement imposed on it by the forcing function. This is fundamental to our understanding of site amplification

$$\frac{u_0}{(u_{st})_0} = \frac{1}{\sqrt{\left[1-\left(\omega/\omega_n\right)^2\right]^2+\left[2\zeta\left(\omega/\omega_n\right)\right]^2}} \tag{2.9}$$

u_0 is the steady state amplitude and $(u_{st})_0$ is the maximum value of the static deformation and their ratio is R_d or the amplification factor. As the ratio of the excitation frequency to that of the fundamental frequency approaches one, the overburden amplifies. The smaller the damping ratio, the greater the amplification factor (Fig. 2.1).

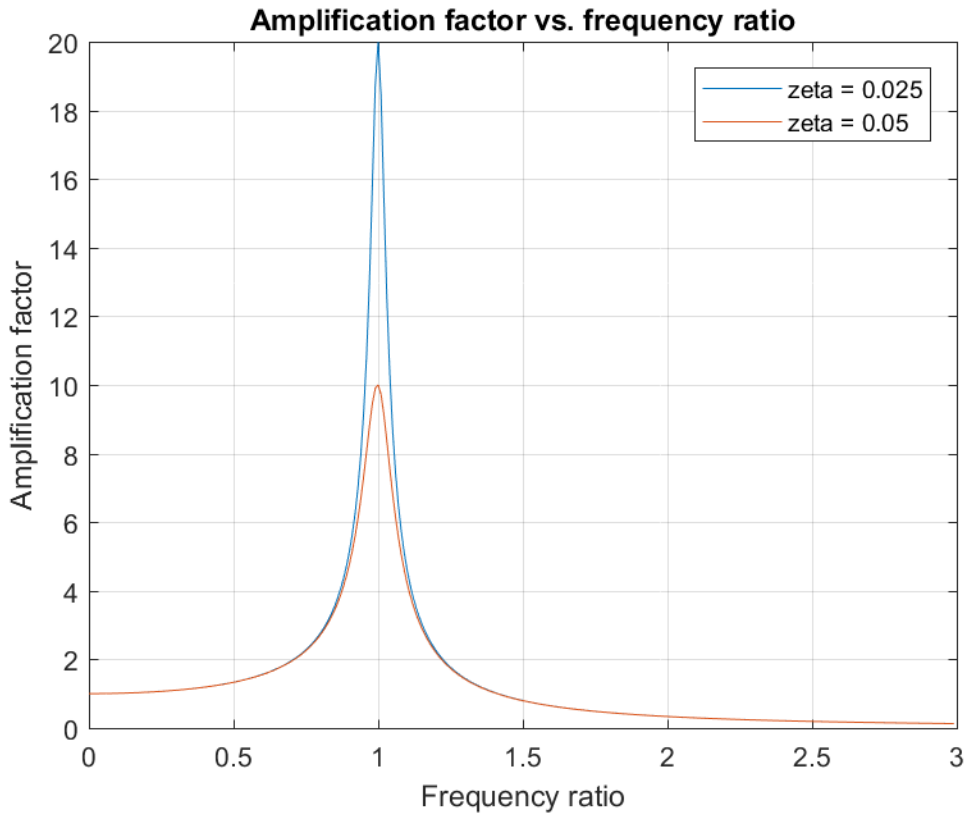

Figure 2.1 Amplification factor vs frequency ratio with two different damping ratio values.

The physical properties we've described all relate to how a material will vibrate. We can take these vibrations and process them using the frequency analysis techniques in appendix section 1 to derive information. We can also invert the frequency domain analysis to estimate sinusoidal properties and ultimately material properties as we have attempted in this thesis for damping.

2.2 Response to a forcing function using Crank-Nicholson approximation

The basin amplification model is seismic waves propagating through the basement layers and exciting a soil column. The propagating waves are known as the "forcing function" and we solve for the response of the soil. In this study, the ground response is analyzed in the frequency domain using spectral ratios. This could be expanded to test the response in the time domain using

the Crank-Nicholson approximation and compared to the frequency domain filtered solution. The Crank-Nicholson approximation is the solution to a SDOF system response to a forcing function *p(t)/m* which is an acceleration time history:

$$v_{t+\Delta t} = \frac{1}{a_1}\left[a_2 v_t + a_3 u_t + \Delta t\left[\alpha\left(\frac{f}{m}\right)_{t+\Delta t} + (1-\alpha)\left(\frac{f}{m}\right)_t\right]\right] \tag{2.10}$$

$$u_{t+\Delta t} = u_t + \Delta t[\alpha v_{t+\Delta t} + (1-\alpha)v_t] \tag{2.11}$$

where

$$a_1 = 1 + 0.5\Delta t \times 2\zeta + 0.25\Delta t^2 {\omega_n}^2 \tag{2.12}$$

$$a_2 = 1 - 0.5\Delta t \times 2\zeta - 0.25\Delta t^2 {\omega_n}^2 \tag{2.13}$$

$$a_3 = -\Delta t {\omega_n}^2 \tag{2.14}$$

and α=0 and Δt is the time step or one over the sampling frequency. To compute the acceleration time history, we use the central difference method (Chopra, 2007).

3. Basic wave relationships

Seismic energy propagates through the earth in waves. There are 2 categories of waves: body waves, which are separated into compressional (P) waves, shear (S) waves and surface waves which are separated into Raleigh and Love waves. P wave particle motion is parallel to the direction of propagation. P waves are the fastest wave with velocity:

$$\alpha = \left(\frac{\lambda+2\mu}{\rho}\right)^{1/2} \tag{3.1}$$

where λ and μ are Lame's constants and ρ is the density of the material. S wave particle motion is perpendicular to the direction of propagation. S waves are the second fastest of the type of wave with velocity:

$$\beta = \left(\frac{\mu}{\rho}\right)^{1/2} \tag{3.2}$$

Lame's constants are always positive, thus α is always greater than β.

Surface waves are slower than body waves and propagate along the free surface, arriving at the end of the seismic record. Rayleigh waves are a "ground roll wave" in which particle motion at the free surface is elliptical. Love waves describe horizontal shear wave motion at the free surface.

Waves propagating through the subsurface refract at interfaces defined by the relationship

$$\frac{\sin\theta_1}{\alpha_1} = \frac{\sin\delta_1}{\beta_1} = \frac{\sin\theta_2}{\alpha_2} = \frac{\sin\delta_2}{\beta_2} \tag{3.3}$$

where α and β are the P and S wave velocities respectively, θ_1 and θ_2 are the reflected and refracted P waves and δ_1 and δ_2 are the reflected and refracted S waves (Fig.3.1). This is known as Snell's law.

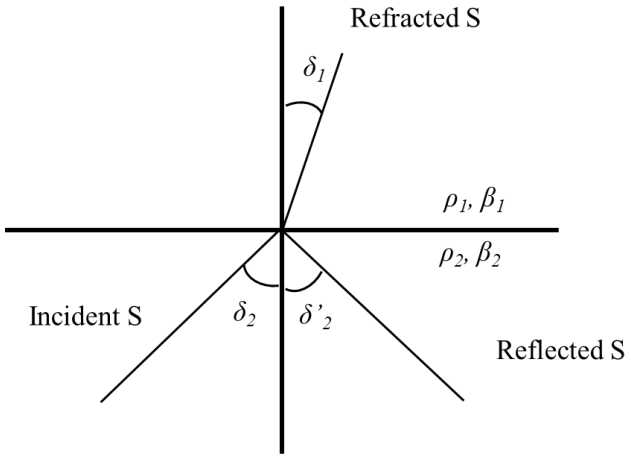

Figure 3.1. Snell's law for an incident S wave. Cartoon based off fig 3.1 (coincidence) in Sheriff and Geldart 1995.

Since the Earth's layers tend to have increasing density with depth, seismic waves refract towards nearly vertical at the surface which is indicated by the refracted S wave in figure 3.1 (Sheriff and Geldart, 1995).

4. Statistics, signal processing and optimization tools

4.1 Pearson's Correlation Coefficient

Pearson's correlation coefficient, also known as Pearson's *r*, is a measure of the strength of association between two continuous variables. It measures linear correlation, is not resistant to outliers and assumes the data follows bivariate normal distribution. It is given as

$$\rho_{XY} = \frac{E[(x-\mu_x)(y-\mu_y)]}{\sigma_X \sigma_Y} \tag{4.1}$$

where E is the expected value operator, μ_x is the mean of x, σ_x is the standard deviation of x and $\sigma_X \sigma_Y$ is the covariance between x and y. The estimator for Pearson's *r* is

$$r = \frac{1}{n+1} \sum_{i=1}^{n} \left(\frac{x_i - \bar{X}}{s_x}\right)\left(\frac{y_i - \bar{Y}}{s_y}\right) \tag{4.2}$$

Where $\bar{X}$ is the maximum likelihood estimator for the mean of x and s_x is the maximum likelihood estimator for the standard deviation of x (Class notes from CEE-202).

4.2 Normalized Cross Correlation

Normalized cross correlation is used to compare two signals. It yields a correlation coefficient and a lag time at each point in a vector equal to the sum of the lengths of the signal plus 1. First, we the subtract the mean out of the signal "S",

$$S_{corr} = S - mean(S) \tag{4.3}$$

then we normalize each signal by the square root of each respective total energy.

$$S_{norm} = S / \sqrt{\sum_{i=1}^{n} S_{corr}^2} \tag{4.4}$$

This initial step is effectively finding the values needed at each point to compute Pearson's *r* (equation 1.4.2). To find the linear cross correlation between two signals, we use

$$r_{yx}(k) = \frac{1}{L}\sum_{i=0}^{L-1} y(i)x(i-k) \quad (4.5)$$

Where *y(k)* is an L point signal, *x(k)* is an M point signal where $M \leq L$ and $0 \leq k \leq L$ (Schilling, 2016).

4.3 Differential Evolution

Differential Evolution is an optimization technique designed to find a global minimum of an objective function. Simple minimization techniques like the downhill simplex method solve for a minimum that depends on their starting position. This is ideal for optimization problems where there is one minimum, however, in problems where the objective function space has multiple minima, methods like downhill simplex fail. Differential evolution attempts to overcome this issue by applying the theory of evolution to optimization techniques.

Differential evolution starts with an initial "population" which is a set of vectors with values for each of the different inputs. These values are then run through the objective function, or "simulated", after which they are assessed based on their "fitness" or how small the objective function output is given the attributes in the vector. From this population, the best subset population is selected which have the best attributes. The vectors with the best attributes are then combined, or "mate" which produce "children" vectors. A subset of the next generation is manipulated or "mutated". This child population is then simulated through the objective function and are assessed for their fitness. Following this step, the process repeats until a global minimum is reached. The mutation aspect of differential evolution is essential for a successful minimization of the objective function space because it provides a more robust exploration of the space.

5. Basic earthquake engineering topics

5.1 Introduction

Currently, in earthquake engineering practice in the U.S, we classify the study area into one of three tectonic regimes: active crustal, subduction and stable (Carlton et al. 2015). California, which is home to the transform San Andreas Fault, is an example of an active crustal regime. Alaska and Cascadia, which lie on convergent plate boundaries with a plunging oceanic plate beneath that of a crustal plate are examples of subduction zones. The central and eastern U.S, which lie on intercontinental crust and a passive margin respectively, are examples of stable crustal regions. These regimes each present their own unique regional effects and, coupled with local site effects, form the bulk of seismic hazard analyses.

5.2 Earthquake Measurement

Earthquake ground motions apply dynamic stresses to buildings and other infrastructure. The effects of earthquake ground motion are dependent on the magnitude of ground shaking and resilience of the building. The resonance between the two entities is governed by the equation for the amplification of a system relative to its static response as a function of the damping ratio, the ratio of excitation frequency and natural frequency of the structure. The same theory applies to ground motion where the shaking basement rock acts as the excitation frequency and the soft overburden the resonating structure. Ground resonance can ultimately be factored into ground-structure coupling.

5.3 Recording and earthquake

We record and process ground motions using an instrument called a seismometer. A seismometer is, in principle, a mass on a spring that responds to the Earth's motion. It records these motions dependent on time which, together with a timer forms a seismograph setup. This is recorded on paper or electronically digitized, the output recording of which is called the seismogram. Today, we generally record acceleration time histories and integrate them to

compute velocity and displacement time histories using the Newmark-β method.

$$v_{n+1} = v_n + \Delta t \times [(1-\beta) \times a_n + \beta \times a_{n+1}] \tag{5.1}$$

$$u_{n+1} = u_n + \Delta t \times v_n + \Delta t^2[(0.5-\alpha) \times a_n + \alpha \times a_{n+1}] \tag{5.2}$$

where a_n, v_n and u_n are the acceleration, velocity and displacement time histories at sample n respectively, Δt is the sampling time interval and α and β are quadratic convergence coefficients and are 0.25 and 0.5 respectively.

5.4 Magnitude

Historically, measuring the magnitude of an earthquake has always posed a problem in the seismology community because ground motion records are site and path dependent and thus the magnitude must be back-calculated from the seismogram recording. The *Richter scale* was the first systematic scale for quantifying earthquake magnitude. It is one of many "local scales" meaning its arbitrary definitions are not transferable from region to region. The *moment magnitude* M_o is a measure of the amount of work done by an earthquake as a function of Area*slip*G (shear modulus). We often think of moment magnitude as being "the best" measure of earthquake magnitude because it quantifies the amount of energy released by the earthquake and is thus translatable from one earthquake to another.

5.5 Intensity

Earthquake moment magnitude is a function of the work done by the earthquake. In earthquake engineering, we are interested in the *effects* of earthquake on human populations and therefore we must look at local ground motion parameters. The *intensity* of ground shaking is a measure of site-specific shaking. Subjective intensity scales have been around since the pioneering Mercalli Intensity scale, invented in 1902 and still in use today though changed slightly, now called the Modified Mercalli Intensity scale (MMI). The MMI is a measure of ground shaking based on

human observation of effects from the earthquake. For example, an intensity V on the scale is “felt by nearly everyone; many awakened. Some dishes, windows broken”. The higher the scale, the more observed structural damage takes over from what people feel. There are two reasons to use the modified Mercalli intensity scale: to collect more data from the general population to enhance ground motion data or provide data where there is none, and to quantify past earthquakes with little or no ground motion. The USGS program “did you feel it” provides a questionnaire for people who may have felt an earthquake. These data are compiled and used to make a Mercalli intensity map which can be correlated to objective ground motion data (USGS Modified Mercalli Intensity Web Page). Historical seismicity is a field that often uses subjective accounts of earthquakes to glean an understanding of the earthquake. For example, the 1755 Cape Ann earthquake was a significant event that occurred of the North Shore of Massachusetts (Ebel, 2006). It was recorded by priests, scientists, newspapers and the public. The author used the accounts to estimate its objective magnitude which can be factored into estimates of east coast seismic recurrence interval important for building codes and local infrastructure.

There are several important parameters used by geotechnical earthquake engineers to objectively analyze ground shaking including but not limited to: peak ground acceleration, velocity and displacement, Bolt bracketed duration, Arias intensity, significant duration, rate of Arias intensity, and ground motion orbit. PGA, PGV and PGD are the maximum values computed at the acceleration, velocity and displacement time histories at both horizontal components respectively. The Bolt bracketed duration is defined as the time difference between the first time a seismic record exceeds a threshold of 0.5g or -0.5g and the last time it exceeds it. The Arias intensity (I_a) is a measure of the energy contained in an earthquake record and is computed by integrating over the squared acceleration record

$$I_a = \frac{\pi}{2g}\int_0^{\infty}[a(t)]^2 dt \tag{5.3}$$

It is in units of velocity and is useful in that it includes the effect of amplitude, frequency content and duration. A plot of the Arias intensity is called a Husid plot. The significant duration is defined as the time difference between the 95th percentile of the normalized Arias intensity and the 5th percentile. The rate of increase of the Arias intensity is the I_a value of the 90th percentile of the normalized Arias intensity plot. The ground motion orbit is the horizontal orthogonal components of the record plotted against one another. This plot displays the motion of the ground in map view during the event. Some shapes tend to be more destructive than other shapes such as ovals and figure eights (Kramer, 1996).

6. On the HVSR

The method of the ratio of the horizontal to vertical spectrum was first developed by Nogoshi and Igarashi in 1971 to determine whether microtremors were predominantly surface waves or body waves (Nogoshi and Igarashi, 1970b, 1971; Nakamura, 2019). They conclude that the microtremor is predominantly Rayleigh waves from analysis of theoretical microtremor simulations performed (Suzuki, 1933; Ohta, 1963). In 1989, however, Nakamura derived the same technique of microtremor H/V ratio to image vertically propagating shear waves. He showed that the ratio of the horizontal to vertical spectra approximates the fundamental peak of the shear wave site transfer function. He writes: “the spectrum of the horizontal components and vertical component of microtremor bears resemblance to [the] transfer function for horizontal motion layers.” (Nakamura 1989). He rebuts Nogoshi and Igarashi by saying “there is little Rayleigh-wave energy in the lower frequency range, and Rayleigh waves predominate at higher frequencies.” (Nakamura, 2019). His proof, he then argues, that the ratio of the horizontal to the vertical spectra

approximates the fundamental peak of the shear wave transfer function, holds. The common name for this method is “Nakamura’s HVSR”, he prefers, however, that it be renamed the “quasi transfer spectrum” to distinguish it from the Rayleigh wave HVSR of Nogoshi and Igarashi, though in this work, we use HVSR. It is challenging to justify Nakamura’s HVSR using physics, he does it using logic and relationships. For this reason, the method has stirred significant controversy. In fact, he writes that he does not consider the HVSR “ a scientific tool for theoretical exploration or pursuit of truth” (Nakamura, 2019). I suggest reading Nakamura’s 2019 opinion paper to better understand the context in which he developed the method and the justifications he gives as well as the history of the Rayleigh wave interpretation vs the shear wave interpretation.

7. Background analyses

7.1 Inversion of the $HVSR_{avg}$ onto the TTF optimization analysis

We generate a TTF using Nrattle with depth = 40, ${}^{i}Q^{-1}$ = 0.05 and applied the brute force method with depth bounds (0, 100) and ${}^{i}Q^{-1}$ bounds (0, 0.20) to solve for the fabricated TTF parameters. The resulting contour plot (Fig. 7.1) displays the results with the color representing the function value. The smallest value, therefore is the minimum of value of *S* from Eq. 16 and the X and Y coordinates are the solutions for depth and ${}^{i}Q^{-1}$ respectively.

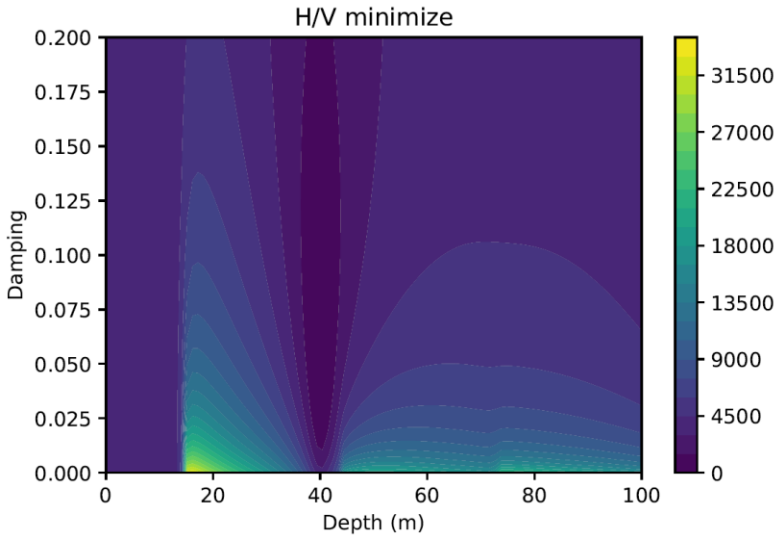

Figure 7.1. Contour plot generated from brute force optimization with depth bounds (0, 100) and ${}^{i}Q^{-1}$ bounds (0, 0.20). Each axis used 100 samples for a total 10,000 iterations.

This method successfully solves the minimum solution but takes 14:25 hours. The objective function value for this example is 0 at a depth of 40 and an ${}^{i}Q^{-1}$ value of 0.05. The same analysis for the HVSR at station CE32 using the 2017 Puebla event using bounds of depth: (30, 100) and ${}^{i}Q^{-1}$: (0, .15) yields the result in Figure 7.2. Figure 7.2 strongly resembles Figure 5.1 except the low function value band at low depths is cut out and there is an increase of noise. A clear global minimum is apparent in dark blue at about (40, 0.02).

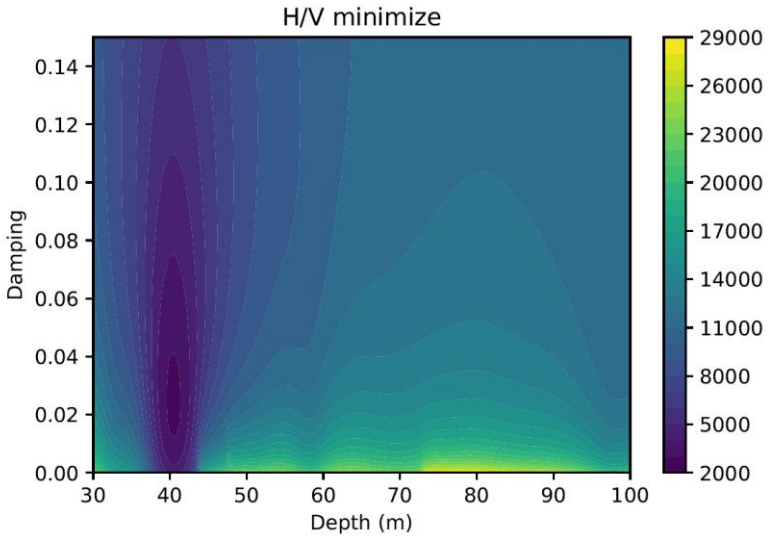

Figure 7.2. Contour plot generated from brute force optimization with depth bounds (30, 100) and ${}^{i}Q^{-1}$ bounds (0, 0.20) applied to the HVSR of the 2017 Puebla earthquake waveform at CE32. Each axis uses 100 samples for a total 10,000 iterations.

The brute force optimization technique takes too long so we tested two other minimization strategies: downhill simplex and differential evolution. Using the downhill simplex algorithm at a starting point (75, 0.14), the minimization fails, solving for a point at (123, 0.08). This means that there are multiple minima in the optimization space and that there are two options for minimization: pick a starting point and hope it yields the correct solution or use global minimization solution techniques (Fig. 7.3).

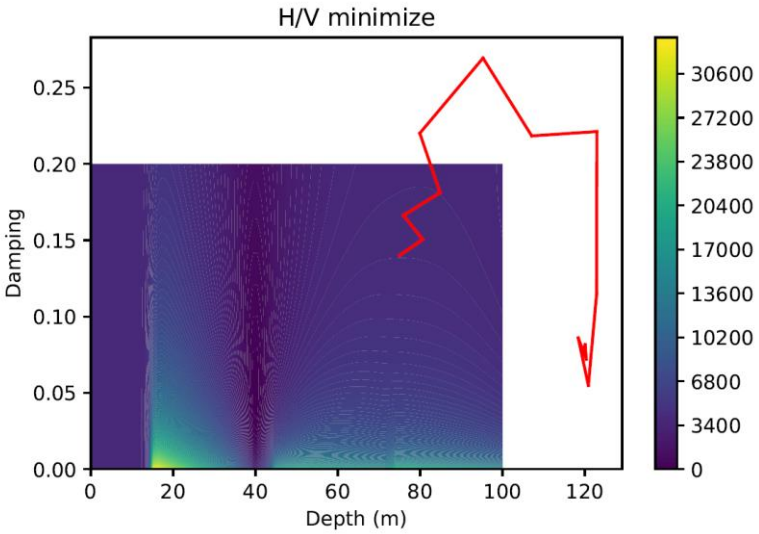

Figure 7.3. Downhill simplex algorithm path (red line) overlying the solution space computed from the brute algorithm. Starting point is at (75, 0.14) and the final point is at (123, 0.08). The total time was 10 minutes. The underlying image is the brute force algorithm solution to fabricated TTF in Fig. 7.1.

The same starting point and algorithm were used on the HVSR from station CE32 and the Puebla event and the algorithm succeeded in finding the global minimum (Fig. 7.4)

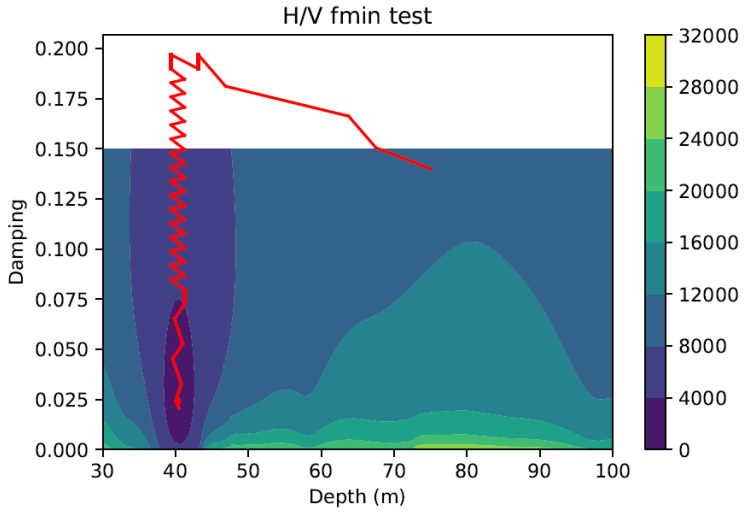

Figure 7.4. Downhill simplex algorithm path (red line) overlying the solution space computed from the brute algorithm on the HVSR computed using ground motion data at station CE32 from the 2017 Puebla earthquake. Starting point is at (75, 0.14) and the final point is at (40, 0.025).

The solution space of the objective function has multiple local minima thus, global optimization techniques are a good strategy to solve the problem consistently across different events and stations. We applied differential evolution to the same event and station and solved for the global minimum (Fig. 7.5).

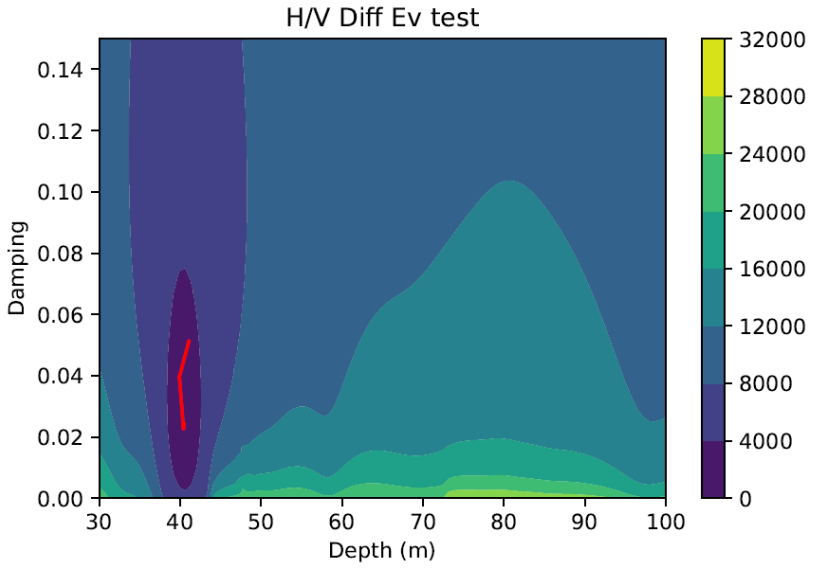

Figure 7.5. The path differential evolution takes to solve the same problem presented in Figure 7.4.

For this event and station, the Puebla earthquake and station CE32, the differential evolution algorithm requires 10 iterations, 333 function evaluations and 28 minutes and 45 seconds. This was a manageable amount of time, so we applied differential evolution to all 60 non-hill or compact zone stations to solve for the inverted TTF.

5.2 Interpolation vs datacutting

The output of the MATLAB FFT function in a complex vector equal to the length of the input time vector. Since the Mexico City database contains records of varying lengths, the output HVSR of each record at a station varies from one event to the next. In order to compute statistics median, standard deviation and 95% confidence interval at each frequency per Thompson et al. 2009, the HVSR of each event at a station must have the exact same frequency vector as each other event at the station. We test two methods of accomplishing this, 1) linear interpolation onto a vector with number of samples equal to the largest sample number event at the station and 2) cutting each event to the length of the shortest event.

To do the linear interpolation method, we loop through every event recorded at a station in the database and find the lowest sampling frequency (fs_{min}), lowest number of samples (N_{min}) and highest number of samples (N_{max}) in the database. We then go through each event and compute its HVSR and linear interpolate it onto a vector with maximum frequency fs_{min} /2 – 1, the Nyquist frequency minus 1, and number of frequencies $N_{max}/2 – fs_{min}$, half the maximum number of samples minus the number of samples per frequency, which in this case is fs_{min}. A station with events that have an fs_{min} of 50, and an N_{max} of 1000 will have HVSRs that are linearly interpolated onto a vector of 500 equally spaced frequencies between 0 and 49 Hz.

To cut each event to N_{min}, we cut around the maximum amplitude of each signal. Since the maximum amplitude tends to be near the arrival of the S wave, we cut ¼ * N_{min} before the max amplitude and ¾ * N_{min} after the max amplitude. This maintains most of the shear wave information of each signal. If a cut length falls before the start of the signal or after N_{max}, the algorithm shifts the cut window by the value exceeding one of those two points.

Cutting the data to the record with the fewer number of samples does not significantly change the shape of $HVSR_{avg}$. It does, however, affect the sigma value. In Figure 7.6, the grey bars indicate the 95% confidence interval and are clearly wider for the HVSR computed from cut waveforms compared to linearly interpolated waveforms. The sigma values calculated for each peak are similarly higher for the cut HVSRs than the interpolated HVSRs (Fig. 7.6).

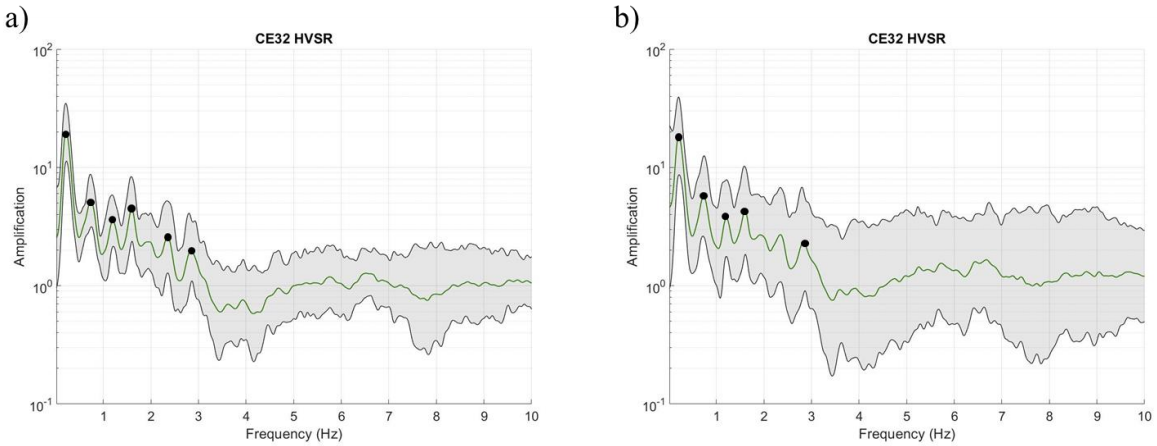

Figure 7.6. a) Mexico City lake zone station CE32 with HVSRs linearly interpolated onto a frequency vector with half the number of samples the event with the greatest number of samples. b) the same station with all waveforms cut to the event with the least number of samples. Identified peaks for each are indicated in black.

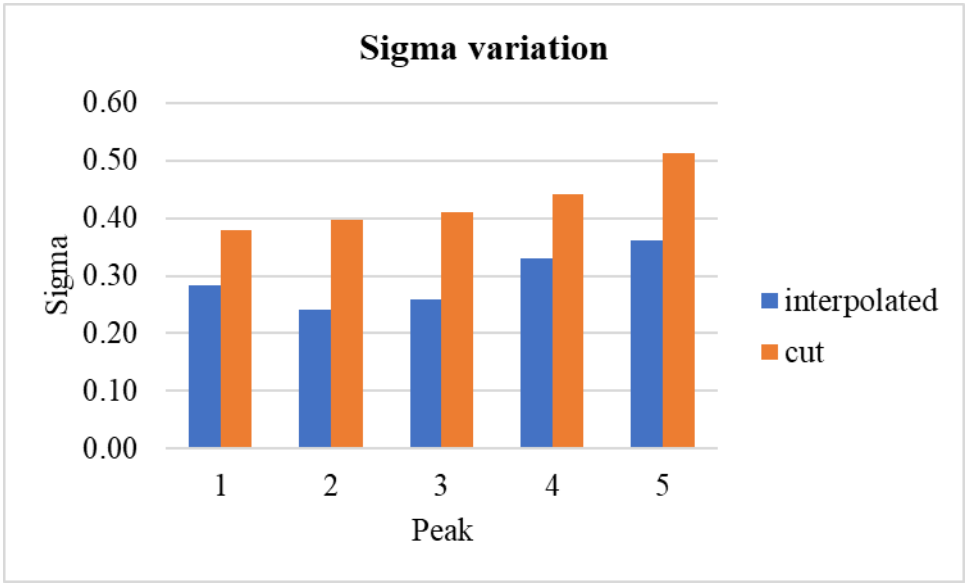

Figure 7.7. Differences of the sigma value of each peak. The five peaks are the five indicated in Figure 7.6a, excluding one peak as this was not identified by the algorithm for the cut waveform.

Whereas the sigma values are significantly different between the two methods, the amplitudes are consistent. There is enough discrepancy, however, that the cut waveforms also have one fewer peak than the interpolated waveforms because of the amplitude discrepancy (Fig. 7.8). Because the shape was not changed significantly, we think that using linear interpolation is a valid method of analyzing a dataset with different length records when applying the FFT to each record and use that method in this study.

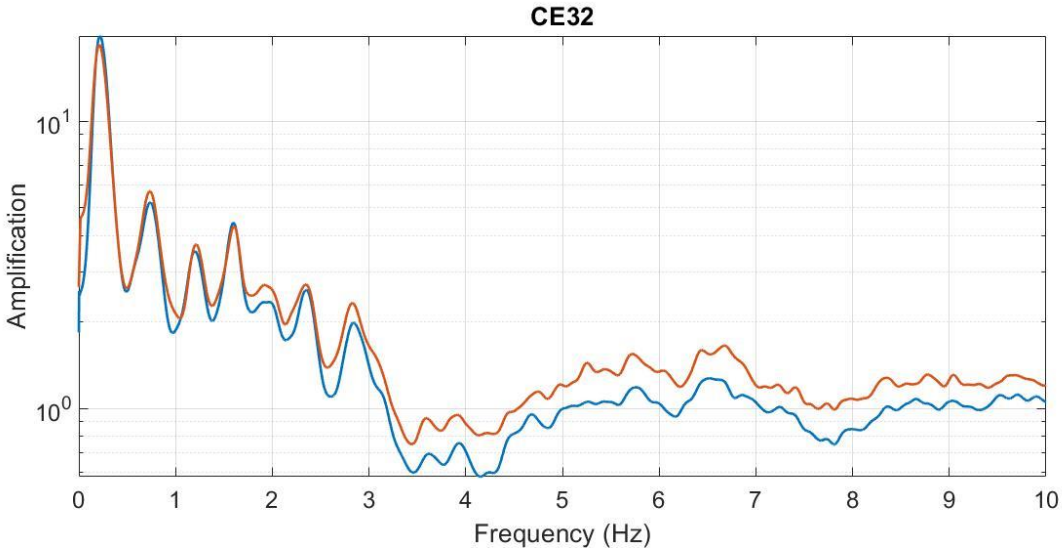

Figure 7.8. $HVSR_{avg}$ for both interpolation (blue) and wavecutting (orange). The shapes are similar but with a slight amplitude discrepancy.

The linearly interpolated HVSRs maintain all the information in every waveform in the database and have much lower interevent variabilities than the cut waveforms, which removed information. Both display similar shapes, though the amplitudes of the HVSRs of the cut waveforms are slightly lower than those of the interpolated waveforms. Linear interpolation

provides similar enough results to cutting the waveform around the maximum S-wave amplitude that we think it is a viable strategy to combining waveforms of varying length. The lower sigma values at higher frequencies of the interpolation method are likely due to the increased influence of surface and shear waves which show up in the vertical axis thus decreasing the H/V ratio.

5.3 Anomalously high HPB sigma stations

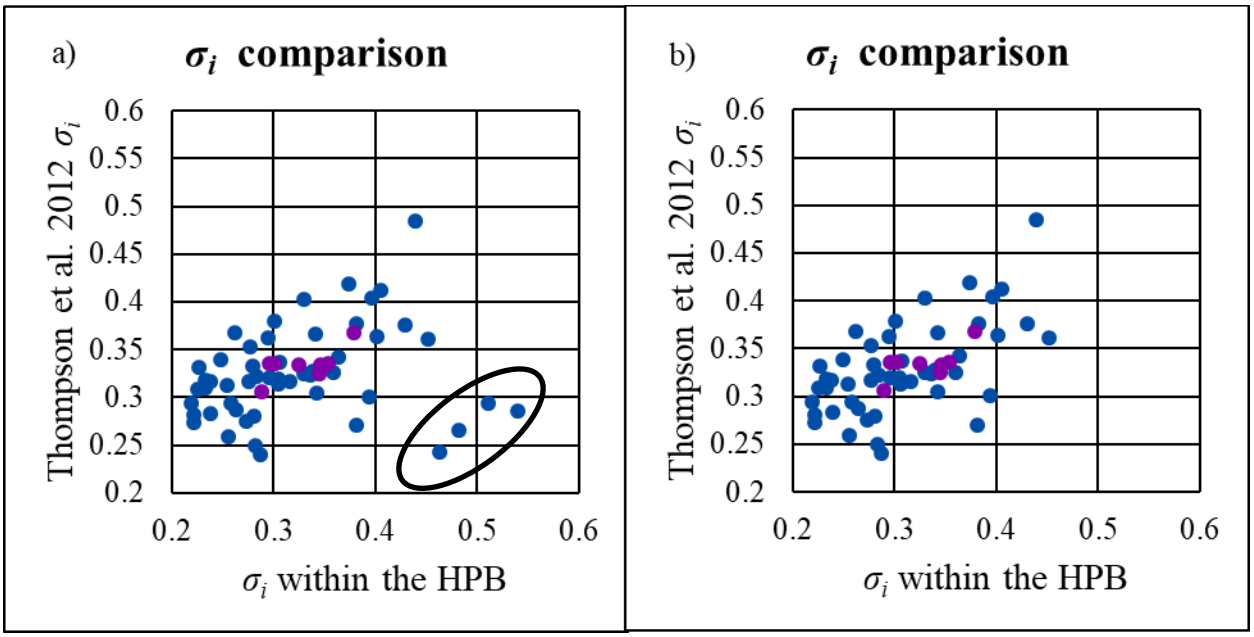

Figure 7.9. Comparison of σ_i between the Thompson et al. 2012 definition and the definition defined in this paper between f_a and f_b, the half power bandwidth. Transition zone stations are indicated in purple and lake zone stations are indicated in blue. a) stations AE02, HA41, NZ31 with anomalously high σ_i between the halfpower bandwidth compared to the Thompson et al. 2012 definition are circled in black. b) the same plot but without anomalous stations.

There are two explanations for these anomalously high values of σ_i 1) a large discrepancy in the amplitude of the HVSRs as we see in AE02 and NZ31 and 2) stations that have few events, but several bad signals contained in the computation. These bad signals do not significantly affect the average as the shape is visually consistent, but they do increase the sigma value and thus, the value of σ_i between the halfpower bandwidth. In these instances, using more of the HVSR over which to take the median to compute σ_i per the Thompson et al. 2012 definition is advantageous

in getting a more accurate value of σ_i because it helps negate the significant effect bad signals have on the fundamental peak. For the case of AE02 and NZ31, however, these HVSR have many events that we use to compute the HVSR, but these events do appear to have varying fundamental peak shapes which come out in the σ_i computation. These sites could, therefore be experiencing some complexity that is contained in the fundamental peak.

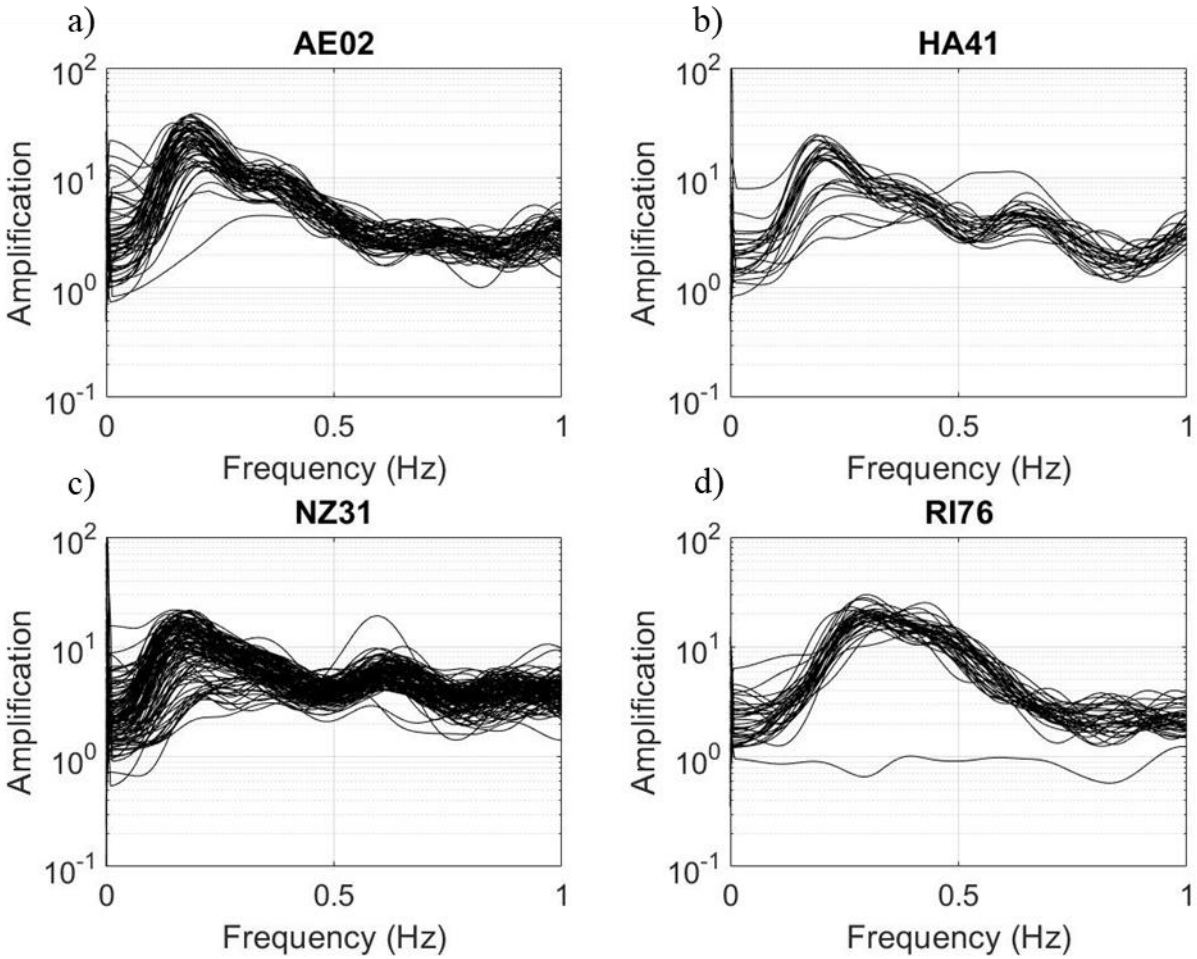

Figure 7.10. Each individual HVSR plotted for the four stations that exhibit anomalously high σ_i values compared to the Thompson et al. (2012) statistics.

TABLES

Table 1. Station information
Station database used to make Figure 10. The information was contained in the RACM network data files.

Station	Latitude	Longitude	Elevation	Soil
CE18	19.3398	-99.0847	2240	Compact
CP28	19.4385	-99.0839	2240	Compact
CT64	19.4876	-99.1137	2240	Compact
PA34	19.2016	-99.0491	2240	Compact
CS78	19.3656	-99.2262	2430	Hills
FJ74	19.299	-99.21	2240	Hills
IM40	19.3428	-99.2032	2365	Hills
TE07	19.427	-99.222	2290	Hills
UI21	19.37	-99.2642	N/A	Hills
TP13	19.2922	-99.1708	N/A	Hills
AE02	19.429	-99.0584	2232	Lake Zone
AL01	19.4356	-99.1453	2232	Lake Zone
AP68	19.3809	-99.1068	2232	Lake Zone
AR14	19.4808	-99.076	2232	Lake Zone
AU11	19.3919	-99.0869	2234	Lake Zone
BA49	19.4097	-99.145	2233	Lake Zone
BL45	19.4253	-99.1481	2232	Lake Zone
BO39	19.4653	-99.1047	2232	Lake Zone
CA20	19.3877	-99.1578	2232	Lake Zone
CA59	19.4258	-99.1183	2233	Lake Zone
CB43	19.3877	-99.1578	2232	Lake Zone
CC55	19.3877	-99.1578	2232	Lake Zone
CE23	19.4619	-99.0642	2233	Lake Zone
CE32	19.3858	-99.0537	2233	Lake Zone
CH84	19.33	-99.1254	2234	Lake Zone
CI05	19.4186	-99.1653	2233	Lake Zone
CJ03	19.4097	-99.1567	2233	Lake Zone
CJ04	19.4098	-99.1566	2233	Lake Zone
CO56	19.4215	-99.159	2233	Lake Zone
CU80	19.2938	-99.1037	2232	Lake Zone
DM12	19.4312	-99.0963	2232	Lake Zone
DX37	19.3322	-99.1439	2240	Lake Zone
EX08	19.4236	-99.1602	2233	Lake Zone

EX09	19.4236	-99.1602	2233	Lake Zone
EX12	19.4236	-99.1602	2232	Lake Zone
GA62	19.4385	-99.1401	2232	Lake Zone
GC38	19.3161	-99.1059	2233	Lake Zone
HA41	19.418	-99.079	2233	Lake Zone
HJ72	19.4251	-99.1301	2232	Lake Zone
IB22	19.345	-99.1297	2234	Lake Zone
JA43	19.4053	-99.125	2234	Lake Zone
JC54	19.313	-99.1272	2237	Lake Zone
LI33	19.3064	-98.9631	2238	Lake Zone
LI58	19.4263	-99.1569	2233	Lake Zone
LV17	19.4931	-99.1275	2233	Lake Zone
MI15	19.2834	-99.1253	2237	Lake Zone
MY19	19.3461	-99.0433	2237	Lake Zone
NZ20	19.4027	-99	2232	Lake Zone
NZ31	19.4167	-99.0247	2234	Lake Zone
PD42	19.4055	-99.0997	2234	Lake Zone
PE10	19.3809	-99.1318	2232	Lake Zone
RI76	19.4473	-99.1	2232	Lake Zone
RM48	19.4359	-99.128	2232	Lake Zone
SI53	19.3753	-99.1483	2235	Lake Zone
SP51	19.3656	-99.1189	2234	Lake Zone
TH35	19.279	-99	2238	Lake Zone
TL08	19.45	-99.134	2232	Lake Zone
TL55	19.436	-99.143	2232	Lake Zone
UC44	19.434	99.165	2234	Lake Zone
VG09	19.454	-99.123	2233	Lake Zone
VM29	19.381	-99.125	2234	Lake Zone
XP06	19.42	-99.135	2232	Lake Zone
AO24	19.358	-99.1539	2235	Transition
AU46	19.3832	-99.1681	2233	Transition
CO47	19.3714	-99.1703	2247	Transition
DR16	19.5005	-99.1829	2233	Transition
EO30	19.3885	-99.1772	2236	Transition
ES57	19.4017	-99.1775	2242	Transition
GR27	19.4747	-99.1797	2238	Transition
ME52	19.4383	-99.182	2238	Transition

Table 2. Event information

Earthquake database used in this study containing 218 events. The average earthquake magnitude was calculated from the average of the given non-zero magnitudes. If one magnitude was given, that was considered the average magnitude. The latitude longitude coordinates and average magnitude were used to make Figure 11.

Date	Epicenter Time	Magnitude	Latitude	Longitude	Mag avg
15-Jul-87	7:16:13	Mb = 6.0, Mc=5.7	17.39	-97.26	5.85
8-Feb-88	13:51:29	Mc = 5.0	17.49	-101.15	5.00
10-Mar-89	19:51.0	Mc = 5.0	17.44	-101.08	5.00
25-Apr-89	14:29:00	Mc = 6.5	16.6	-99.4	6.50
2-May-89	9:30:16	Mc = 5.1	16.63	-99.51	5.10
12-Aug-89	15:31:49	Mc = 4.8	18.12	-101.03	4.80
11-May-90	23:43:49	Mb = 5.30, Ms = 4.90, Mc = 5.30	17.046	-100.84	5.17
31-May-90	7:35:26	Mb = 5.80, Ms = 5.90, Mc = 5.50	17.106	-100.893	5.73
14-Jan-91	21:11:06	Mb = 5.30, Ms = 5.00, Mc = 5.10	17.838	-101.854	5.13
1-Apr-91	7:34:45	Mb = 5.50, Ms = 5.40, Mc = 5.30	16.044	-98.387	5.40
18-Aug-91	13:18:12	Mc = 3.80	19.33	-99.24	3.80
12-Feb-92	11:56:58	Mb = 5.10, Ms = 4.60, Mc = 4.40	17.733	-101.058	4.70
31-Mar-92	20:56:33	Mb = 5.20, Ms = 5.10, Mc = 4.70	17.233	-101.302	5.00
7-Jun-92	17:41:10	Ms = 5.3	16.22	-98.87	5.30
31-Mar-93	10:18:15	Mb = 5.30, Ms = 5.00, Mc = 5.30	17.18	-101.02	5.20
15-May-93	3:11:56	Mb = 5.90, Ms = 5.90, Mc = 6.00	16.47	-98.72	5.93
15-May-93	3:09:39	Mb = 5.80, Ms = 5.80, Mc = 5.80	16.43	-98.74	5.80
29-Jul-93	20:17:01	Mb = 5.00, Ms = 4.20, Mc = 5.00	17.38	-100.65	4.73
5-Aug-93	1:20:48	Mb = 4.90, Mc = 5.10	17.08	-98.53	5.00
3-Sep-93	12:35:00	Mb = 5.80, Ms = 6.80, Mc = 6.50	13.98	-92.79	6.37
10-Sep-93	10:50:23	Mb = 4.8, Mc = 4.8	16.57	-98.94	4.80
10-Sep-93	19:12:54	Mb = 6.30, Ms = 7.30	14.14	-92.82	6.80
24-Oct-93	7:52:18	Mb = 6.20, Ms = 6.60, Mc = 6.50	16.54	-98.98	6.43
23-Feb-94	14:13:51	Mb = 5.40, Mc = 5.00	17.82	-97.3	5.20
14-Mar-94	20:51:32	Mc = 6.50	15.67	-93.01	6.50
23-May-94	1:41:46	Mc = 5.60	18.03	-100.57	5.60
4-Jul-94	21:36:43	Mc = 5.90	14.83	-97.29	5.90
29-Oct-94	16:44:04	Mc = 5.10	16.97	-99.89	5.10
10-Dec-94	16:17:40	Mc = 6.6	17.98	-101.52	6.60
10-Dec-94	16:46:46	Mc = 6.30	18.02	-101.56	6.30
13-Dec-94	8:23:46	Mb = 5.30, Ms = 4.90, Mc = 5.10	15.85	-98.79	5.10
27-Apr-95	6:42:25	Mb = 4.9, Ms = 4.4, Mc = 4.9	17.88	-101.64	4.73
14-Sep-95	14:04:30	Mc=6.4, Mb = 7.2, Me = 7.3	16.31	-98.88	6.97

9-Oct-95	15:35:51	Mc = 6.5, Mb = 7.3, Me = 7.5	18.74	-104.67	7.10
12-Oct-95	16:53:04	Mc = 5.5, Mb = 5.5, Me = 6.1	19.04	-103.2	5.70
21-Oct-95	2:38:59	Mc = 6.2, ME = 6.5	16.92	-93.62	6.35
30-Oct-95	14:47:56	ME = 5.5	16.35	-98.5	5.50
20-Dec-95	21:52:27	Mb = 5.3, Mc = 5.0	18.43	-101.16	5.15
8-Jan-96	9:20:12	Mb = 4.9, Ms = 4.2, Mc = 4.9	15.63	-98.05	4.67
25-Feb-96	3:08:13	Ms = 6.9	15.83	-98.25	6.90
25-Feb-96	9:17:57	Mb = 5.6, Ms = 5.4, Mc = 5.4	15.86	-98.13	5.47
25-Feb-96	14:27:24	Mb = 5.2, Ms = 5.3, Mc = 5.2	15.48	-98.04	5.23
25-Feb-96	4:17:04	Mb = 5.10, Mc = 4.8	15.42	-98.16	4.95
25-Feb-96	14:44:06	Mb = 4.6, Ms = 4.9, Mc = 5.0	15.54	-97.88	4.83
26-Feb-96	1:37:32	Mb = 5.1, Ms = 4.4, Mc = 5.1	15.77	-97.92	4.87
13-Mar-96	21:04:19	Mb = 5.2, Ms = 4.4, Mc = 5.1	16.52	-99.08	4.90
19-Mar-96	17:12:39	Mb = 5.8, Ms = 5.2, Mc = 5.6	15.49	-97.55	5.53
27-Mar-96	12:34:48	Mb = 5.5, Ms = 4.9, Mc = 4.6	16.21	-98.25	5.00
23-Apr-96	6:53:35	Mb = 5.3, Ms = 4.9, Mc = 5.3	17.11	-101.6	5.17
15-Jul-96	21:23:38	Ms = 6.5	17.4	-101.1	6.50
16-Jul-96	11:39:54	Mb = 4.4, Mc = 4.7	17.36	-101.22	4.55
18-Jul-96	8:16:46	Mb = 4.9, Ms = 4.7, Mc = 5.1	17.54	-101.2	4.90
19-Jul-96	9:00:55	Mb = 4.8, Ms = 3.9, Mc = 4.8	17.35	-100.29	4.50
11-Jan-97	20:28:27	Ms = 6.9	17.9	-103	6.90
21-Jan-97	21:19:58	Mb = 5.1, Ms = 5.0	16.44	-98.15	5.05
3-Apr-97	21:22:31	Mc = 5.1	17.98	-98.33	5.10
8-May-97	15:58:29	Mb = 5.0, Ms = 4.3, Mc = 4.8	17.32	-100.44	4.70
22-May-97	7:50:55	Ms = 6.0	18.4	-101.8	6.00
22-May-97	7:50:55	Ms = 6.0	18.4	-101.8	6.00
19-Jul-97	14:22:04	Ms = 6.3	15.8	-98.3	6.30
19-Jul-97	7:34:37	Mb = 4.6, Ms = 3.8, Mc = 4.9	17.22	-100.56	4.43
16-Dec-97	11:44:02	Mb = 5.5, Ms = 5.5, Mc = 4.7	15.95	-99.05	5.23
16-Dec-97	11:48:29	Mc = 6.0	15.7	-99.04	6.00
22-Dec-97	5:22:07	Ms = 5.0	17.1	-101.2	5.00
22-Dec-97	5:22:07	Ms = 5.0	17.1	-101.2	5.00
10-Jan-98	8:20:10	Ma = 6.3	14.29	-91.82	6.30
3-Feb-98	3:02:01	Mb = 6.0, Ms = 6.2, Mc = 6.4, Ma = 6.4'	15.69	-96.37	6.25
5-Mar-98	4:12:55	Mb = 5.3, Ms = 4.5, Mc = 4.9, Ma = 5.1	16.05	-98.43	4.95
18-Mar-98	11:56:04	Mc = 4.3	20.1	-99.23	4.30
20-Apr-98	22:59:17	Mb = 5.4, Mc = 5.0, Ma = 5.5, Me = 5.7	18.37	-101.21	5.40
9-May-98	17:03:13	Mb = 4.8, Ms = 4.7, Mc = 4.8, Ma = 5.2, Me = 5.1	17.34	-101.41	4.92
16-May-98	17:41:52	Mb = 5.0, Ms = 4.3, Mc = 5.1, Ma = 5.1, Me = 5.3	17.25	-101.35	4.96
7-Jun-98	23:20:16	Mb = 5.8, Mc = 5.2, Ma = 5.6, Me = 6.2	15.82	-94.07	5.70

5-Jul-98	19:55:07	Mb = 4.9, Ms = 4.5, Mc = 4.9	16.83	-100.12	4.77
11-Jul-98	5:21:12	Mb = 4.6, Ms = 4.7, Mc = 4.9, Ma = 5.3, Me = 5.4	17.25	-101.54	4.98
12-Jul-98	8:11:27	Mb = 5.1, Ms = 4.6, Mc = 4.8, Ma = 5.2, Me = 5.4	16.83	-100.44	5.02
17-Jul-98	11:18:04	Mc = 4.6	16.98	-100.16	4.60
9-Aug-98	16:18:06	Mb = 4.2, Mc = 4.5	16.87	-100.25	4.35
6/15/1999	20:42:07	Mb = 6.4, Ms = 6.5, Me = 7.0	18.18	-97.51	6.63
21-Jun-99	17:43:05	Mc = 6.0, Ms = 5.8, Mc = 5.8, Me = 6.2	17.99	-101.72	5.95
30-Sep-99	16:31:14	Mb = 6.5, Ms = 7.5, Mc = 5.2, Ma = 7.1, Me = 7.6	15.95	-97.03	6.78
14-Dec-99	7:12:16	Mb = 4.8, Mc = 4.5	17.96	-98.54	4.65
29-Dec-99	5:19:46	Mb = 6.1, Ms = 5.4, Mc = 5.1, Ma = 5.6, Me = 5.9	18.02	-101.68	5.62
12-Mar-00	22:21:32	Mb = 5.5, Ms = 5.8, Mc = 5.4, Ma = 5.8, Me = 5.9	14.59	-92.97	5.68
18-Mar-00	0:50:58	Mb = 4.8, Ms = 4.3, Mc = 4.7	17.08	-99.31	4.60
21-Jul-00	6:13:39	Mb = 5.4, Ms = 5.1, Mc = 5.4, Ma = 5.5, Me = 6.0	18.09	-98.97	5.48
9-Aug-00	11:41:47	Mb = 6.1, Ms = 6.5, Mc = 0.0, Ma = 6.5, Me = 7.0	17.99	-102.66	6.53
12-Dec-00	14:07:45	Mb = 5.3, Ms = 5.1, Mc = 5.3, Ma = 5.3, Me = 5.4	17.94	-102.58	5.28
13-Jan-01	17:33:46	Mc = 7.6	13.15	-89.94	7.60
26-Jan-01	14:19:39	Mb = 5.0, Ms = 0.0, Mc = 4.8, Ma = 0.0, Me = 0.0	16.2	-97.98	4.90
5-Mar-01	10:17:36	Mb = 5.0, Ms = 4.5, Mc = 4.9, Ma = 5.0, Me = 5.2	17.13	-100.06	4.92
6-Mar-01	21:57:56	Mb = 5.1, Ms = 4.5, Mc = 5.1, Ma = 4.9, Me = 5.3	17.14	-100.1	4.98
20-May-01	4:21:37	Mb = 5.5, Ms = 6.0, Mc = 6.5, Ma = 6.3, Me = 6.5	18.64	-105.12	6.16
14-Sep-01	17:13:15	Mb = 0.0, Ms = 0.0, Mc = 2.9, Ma = 0.0, Me = 0.0	19.31	-99.3	2.90
8-Oct-01	3:39:19	Mb = 5.6, Ms = 5.4, Mc = 5.5, Ma = 7.6, Me = 6.1	16.94	-100.14	6.04
29-Oct-01	5:23:12	Mb = 5.0, Ms = 4.5, Mc = 5.1, Ma = 5.1, Me = 5.4	17	-100.19	5.02
10-Nov-01	17:09:01	Mb = 5.3, Ms = 5.1, Mc = 5.1, Ma = 5.7, Me = 5.9	15.96	-98.17	5.42
15-Nov-01	22:18:22	Mb = 0.0, Ms = 0.0, Mc = 3.5, Ma = 0.0, Me = 0.0	19.56	-99.16	3.50
23-Nov-01	6:41:37	Mb = 4.7, Ms = 0.0, Mc = 4.9, Ma = 5.8, Me = 5.1	16.96	-100.19	5.13
16-Jan-02	23:09:55	Mb = 0.0, Ms = 0.0, Mc = 6.7, Ma = 0.0, Me = 0.0	15.43	-93.55	6.70
30-Jan-02	8:42:04	Mb = 5.6, Ms = 0.0, Mc = 5.5, Ma = 5.2, Me = 5.4	18.1	-95.97	5.43
1-Feb-02	19:29:11	Mb = 0.0, Ms = 0.0, Mc = 2.6, Ma = 0.0, Me = 0.0	19.52	-99.21	2.60
18-Apr-02	5:02:45	Mb = 5.4, Ms = 6.0, Mc = 6.3, Ma = 6.2, Me = 6.5	16.77	-101.12	6.08
18-Apr-02	17:57:19	Mb= 5.0, Ms = 0.0, Mc = 5.9, Ma = 5.8, Me = 6.0	16.66	-101.89	5.68
7-Jun-02	17:00:52	Mb = 5.3, Ms = 5.1, Mc = 4.8, Ma = 5.4, Me = 5.6	15.91	-96.97	5.24
19-Jun-02	21:50:08	Mb = 5.2, Ms = 0.0, Mc = 5.5, Ma = 5.1, Me = 5.3	16.24	-98.09	5.28
30-Aug-02	21:11:43	Mb = 4.8, Ms = 4.8, Mc = 5.0, Ma = 5.3, Me = 5.3	16.69	-100.93	5.04
25-Sep-02	18:14:48	Mb = 5.2, Ms = 4.7, Mc = 5.3, Ma = 5.3, Me = 5.3	16.86	-100.12	5.16
27-Sep-02	7:04:58	Mb = 5.2, Ms = 4.6, Mc = 4.9, Ma = 5.1, Me = 5.4	17.16	-100.59	5.04
4-Nov-02	10:00:45	Mb = 5.2, Ms = 0.0, Mc = 4.9, Ma = 5.2, Me = 5.2	17.25	-101.6	5.13
8-Nov-02	23:20:42	Mb = 5.1, Ms = 4.5, Mc = 5.0, Ma = 5.1, Me = 5.3	16.21	-98.14	5.00
10-Dec-02	3:09:35	Mb = 5.1, Ms = 0.0, Mc = 5.1, Ma = 5.3, Me = 5.5	17.41	-101.26	5.25
10-Jan-03	2:08:02	Mb = 5.1, Ms = 4.5, Mc = 4.9, Ma = 5.1, Me = 5.3	16.97	-100.3	4.98

22-Jan-03	2:06:34	Mb = 6.5, Ms = 7.6, Mc = 0.0, Ma = 7.2, Me = 7.6	18.6	-104.22	7.23
27-Mar-03	7:44:23	Mb = 4.8, Ms = 0.0, Mc = 4.8, Ma = 4.9, Me = 5.1	18.01	-101.78	4.90
16-Nov-03	3:17:13	Mb = 0.0, Ms = 0.0, Mc = 4.0, Ma = 0.0, Me = 0.0	19.18	-98.97	4.00
19-Nov-03	13:50:28	Mb = 4.9, Ms = 0.0, Mc = 4.8, Ma = 4.8, Me = 4.8	17.86	-99.54	4.83
26-Nov-03	5:04:26	Mb = 0.0, Ms = 0.0, Mc = 3.6, Ma = 0.0, Me = 0.0	19.19	-98.97	3.60
1-Jan-04	23:31:49	Ms = 6.3	17.31	-101.42	6.30
1-Jan-04	23:57:56	Mc = 5.8	16.97	-98.97	5.80
13-Jan-04	21:28:56	Mc = 5.5	15.9	-97.03	5.50
6-Feb-04	19:11:35	Mc = 5.0	18.26	-102.8	5.00
7-Aug-04	11:49:12	Mc = 5.3	17.1	-95.48	5.30
18-Aug-04	9:03:10	Mc = 5.7	16.33	-95.14	5.70
13-Sep-04	20:58:34	Ms = 3.1	19.37	-99.11	3.10
28-Oct-04	20:30:02	Mc = 4.6	18.34	-99.74	4.60
15-Nov-04	2:38:39	Mc = 5.1	15.98	-98.72	5.10
14-Aug-05	2:51:56	Mc = 5.8	15.94	-97.93	5.80
20-Feb-06	10:54:23	Mc = 5.0	18.16	-100.75	5.00
11-Aug-06	14:30:41	Mc = 5.9	18.32	-101.27	5.90
13-Apr-07	5:42:22	Me = 6.3	17.09	-100.44	6.30
13-Apr-07	8:43:50	Me = 5.4	16.97	-100.27	5.40
19-Apr-07	10:02:09	Me = 5.2	17.21	-101.37	5.20
28-Apr-07	13:56:35	Mc = 5.0	16.94	-99.82	5.00
6-Nov-07	6:35:42	Mc = 5.6	17.08	-100.14	5.60
26-Nov-07	21:56:16	Mc = 5.6	18.05	-101.31	5.60
12-Feb-08	12:50:18	Mc = 6.6	16.19	-94.54	6.60
28-Apr-08	0:06:29	Mc = 5.6	18.05	-100.01	5.60
23-Sep-08	22:46:15	Mc = 5.2	16.42	-100.14	5.20
20-Oct-08	5:00:52	Mc = 5.1	17.25	-102.09	5.10
31-Jan-09	13:24:58	Mc = 5.3	17.54	-101.96	5.30
27-Mar-09	8:48:16	Mc = 5.3	17.35	-100.82	5.30
27-Apr-09	16:46:27	Mc = 5.7	16.9	-99.58	5.70
22-May-09	19:24:18	Mc = 5.7	18.13	-98.44	5.70
15-Aug-09	13:22:45	Mc = 5.4	18.06	-100.67	5.40
9-Feb-10	0:47:40	Mc = 5.8	15.9	-98.86	5.80
20-Apr-10	2:28:57	Mc = 5.0	16.64	-98.46	5.00
30-Jun-10	7:22:27	Mc = 6.0	16.22	-98.03	6.00
7-Apr-11	13:11:22	Mc = 6.7	17.2	-94.34	6.70
26-Apr-11	11:07:28	Mc = 5.5	16.71	-99.69	5.50
5-May-11	13:24:07	Mc = 5.5	16.61	-98.91	5.50
5-May-11	13:24:08	Mc = 5.8	16.71	-98.92	5.80
11-Dec-11	1:47:25	Mc = 6.5	17.84	-99.98	6.50

20-Mar-12	18:02:50	Mc = 7.4	16.42	-98.36	7.40
20-Mar-12	18:02:50	Mc = 7.4	16.42	-98.36	7.40
2-Apr-12	17:36:42	Mc = 6.0	16.27	-98.47	6.00
11-Apr-12	22:55:10	Mc = 6.4	17.9	-103.06	6.40
13-Apr-12	10:10:03	Mc = 5.2	16.11	-98.34	5.20
1-May-12	16:37:59	Mc = 5.6	18.2	-101.01	5.60
24-Jul-12	5:25:28	Mc = 5.0	16.27	-98.31	5.00
22-Sep-12	12:29:57	Mc = 5.4	16.23	-98.3	5.40
29-Sep-12	7:11:10	Mc = 5.5	15.89	-98.67	5.50
7-Nov-12	16:35:51	Mc = 7.3	14.08	-92.32	7.30
15-Nov-12	9:20:22	Mc = 6.1	18.17	-100.52	6.10
20-Feb-13	21:23:11	Mc = 5.6	18.6	-104.04	5.60
26-Mar-13	13:04:45	Mc = 5.4	15.78	-98.61	5.40
26-Mar-13	13:12:17	Mc = 5.0	15.94	-98.45	5.00
5-Apr-13	1:58:48	Mc = 5.3	17.08	-100.82	5.30
12-Apr-13	3:45:09	Mc = 5.2	17.78	-101.58	5.20
22-Apr-13	1:16:34	Mc = 5.8	17.87	-102.19	5.80
16-Jun-13	5:19:02	Mc = 5.8	18.11	-99.22	5.80
16-Jun-13	5:19:03	Mc = 5.8	18.11	-99.22	5.80
13-Aug-13	16:50:42	Mc = 5.0	16.56	-98.57	5.00
16-Aug-13	15:32:59	Mc = 5.1	16.54	-98.59	5.10
21-Aug-13	12:38:30	Mc = 6.0	16.79	-99.56	6.00
21-Aug-13	13:02:18	Mc = 5.0	16.73	-99.7	5.00
10-Mar-14	0:37:57	Mc = 5.8	15.79	-98.55	5.80
5-Apr-14	1:58:48	Mc = 5.3	17.08	-100.82	5.30
18-Apr-14	14:27:23	Mc = 7.2	17.18	-101.19	7.20
8-May-14	17:00:16	Mc = 6.4	17.11	-100.87	6.40
10-May-14	7:36:01	Mc = 6.1	17.06	-100.95	6.10
20-May-14	1:39:14	Mc = 5.0	18.04	-100.1	5.00
21-May-14	10:06:15	Mc = 5.8	17.11	-95.07	5.80
24-May-14	8:24:45	Mc = 5.7	16.21	-98.42	5.70
7-Jul-14	11:23:58	Mc = 6.9	14.75	-92.63	6.90
23-Jul-14	0:28:14	Mc = 5.2	16.59	-100.47	5.20
29-Jul-14	10:46:14	Mc = 6.4	17.63	-95.66	6.40
11-Aug-14	1:09:42	Mc = 5.2	16.38	-98.19	5.20
13-Aug-14	6:48:11	Mc = 5.4	16.13	-98.35	5.40
1-Dec-14	8:50:07	Mc = 3.4	19.37	-99.23	3.40
20-Mar-15	22:30:08	Mc = 5.4	17.96	-98.58	5.40
28-Apr-15	18:56:53	Me = 5.5	17.03	-95.19	5.50
30-Sep-15	17:25:55	Mc = 5.5	17.83	-101.52	5.50

23-Nov-15	20:41:20	Mc = 5.6	16.86	-98.94	5.60
10-Apr-16	7:11:21	Mc = 5.4	15.74	-96.37	5.40
8-May-16	7:33:59	Mc = 6.0	16.25	-97.98	6.00
27-Jun-16	20:50:33	Mc = 5.7	16.2	-97.93	5.70
27-Jun-16	20:52:33	Mc = 5.7	16.2	-97.93	5.70
19-Jul-16	13:42:46	Mc = 5.1	17.48	-98.08	5.10
22-Sep-16	18:08:59	Mc = 5.0	17.97	-98.49	5.00
23-Sep-16	7:54:50	Mc = 4.8	16.74	-99.45	4.80
2-Dec-16	13:57:55	Mc = 4.9	17.35	-101.34	4.90
12-Jan-17	10:26:57	Mc = 5.0	16.59	-98.56	5.00
2-Feb-17	0:52:09	Mc = 5.0	17.2	-101.28	5.00
13-Feb-17	7:29:31	Mc = 5.0	17.02	-99.74	5.00
18-Aug-17	5:15:11	Mc = 5.3	16.84	-100.49	5.30
8-Sep-17	4:49:18	Mc = 8.2	14.85	-94.11	8.20
19-Sep-17	18:14:40	Mc = 7.1	18.4	-98.72	7.10
23-Sep-17	12:52:59	Mc = 6.1	16.48	-94.9	6.10
25-Dec-17	20:23:10	Mc = 5.0	16.86	-99.85	5.00
13-Feb-18	21:39:36	Mc = 2.5	19.45	-99.09	2.50
16-Feb-18	23:39:38	Mc = 7.2	16.25	-98.03	7.20
19-Feb-18	6:56:57	Mc = 6.0	16.25	-97.77	6.00
20-Mar-18	17:46:53	Mc = 5.3	15.87	-98.72	5.30
16-May-18	14:20:29	Mc = 5.2	18.18	-100.47	5.20
21-May-18	2:15:19	Mc = 5.1	17.08	-98.68	5.10
19-Jul-18	13:31:54	Mc = 5.9	17.77	-97.89	5.90
22-Aug-18	18:03:09	Mc = 5.3	16.5	-98.75	5.30

Table 5. Inversion results and Thompson et al. (2012) classification

Station	Latitude	Longitude	Elevation	Soil	Depth	Damp	sigma	r	Class
AE02	19.429	-99.058	2232	Lake Zone	87.3955	0.02	0.24	0.28	LP
AL01	19.4356	-99.145	2232	Lake Zone	31.9579	0.03	0.31	0.52	LP
AP68	19.3809	-99.107	2232	Lake Zone	58.9228	0.02	0.28	-0.09	LP
AR14	19.4808	-99.076	2232	Lake Zone	66.0157	0.02	0.28	0.45	LP
AU11	19.3919	-99.087	2234	Lake Zone	74.9806	0.02	0.28	0.52	LP
BA49	19.4097	-99.145	2233	Lake Zone	44.997	0.03	0.31	0.54	LP
BL45	19.4253	-99.148	2232	Lake Zone	39.7368	0.04	0.33	0.54	LP
BO39	19.4653	-99.105	2232	Lake Zone	43.9814	0.03	0.40	0.48	HP
CA20	19.3877	-99.158	2232	Lake Zone	19.1634	0.04	0.34	0.62	LG
CA59	19.4258	-99.118	2233	Lake Zone	52.0136	0.02	0.33	0.50	LP

CB43	19.3877	-99.158	2232	Lake Zone	19.9032	0.01	0.32	0.58	LP
CC55	19.3877	-99.158	2232	Lake Zone	18.0614	0.04	0.32	0.63	LG
CE23	19.4619	-99.064	2233	Lake Zone	71.7123	0.03	0.26	0.49	LP
CE32	19.3858	-99.054	2233	Lake Zone	76.8948	0.02	0.25	0.57	LP
CH84	19.33	-99.125	2234	Lake Zone	24.2692	0.02	0.34	0.54	LP
CI05	19.4186	-99.165	2233	Lake Zone	32.0427	0.04	0.41	0.49	HP
CJ03	19.4097	-99.157	2233	Lake Zone	33.3339	0.03	0.32	0.60	LG
CJ04	19.4098	-99.157	2233	Lake Zone	33.6048	0.03	0.34	0.60	LP
CO56	19.4215	-99.159	2233	Lake Zone	39.1622	0.03	0.32	0.54	LP
CU80	19.2938	-99.104	2232	Lake Zone	48.6099	0.04	0.49	0.39	HP
DM12	19.4312	-99.096	2232	Lake Zone	61.3109	0.02	0.30	0.38	LP
DX37	19.3322	-99.144	2240	Lake Zone	17.5032	0.03	0.31	0.57	LP
EX08	19.4236	-99.16	2233	Lake Zone	26.1224	0.01	0.35	0.23	HP
EX09	19.4236	-99.16	2233	Lake Zone	37.8074	0.03	0.42	0.40	HP
EX12	19.4236	-99.16	2232	Lake Zone	38.8914	0.03	0.36	0.38	HP
GA62	19.4385	-99.14	2232	Lake Zone	33.4782	0.03	0.32	0.36	LP
GC38	19.3161	-99.106	2233	Lake Zone	29.3256	0.02	0.37	0.52	HP
HA41	19.418	-99.079	2233	Lake Zone	79.993	0.02	0.29	0.17	LP
HJ72	19.4251	-99.13	2232	Lake Zone	38.2814	0.03	0.28	0.60	LP
IB22	19.345	-99.13	2234	Lake Zone	25.7413	0.03	0.32	0.58	LP
JA43	19.4053	-99.125	2234	Lake Zone	53.6254	0.02	0.29	0.45	LP
JC54	19.313	-99.127	2237	Lake Zone	20.1509	0.02	0.31	0.46	LP
LI33	19.3064	-98.963	2238	Lake Zone	55.039	0.05	0.36	0.52	HP
LI58	19.4263	-99.157	2233	Lake Zone	38.0863	0.03	0.29	0.48	LP
LV17	19.4931	-99.128	2233	Lake Zone	26.0404	0.04	0.32	0.46	LP
MI15	19.2834	-99.125	2237	Lake Zone	24.238	0.03	0.40	0.45	HP
MY19	19.3461	-99.043	2237	Lake Zone	51.204	0.04	0.27	0.73	LG
NZ20	19.4027	-99	2232	Lake Zone	94.9577	0.02	0.24	0.45	LP
NZ31	19.4167	-99.025	2234	Lake Zone	90.1681	0.02	0.27	0.45	LP
PD42	19.4055	-99.1	2234	Lake Zone	80.7122	0.01	0.27	0.37	LP
PE10	19.3809	-99.132	2232	Lake Zone	40.2566	0.02	0.38	0.58	HP
RI76	19.4473	-99.1	2232	Lake Zone	49.7157	0.03	0.29	0.49	LP
RM48	19.4359	-99.128	2232	Lake Zone	41.6272	0.04	0.29	0.54	LP
SI53	19.3753	-99.148	2235	Lake Zone	24.2623	0.03	0.36	0.62	HG
SP51	19.3656	-99.119	2234	Lake Zone	34.5343	0.03	0.38	0.62	HG
TH35	19.279	-99	2238	Lake Zone	75.0953	0.03	0.33	0.22	LP
TL08	19.45	-99.134	2232	Lake Zone	33.7691	0.03	0.31	0.55	LP
TL55	19.436	-99.143	2232	Lake Zone	29.6549	0.03	0.32	0.44	LP

UC44	19.434	99.165	2234	Lake Zone	24.0959	0.03	0.33	0.50	LP
VG09	19.454	-99.123	2233	Lake Zone	39.4248	0.02	0.37	0.45	HP
VM29	19.381	-99.125	2234	Lake Zone	46.2056	0.03	0.38	0.55	HP
XP06	19.42	-99.135	2232	Lake Zone	46.2097	0.02	0.32	0.51	LP
AO24	19.358	-99.154	2235	Transition	18.8975	0.04	0.34	0.69	LG
AU46	19.3832	-99.168	2233	Transition	15.4787	0.04	0.33	0.53	LP
CO47	19.3714	-99.17	2247	Transition	8.48091	0.05	0.33	0.61	LG
DR16	19.5005	-99.183	2233	Transition	10.4687	0.03	0.34	0.60	LG
EO30	19.3885	-99.177	2236	Transition	9.71902	0.04	0.31	0.61	LG
ES57	19.4017	-99.178	2242	Transition	15.2054	0.04	0.34	0.61	LG
GR27	19.4747	-99.18	2238	Transition	13.7988	0.02	0.37	0.52	HP
ME52	19.4383	-99.182	2238	Transition	14.9988	0.03	0.33	0.58	LP

Table 6. Number of peaks

Station	Latitude	Longitude	Elevation	Soil	# peaks
AE02	19.429	-99.058	2232	Lake Zone	2
AL01	19.4356	-99.145	2232	Lake Zone	3
AP68	19.3809	-99.107	2232	Lake Zone	3
AR14	19.4808	-99.076	2232	Lake Zone	3
AU11	19.3919	-99.087	2234	Lake Zone	5
BA49	19.4097	-99.145	2233	Lake Zone	2
BL45	19.4253	-99.148	2232	Lake Zone	4
BO39	19.4653	-99.105	2232	Lake Zone	2
CA20	19.3877	-99.158	2232	Lake Zone	2
CA59	19.4258	-99.118	2233	Lake Zone	1
CB43	19.3877	-99.158	2232	Lake Zone	4
CC55	19.3877	-99.158	2232	Lake Zone	3
CE23	19.4619	-99.064	2233	Lake Zone	5
CE32	19.3858	-99.054	2233	Lake Zone	7
CH84	19.33	-99.125	2234	Lake Zone	4
CI05	19.4186	-99.165	2233	Lake Zone	2
CJ03	19.4097	-99.157	2233	Lake Zone	4
CJ04	19.4098	-99.157	2233	Lake Zone	3
CO56	19.4215	-99.159	2233	Lake Zone	2
CU80	19.2938	-99.104	2232	Lake Zone	6
DM12	19.4312	-99.096	2232	Lake Zone	2
DX37	19.3322	-99.144	2240	Lake Zone	3

EX08	19.4236	-99.16	2233	Lake Zone	2
EX09	19.4236	-99.16	2233	Lake Zone	1
EX12	19.4236	-99.16	2232	Lake Zone	2
GA62	19.4385	-99.14	2232	Lake Zone	2
GC38	19.3161	-99.106	2233	Lake Zone	4
HA41	19.418	-99.079	2233	Lake Zone	6
HJ72	19.4251	-99.13	2232	Lake Zone	3
IB22	19.345	-99.13	2234	Lake Zone	2
JA43	19.4053	-99.125	2234	Lake Zone	2
JC54	19.313	-99.127	2237	Lake Zone	3
LI33	19.3064	-98.963	2238	Lake Zone	2
LI58	19.4263	-99.157	2233	Lake Zone	3
LV17	19.4931	-99.128	2233	Lake Zone	5
MI15	19.2834	-99.125	2237	Lake Zone	2
MY19	19.3461	-99.043	2237	Lake Zone	3
NZ20	19.4027	-99	2232	Lake Zone	4
NZ31	19.4167	-99.025	2234	Lake Zone	5
PD42	19.4055	-99.1	2234	Lake Zone	2
PE10	19.3809	-99.132	2232	Lake Zone	4
RI76	19.4473	-99.1	2232	Lake Zone	3
RM48	19.4359	-99.128	2232	Lake Zone	2
SI53	19.3753	-99.148	2235	Lake Zone	3
SP51	19.3656	-99.119	2234	Lake Zone	5
TH35	19.279	-99	2238	Lake Zone	2
TL08	19.45	-99.134	2232	Lake Zone	3
TL55	19.436	-99.143	2232	Lake Zone	2
UC44	19.434	99.165	2234	Lake Zone	3
VG09	19.454	-99.123	2233	Lake Zone	2
VM29	19.381	-99.125	2234	Lake Zone	2
XP06	19.42	-99.135	2232	Lake Zone	4
AO24	19.358	-99.154	2235	Transition	3
AU46	19.3832	-99.168	2233	Transition	4
CO47	19.3714	-99.17	2247	Transition	2
DR16	19.5005	-99.183	2233	Transition	2
EO30	19.3885	-99.177	2236	Transition	3
ES57	19.4017	-99.178	2242	Transition	2
GR27	19.4747	-99.18	2238	Transition	2
ME52	19.4383	-99.182	2238	Transition	2

Table 7. First Peak Statistics

Station	Latitude	Longitude	Elevation	Soil	fn	a	HPB	sigma
AE02	19.429	-99.058	2232	Lake Zone	0.19	19.84	0.11	0.46
AL01	19.4356	-99.145	2232	Lake Zone	0.56	13.70	0.23	0.25
AP68	19.3809	-99.107	2232	Lake Zone	0.28	16.53	0.15	0.24
AR14	19.4808	-99.076	2232	Lake Zone	0.26	15.95	0.13	0.27
AU11	19.3919	-99.087	2234	Lake Zone	0.23	14.13	0.14	0.28
BA49	19.4097	-99.145	2233	Lake Zone	0.38	16.95	0.16	0.31
BL45	19.4253	-99.148	2232	Lake Zone	0.43	13.45	0.20	0.23
BO39	19.4653	-99.105	2232	Lake Zone	0.37	13.51	0.19	0.40
CA20	19.3877	-99.158	2232	Lake Zone	0.90	11.88	0.31	0.31
CA59	19.4258	-99.118	2233	Lake Zone	0.32	15.71	0.15	0.34
CB43	19.3877	-99.158	2232	Lake Zone	0.89	13.81	0.29	0.28
CC55	19.3877	-99.158	2232	Lake Zone	0.85	10.33	0.48	0.32
CE23	19.4619	-99.064	2233	Lake Zone	0.21	15.05	0.14	0.26
CE32	19.3858	-99.054	2233	Lake Zone	0.22	19.77	0.12	0.28
CH84	19.33	-99.125	2234	Lake Zone	0.74	24.65	0.14	0.36
CI05	19.4186	-99.165	2233	Lake Zone	0.52	13.24	0.24	0.41
CJ03	19.4097	-99.157	2233	Lake Zone	0.52	11.91	0.22	0.30
CJ04	19.4098	-99.157	2233	Lake Zone	0.52	10.61	0.22	0.25
CO56	19.4215	-99.159	2233	Lake Zone	0.46	16.72	0.14	0.33
CU80	19.2938	-99.104	2232	Lake Zone	0.36	11.18	0.16	0.44
DM12	19.4312	-99.096	2232	Lake Zone	0.28	22.51	0.12	0.39
DX37	19.3322	-99.144	2240	Lake Zone	1.00	12.83	0.27	0.34
EX08	19.4236	-99.16	2233	Lake Zone	0.46	14.58	0.16	0.28
EX09	19.4236	-99.16	2233	Lake Zone	0.47	17.03	0.15	0.37
EX12	19.4236	-99.16	2232	Lake Zone	0.46	14.73	0.15	0.29
GA62	19.4385	-99.14	2232	Lake Zone	0.48	13.83	0.22	0.23
GC38	19.3161	-99.106	2233	Lake Zone	0.61	22.80	0.16	0.26
HA41	19.418	-99.079	2233	Lake Zone	0.21	12.47	0.12	0.54
HJ72	19.4251	-99.13	2232	Lake Zone	0.39	12.58	0.29	0.22
IB22	19.345	-99.13	2234	Lake Zone	0.69	18.89	0.17	0.30
JA43	19.4053	-99.125	2234	Lake Zone	0.32	18.67	0.14	0.26
JC54	19.313	-99.127	2237	Lake Zone	0.88	20.97	0.19	0.23
LI33	19.3064	-98.963	2238	Lake Zone	0.33	5.52	0.28	0.45
LI58	19.4263	-99.157	2233	Lake Zone	0.47	17.95	0.14	0.26
LV17	19.4931	-99.128	2233	Lake Zone	0.52	10.67	0.19	0.34

MI15	19.2834	-99.125	2237	Lake Zone	0.74	13.98	0.35	0.33
MY19	19.3461	-99.043	2237	Lake Zone	0.34	10.57	0.12	0.22
NZ20	19.4027	-99	2232	Lake Zone	0.17	11.30	0.11	0.29
NZ31	19.4167	-99.025	2234	Lake Zone	0.18	9.94	0.17	0.48
PD42	19.4055	-99.1	2234	Lake Zone	0.21	22.17	0.10	0.38
PE10	19.3809	-99.132	2232	Lake Zone	0.46	12.05	0.21	0.43
RI76	19.4473	-99.1	2232	Lake Zone	0.31	16.97	0.22	0.51
RM48	19.4359	-99.128	2232	Lake Zone	0.38	11.44	0.29	0.22
SI53	19.3753	-99.148	2235	Lake Zone	0.71	13.69	0.25	0.40
SP51	19.3656	-99.119	2234	Lake Zone	0.53	17.13	0.17	0.30
TH35	19.279	-99	2238	Lake Zone	0.21	8.13	0.29	0.36
TL08	19.45	-99.134	2232	Lake Zone	0.49	13.83	0.28	0.23
TL55	19.436	-99.143	2232	Lake Zone	0.59	13.78	0.28	0.28
UC44	19.434	99.165	2234	Lake Zone	0.71	13.72	0.32	0.28
VG09	19.454	-99.123	2233	Lake Zone	0.43	15.62	0.22	0.34
VM29	19.381	-99.125	2234	Lake Zone	0.38	14.96	0.15	0.38
XP06	19.42	-99.135	2232	Lake Zone	0.36	16.88	0.19	0.24
AO24	19.358	-99.154	2235	Transition	0.96	13.64	0.23	0.30
AU46	19.3832	-99.168	2233	Transition	1.14	10.73	0.35	0.33
CO47	19.3714	-99.17	2247	Transition	2.04	6.49	0.67	0.34
DR16	19.5005	-99.183	2233	Transition	1.72	9.13	0.34	0.30
EO30	19.3885	-99.177	2236	Transition	1.73	6.93	0.71	0.29
ES57	19.4017	-99.178	2242	Transition	1.21	10.71	0.45	0.35
GR27	19.4747	-99.18	2238	Transition	1.31	13.93	0.43	0.38
ME52	19.4383	-99.182	2238	Transition	1.19	12.76	0.32	0.35

Table 8. All peak statistics

Station	fn	a	HPB	sigma	p	w
'AE02'	0.19255	19.8398	0.10777	0.46377	17.1012	0.14371
'AE02'	1.41971	3.25474	1.12513	0.27922	1.05758	0.38564
'AL01'	0.56271	13.6959	0.2325	0.25428	11.9959	0.31053
'AL01'	1.64771	2.33226	0.7194	0.30182	0.87263	0.33355
'AL01'	2.70912	2.58147	0.63348	0.37119	1.15054	0.46601
'AP68'	0.28242	16.5317	0.14686	0.23882	13.8477	0.18604
'AP68'	2.15769	3.11352	1.01954	0.35028	1.46158	0.91533
'AP68'	8.01793	1.84437	2.42882	0.31504	0.70754	1.69493

'AR14'	0.2607	15.9458	0.13035	0.27311	13.743	0.17471
'AR14'	3.11657	1.6359	0.84333	0.49256	0.56953	0.40791
'AR14'	4.21072	1.57689	0.8137	0.39511	0.52377	0.22773
'AU11'	0.23385	14.128	0.14077	0.28112	12.3841	0.18184
'AU11'	0.65274	5.34894	0.20888	0.2882	1.61032	0.11464
'AU11'	1.14883	3.94316	0.20888	0.30167	2.09565	0.19147
'AU11'	2.46113	3.2053	0.31445	0.46958	1.04638	0.20122
'AU11'	3.15133	2.08966	0.51084	0.39592	0.67684	0.25157
'BA49'	0.37635	16.9529	0.15599	0.30546	14.8414	0.20935
'BA49'	1.73691	2.37193	0.44692	0.32189	0.79944	0.29792
'BL45'	0.42515	13.4468	0.19713	0.22699	11.6578	0.31042
'BL45'	1.34902	2.18713	0.30893	0.31315	0.91287	0.21215
'BL45'	1.80506	1.74758	0.48547	0.3194	0.5212	0.24068
'BL45'	2.43029	1.86573	0.54137	0.38313	0.63953	0.34867
'BO39'	0.37247	13.5077	0.18624	0.39607	12.5123	0.27278
'BO39'	7.20731	1.71365	1.75921	0.40238	0.52372	0.37885
'CA20'	0.89891	11.8779	0.31108	0.30678	10.123	0.45278
'CA20'	6.97027	1.64895	3.33174	0.32815	0.74969	2.21452
'CA59'	0.32492	15.7064	0.15326	0.33936	13.8926	0.21078
'CB43'	0.89286	13.8065	0.28975	0.28415	11.9356	0.40339
'CB43'	2.72365	5.25776	0.55375	0.33629	3.33846	0.58915
'CB43'	4.54586	4.65098	3.45125	0.32811	1.76216	1.29683
'CB43'	25.7577	1.14137	8.35339	0.4657	0.51638	6.67149
'CC55'	0.85413	10.3275	0.47764	0.316	8.56502	0.64056
'CC55'	3.02317	2.24607	0.53102	0.36057	0.94333	0.37235
'CC55'	8.41766	1.72285	1.75883	0.38892	0.73994	0.5419
'CE23'	0.20822	15.0468	0.1436	0.25584	12.8638	0.18527
'CE23'	0.96724	2.87898	0.35592	0.2674	1.39119	0.3003
'CE23'	3.50996	1.46032	0.68209	0.31525	0.6198	0.54309
'CE23'	6.93274	1.73052	1.29444	0.33168	0.70359	0.95141
'CE23'	12.7885	1.68548	3.32944	0.37247	0.50183	1.63513
'CE32'	0.21789	19.7689	0.12361	0.28281	17.2231	0.15708
'CE32'	0.73747	5.22349	0.19903	0.24084	2.67309	0.17713
'CE32'	1.20049	3.53174	0.20113	0.25858	1.51221	0.1587
'CE32'	1.59855	4.43596	0.16342	0.32918	2.60097	0.16078
'CE32'	2.35069	2.58784	0.23675	0.39597	0.85849	0.14766
'CE32'	2.84094	1.99174	0.28284	0.36066	0.89033	0.22784
'CE32'	6.51573	1.27581	2.53925	0.30504	0.52561	0.79958

'CH84'	0.74476	24.6508	0.14291	0.36442	22.5623	0.19297
'CH84'	1.92922	3.2537	0.29405	0.32593	1.2736	0.21571
'CH84'	4.5235	2.15122	0.84094	0.32647	1.04807	0.74722
'CH84'	17.1898	1.7835	17.7505	0.30508	0.58991	10.9415
'CI05'	0.52128	13.2415	0.2373	0.40531	11.488	0.30258
'CI05'	5.99338	1.57903	1.43027	0.42455	0.58918	0.86981
'CJ03'	0.51943	11.9058	0.21621	0.29608	10.2403	0.27415
'CJ03'	1.66191	2.29818	0.54757	0.28294	0.86236	0.26631
'CJ03'	2.4999	2.14168	0.59235	0.42862	0.89056	0.49488
'CJ03'	6.0476	1.891	3.82405	0.3117	0.55758	0.76593
'CJ04'	0.52278	10.6129	0.22452	0.24881	9.30141	0.3021
'CJ04'	1.60602	2.4882	0.48017	0.30941	1.06823	0.41818
'CJ04'	2.70401	2.70555	0.57686	0.44611	1.29961	0.51114
'CO56'	0.46061	16.7233	0.13547	0.33033	14.6126	0.18504
'CO56'	3.89541	1.61351	2.35517	0.35734	0.72686	0.70884
'CU80'	0.3632	11.1778	0.15689	0.43974	8.21663	0.18822
'CU80'	0.8489	6.62818	0.2407	0.32993	2.86185	0.1963
'CU80'	1.42917	3.00763	0.33526	0.48741	1.17634	0.24012
'CU80'	3.45149	1.34493	0.46206	0.49414	0.52681	0.32994
'CU80'	5.5039	0.92415	6.58491	0.31638	0.2782	0.87445
'CU80'	22.3143	1.77211	31.2891	0.2315	0.53866	5.35552
'DM12'	0.28409	22.5061	0.11559	0.39415	20.3277	0.15629
'DM12'	4.44742	1.77306	1.02467	0.41259	0.60305	0.57756
'DX37'	0.99916	12.8333	0.27235	0.3426	10.9843	0.34337
'DX37'	6.22139	1.96583	1.42573	0.3204	0.9166	1.30332
'DX37'	21.4582	1.89602	30.2292	0.27496	0.73119	10.6315
'EX08'	0.45948	14.5784	0.15918	0.2776	12.8076	0.37197
'EX08'	3.67746	6.90781	1.29967	0.41589	4.77819	1.53505
'EX09'	0.46768	17.0285	0.14769	0.37427	14.8542	0.29767
'EX12'	0.4562	14.7274	0.14605	0.29445	12.874	0.23236
'EX12'	3.66597	2.41832	1.22418	0.4193	0.84918	1.07023
'GA62'	0.48283	13.8253	0.22072	0.23337	12.0393	0.30458
'GA62'	1.74093	2.64924	0.61802	0.33105	1.21145	0.40729
'GC38'	0.60797	22.8044	0.15781	0.26206	20.5983	0.21064
'GC38'	1.42033	4.40785	0.31045	0.2668	2.02453	0.25826
'GC38'	2.42672	1.47563	0.49414	0.48252	0.56618	0.37844
'GC38'	6.55576	2.15824	1.43326	0.47112	1.0706	1.26168
'HA41'	0.21109	12.4676	0.11994	0.54001	10.4437	0.16872

'HA41'	1.04824	3.63026	0.24467	0.2574	1.17343	0.15632
'HA41'	1.71029	3.96757	0.39339	0.34229	2.24063	0.37968
'HA41'	3.12313	2.50812	0.43177	0.32492	0.95568	0.27236
'HA41'	4.10421	2.17731	0.27585	0.32298	0.81417	0.19098
'HA41'	5.33955	2.22924	0.35501	0.35784	1.03057	0.29019
'HJ72'	0.38804	12.5767	0.29301	0.22215	10.3134	0.34738
'HJ72'	1.41754	2.89203	0.70679	0.2665	0.85684	0.19474
'HJ72'	7.34901	1.94647	2.06493	0.34172	0.92099	1.2269
'IB22'	0.6947	18.8865	0.16705	0.30471	16.7206	0.22295
'IB22'	4.36439	2.1953	1.76061	0.33064	1.16675	1.70054
'JA43'	0.32079	18.6651	0.14189	0.25856	16.5283	0.19521
'JA43'	3.37904	2.62704	1.18598	0.36794	1.48578	1.16521
'JC54'	0.8839	20.9697	0.185	0.2261	18.973	0.27521
'JC54'	2.94463	1.67801	0.49591	0.28454	0.51259	0.25453
'JC54'	4.72014	3.32618	0.93272	0.40907	2.1988	1.01652
'LI33'	0.3345	5.52022	0.285	0.45191	3.58117	0.30251
'LI33'	1.04099	1.77183	0.405	0.34276	0.76467	0.30478
'LI58'	0.46748	17.9479	0.13939	0.26403	15.5845	0.2
'LI58'	2.65479	1.08261	0.85133	0.3255	0.32536	0.25076
'LI58'	6.28744	1.36596	2.23663	0.36686	0.54788	0.93895
'LV17'	0.52066	10.6745	0.18907	0.3364	9.04839	0.3576
'LV17'	0.91042	9.02282	0.19052	0.31723	3.02101	0.12453
'LV17'	1.79176	3.36955	0.68355	0.31486	1.19852	0.25259
'LV17'	5.00297	2.15253	1.35109	0.34383	0.87655	0.50338
'LV17'	6.49513	1.73368	3.0745	0.2932	0.52256	0.99597
'MI15'	0.7443	13.9849	0.34914	0.32953	12.2001	0.42585
'MI15'	6.42097	1.52315	1.55684	0.36016	0.49304	0.89663
'MY19'	0.34477	10.5696	0.11571	0.22179	9.30185	0.16904
'MY19'	1.15239	1.77654	0.27629	0.26462	0.77245	0.21692
'MY19'	2.43583	1.43839	0.34713	0.37298	0.75266	0.31075
'NZ20'	0.17156	11.3032	0.11379	0.28753	7.31177	0.1215
'NZ20'	2.39486	1.88921	0.29586	0.32922	0.72304	0.20997
'NZ20'	2.95856	1.83103	0.77378	0.35905	0.62952	0.24692
'NZ20'	3.99143	1.51461	0.87881	0.33568	0.46981	0.30072
'NZ31'	0.18332	9.9443	0.17314	0.48219	7.63645	0.23143
'NZ31'	0.6169	5.73008	0.19787	0.2476	1.87401	0.12144
'NZ31'	1.80851	2.54243	0.21533	0.43455	0.86786	0.13945
'NZ31'	2.25009	2.07716	0.32227	0.42781	0.69245	0.19218

'NZ31'	3.81635	1.19828	0.89043	0.41358	0.41186	0.27915
'PD42'	0.21129	22.1688	0.10313	0.38137	18.7014	0.13014
'PD42'	2.42233	2.97494	2.96063	0.33595	1.88989	3.04649
'PE10'	0.45554	12.0469	0.20535	0.42999	9.6844	0.27965
'PE10'	1.28165	4.408	0.38945	0.3326	1.36187	0.21682
'PE10'	2.0039	3.79254	0.53579	0.48401	1.57043	0.45549
'PE10'	3.44133	2.7843	0.62312	0.41352	1.30619	0.50814
'RI76'	0.31144	16.9652	0.21724	0.51103	14.8869	0.27319
'RI76'	3.39893	1.78444	0.64211	0.30129	0.83992	0.56064
'RI76'	5.27334	1.10668	1.3092	0.3752	0.37985	0.41206
'RM48'	0.37935	11.4426	0.29084	0.21922	9.52526	0.37126
'RM48'	7.93357	1.69861	3.43443	0.32655	0.82157	2.29427
'SI53'	0.71402	13.6931	0.2495	0.4015	12.1631	0.343
'SI53'	4.23653	1.5565	0.93726	0.36768	0.54337	0.58156
'SI53'	7.18454	1.99437	2.33411	0.3699	1.05415	2.08646
'SP51'	0.52674	17.1281	0.16977	0.30094	15.5169	0.23222
'SP51'	1.35349	4.28518	0.28837	0.32901	2.10864	0.25384
'SP51'	2.16512	1.94084	0.58953	0.41193	0.76309	0.4055
'SP51'	3.11047	1.77015	0.63953	0.4453	0.57932	0.32705
'SP51'	5.61279	1.61581	3.76977	0.36304	0.60576	2.05525
'TH35'	0.20833	8.12968	0.28543	0.35954	5.50069	0.32449
'TH35'	1.43862	2.76493	0.54297	0.38763	1.47833	0.51165
'TL08'	0.49289	13.8325	0.28131	0.23348	11.6953	0.34974
'TL08'	3.5103	1.56506	1.82007	0.34397	0.58495	0.50287
'TL08'	7.4053	1.83929	1.74794	0.32476	0.88595	1.18827
'TL55'	0.5888	13.7844	0.27808	0.2765	12.1779	0.36455
'TL55'	3.42185	1.77195	0.94261	0.34035	0.83666	0.84253
'UC44'	0.70619	13.719	0.32311	0.28	11.7446	0.39637
'UC44'	2.41835	2.72204	0.97267	0.34563	1.09069	0.49671
'UC44'	5.55955	2.10624	1.49898	0.3725	1.17586	1.296
'VG09'	0.42685	15.6205	0.22337	0.34194	13.9923	0.31895
'VG09'	2.22755	2.88075	0.48039	0.49361	1.23445	0.40506
'VM29'	0.38368	14.9573	0.14748	0.38222	13.3343	0.20092
'VM29'	2.95965	2.17083	0.97805	0.39101	0.86959	0.63335
'XP06'	0.36309	16.8791	0.19349	0.23809	14.3037	0.25295
'XP06'	2.05908	2.96471	0.50163	0.36727	1.10045	0.24438
'XP06'	3.73597	2.34941	0.83844	0.44628	0.7053	0.34496
'XP06'	8.4561	1.18162	9.85351	0.31886	0.36269	2.49207

'AO24'	0.95691	13.6373	0.23087	0.30167	11.9034	0.36468
'AO24'	2.91934	1.25001	0.90223	0.34687	0.4015	0.46142
'AO24'	5.00329	1.46503	1.63131	0.35062	0.54018	0.90488
'AU46'	1.14035	10.7327	0.35137	0.32532	8.84105	0.50531
'AU46'	5.12999	1.79835	0.84967	0.33836	0.79283	0.57125
'AU46'	6.87725	2.68246	0.84648	0.43815	1.53225	0.82289
'AU46'	12.3682	1.82928	5.54844	0.31438	0.61369	1.76997
'CO47'	2.03611	6.48728	0.67352	0.34476	4.66292	1.12343
'CO47'	7.25975	2.02125	1.50263	0.34167	0.84593	0.86462
'DR16'	1.71919	9.13107	0.33825	0.29644	7.45076	0.81906
'DR16'	4.65174	1.2313	1.40887	0.3396	0.4485	1.16565
'EO30'	1.72572	6.9312	0.71142	0.289	5.33033	0.95203
'EO30'	5.76885	1.67865	0.84877	0.29423	0.52058	0.57032
'EO30'	8.20599	2.75997	1.09883	0.33771	1.66102	1.11471
'ES57'	1.21042	10.714	0.45206	0.35379	9.06363	0.57727
'ES57'	7.74207	2.10847	1.22732	0.38464	1.448	2.73668
'GR27'	1.31231	13.9255	0.43306	0.37938	12.1776	0.61395
'GR27'	4.09113	1.83551	1.67155	0.35053	0.84703	0.87261
'ME52'	1.19376	12.7578	0.3157	0.34625	10.9577	0.48002
'ME52'	7.85644	2.00944	1.02275	0.40129	0.98434	0.75795